Crashworthiness and Puncture Protection Analyses of LNG Tenders

Final Report

March 2019

Prepared for: Ron Hynes
Assistant Vice President, Technical Services

Association of American Railroads
425 Third Street, S.W., Suite 1000
Washington, DC 20024

Prepared by: Steven W Kirkpatrick, Ph.D.
Christina Wagner, Ph.D.
Claudia Northrup

Applied Research Associates, Inc.
95 1st Street, Suite 100
Los Altos, CA 94022

Contents

Figures

Tables

ACKNOWLEDGMENTS

The analyses described in this paper primarily were performed by Applied Research Associates, Inc. (ARA) under sponsorship of the Association of American Railroads (AAR). In addition, the work described in this paper has benefitted from support and consultation with a variety of industry and government personnel. Significant contributions or technical information has been provided by Union Pacific Railroad, BNSF Railway, Chart Industries, EMD, the Volpe Transportation Systems Center, and the Federal Railroad Administration (FRA).

1 Introduction and Scope

The extensive North American freight rail network is currently operated with diesel as the sole fuel source. However, the Class 1 railways have recently started to explore Liquefied Natural Gas (LNG) as an alternative fuel source, which has a lower environmental impact and could provide fuel cost savings compared to diesel. As part of this effort, a limited number of legacy LNG fuel tenders have been built for operational testing based on cryogenic tank car designs. Examples of these legacy tenders are shown in Figure 1.

Figure 1. Photographs of the legacy LNG fuel tenders.

Programs to evaluate LNG as a locomotive fuel have been documented in several industry publications [e.g., 1, 2]. The efforts to develop a specification for fuel tenders is being led under the Association of American Railroads (AAR) Natural Gas Fuel Tender Technical Advisory Group (NGFT TAG), a joint effort of the AAR Locomotive, Tank Car, and Equipment Engineering Committees, with the FRA and multiple participants from industry. This task force is working to address the various regulatory and safety issues. For example, LNG tenders are not permitted to move by rail, unless approved under an FRA waiver. The mission of the NGFT TAG is "Develop Standard(s) for future Natural Gas Fuel Tenders for the railroad industry to support the use of natural gas (methane) as an alternative locomotive fuel."

This report describes a project performed by Applied Research Associates, Inc. (ARA) to support the AAR to provide objective analyses to support the NGFT TAG and other stakeholders related to the safety performance of the Natural Gas Fuel Tenders. This is intended to address issues both for the near-term goal of obtaining FRA authorization for existing BNSF Railway and Union Pacific Railroad legacy LNG tenders for operational testing as well as the longer-term development of final performance standards to be used in an AAR specification for Natural Gas Fuel Tenders.

The scope of the work described here is limited to the crash safety of the primary tender tank and structural members. The overall specification being developed by the NGFT TAG addresses many more issues beyond the structural crash performance (e.g., locomotive interface, piping, pumps, hoses and connections, fuel supply requirements, electrical controls, etc.) The evaluation of the integrity and performance of these nonstructural components under crash conditions were not included in the scope of the analyses described in this paper.

Detailed finite element (FE) crash and impact analyses are being performed for tender designs for a range of collision scenarios. The results of the simulations are being used by the NGFT TAG to understand the potential consequences of the proposed collision load cases and inform the development of performance criteria for tenders. In addition to evaluating baseline designs, the analyses can be used to investigate potential mitigation strategies to improve the crashworthiness of NGFTs. The analyses have an additional purpose to demonstrate that any requirement that is placed in the specification is realistic and can be addressed with available protection technologies. It is important to assess that it is possible to design a functional tender that meets the specification.

The objective of this report is to present some preliminary analyses for each of the collision scenarios to indicate the range of safety issues addressed by the NGFT TAG. The analyses performed included tank impact and puncture analyses, analyses of proposed design loading conditions, and analyses of specific collision scenarios. The puncture analyses applied the puncture methodologies developed in the previous Next Generation Railroad Tank Car

(NGRTC) Project and the Advanced Tank Car Collaborative Research Program (ATCCRP) and described in References 3 and 4.

The collision scenarios selected to evaluate the performance of the LNG tender designs were developed in a collaboration between the FRA, the Volpe transportation Systems Center, and the NGFT TAG. The set of primary collision scenarios that pose a safety risk for LNG tenders that were developed are:

1. Head-on collision between two locomotive-led freight trains
2. Collision of highway vehicle into LNG tender at grade-crossing
3. LNG tender rollover scenario
4. Side impact with the NGFT tank
5. Head impact with the NGFT tank

The objective of the side and head impact scenarios are to ensure integrity of the NGFT jacket and inner tank to resist punctures in the variety of blunt impact conditions that can occur in derailment or sideswipe impact scenarios.

The primary objective of the crash safety analyses is to prevent any significant releases of the natural gas in the collision scenarios. A secondary objective is to provide a safe environment in any post collision response and to allow for appropriate handling of the LNG as required by the collision response and damage. As a result, the primary damage and failure mechanisms of interest are:

1. Puncture of the inner cryogenic tank.
2. Overpressure leading to a failure of a rupture disk or release of LNG.
3. Puncture or loss of vacuum in jacket.

The puncture of the inner cryogenic tank would likely result in a significant release and should be prevented for all of the scenarios evaluated. The consequences of an overpressure can vary based on the specific design of the rupture disk and/or pressure release valve systems used on the tank. Preferably, the tender design incorporates a system with self-reclosing pressure release valves and the dynamic overpressure in a collision results in only a brief venting response from the tender. However, for either design, maintaining a response below the pressure relief limit is preferable. Finally, the puncture of the jacket or release of vacuum would not be an immediate risk of release but would result in a significant reduction in the effectiveness of the tender insulation. As a result, intervention would be required in a significantly shortened time schedule to prevent a pressure build up in the tank and subsequent release.

2 Analysis Methodologies

The LS-DYNA finite element code was used for the NGFT analyses described in this report [5]. LS-DYNA, developed and maintained by the Livermore Software Technology Corporation (LSTC), is an explicit nonlinear three-dimensional finite element code for analyzing the large deformation dynamic response of solids and structures. LS-DYNA has many features ideally suited to the analysis of vehicle collisions and is well accepted in the crashworthiness community as a state-of-the-art code. Equipment manufacturers commonly use LS-DYNA in the design of passenger rail car and automotive crash safety. The model for the tank car was developed using the TrueGrid preprocessor code [6].

2.1 Validation of Modeling Methodologies

It is difficult to fully verify and validate any code for the full range of highly nonlinear responses and modeling techniques necessary for analysis of impact and crash analyses without a corresponding full-scale crash test program. The physical phenomena involved in the impact response are extremely complex and nonlinear including large-scale deformation, material damage and failure, and complex and evolving contact and impact behaviors.

The first requirement to assure the validity of the software and modeling techniques is to select a code and modeling techniques that have been widely applied and validated for a wide range of applications with the physical phenomena involved in vehicle impact and crashworthiness assessment. The analyses used in this project use the LS-DYNA finite element code, which has a long history of application for various problems in crashworthiness, blast and impact response, dynamic fracture, impact and penetration mechanics, and other related problems.

LS-DYNA has a large base of users in different applications as demonstrated by the annual LS-DYNA Users Conferences held in the United States, Europe, and Asia. An exact number of LS-DYNA users is not currently available but includes more than 2000 client organizations worldwide. Example LS-DYNA clients in the automotive crashworthiness community include: Ford, General Motors, Fiat Chrysler, Honda, SAAB, OPEL, Toyota, Jaguar, Porsche, and Rover.

For quality assurance (QA) of LS-DYNA, LSTC runs a minimum of 2,200 QA problems before a new version of LS-DYNA is released.

In addition to the validation efforts of the larger LS-DYNA user community, ARA has compiled a portfolio of validated component and system level analyses. The following is a list of examples of ARA projects with LS-DYNA model validation:

- Static and dynamic buckling examples [7-16].
- Pioneer car train crash example [17].
- Crown Victoria crash model development [18, 19].

- Various highway and rail crashworthiness research programs [20-26].
- Dynamic ductile fracture analysis of steel weldments [27-35].

In addition, research on the Next Generation Railroad tank Car (NGRTC) developed and validated a modeling capability used to analyze the impact and puncture response of tank cars [3]. This modeling capability is applicable to many of the analysis scenarios applied to the NGFT designs in this study. A brief summary of this validated analysis methodology from the NGRTC program is provided here.

Full-scale impact tests were performed on tank cars [42, 43] and the results were used to validate the models. The model developed for the 105J500 chlorine tank car used in the testing is shown in Figure 2. This model is an extension of previous models used to assess the integrity of tank car designs to derailment and impact conditions [44-45]. The model was developed with the TrueGrid mesh generation code [6] for analysis with the LS-DYNA nonlinear finite element code [5]. The model includes all of the primary tank car structures including the jacket and jacket standoffs, commodity tank, manway, bolsters, stub sills, and outriggers. The outriggers were attached to the draft gear to prevent a post-test rollover of the target tank caused by the rebound off the reaction wall in the impact testing.

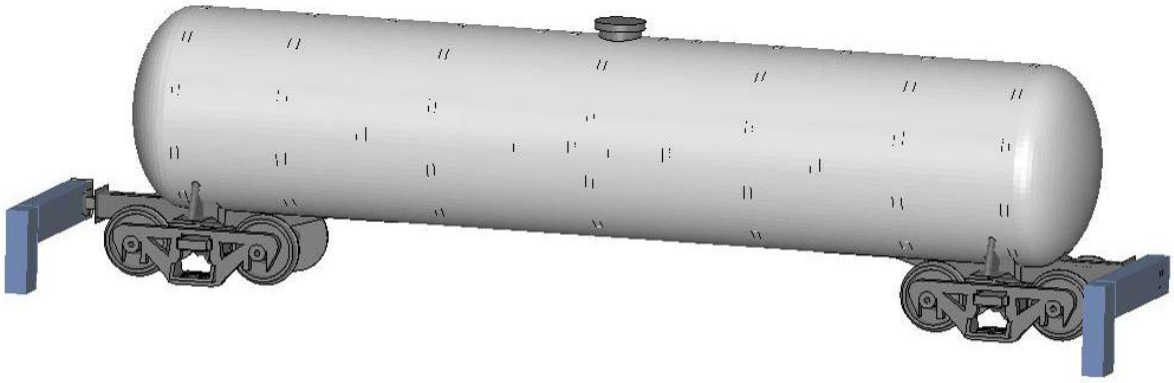

Figure 2. Updated model of a 105J500W pressure tank car.

The tests were fully instrumented with accelerometers, string potentiometers, pressure gauges, and strain gauges. These measurements were compared to the model predictions to validate the model. Overall, very good agreement was obtained between the prediction and test for the various measurements made. An example of the agreement is the comparison of the predicted and measured force-deflection curves, shown in Figure 3. This force-deflection curve is an important characteristic of the tank car for a given impact scenario. The area under the force-deflection curve is the impact energy that is dissipated (the primary measure used to assess the puncture protection levels). The comparison of the force-deflection behaviors shows good agreement between the calculation and the test.

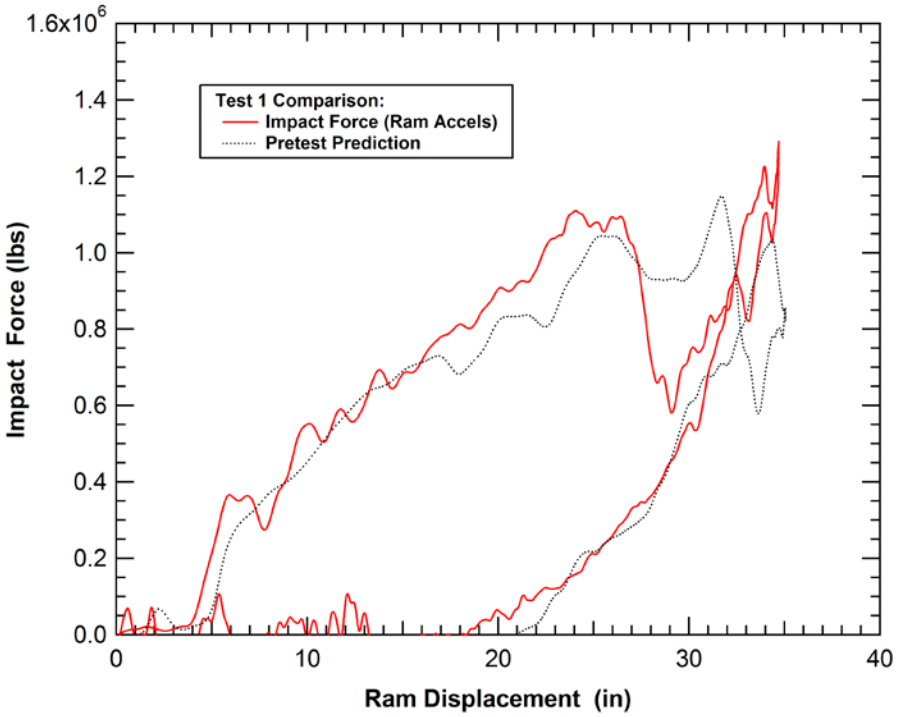

Figure 3. Comparison of the measured and predicted Test 1 force-deflection curves.

2.1.1 Material Damage and Failure Behaviors

The other necessary component of the predictive tank car puncture modeling capability developed for the NGRTC program is a detailed model that can be used to determine the impact damage and failure of the tank and protective system materials. An extensive program of laboratory materials testing was performed to characterize the tank car materials of interest [e.g., 50, 56-61]. The tests included various material characterization tests, such as notched tensile tests and combined tension/shear tests, used to calibrate the material constitutive and failure behavior. Material strain rate effects were investigated for the tank car puncture behavior and found to not have a significant effect. Additional component tests, such as punch tests and bend tests, were performed to validate the constitutive models.

The material damage and failure model applied is the Bao-Wierzbicki (BW) model [62, 63] that defines the material damage development based on the current stress state in the material and the plastic strain increments. The critical strain function is that proposed in the BW criterion and contains multiple branches depending on the range of stress state, as shown in Figure 4. The critical strain in each branch are governed by the equation

$$\varepsilon_c\left(\sigma_{mean}/\sigma_{eq}\right)=\begin{cases}\infty & \left(\sigma_{mean}/\sigma_{eq}\right)\le -\dfrac{1}{3}\\ \dfrac{A}{1+3\left(\sigma_{mean}/\sigma_{eq}\right)} & -\dfrac{1}{3}\le\left(\sigma_{mean}/\sigma_{eq}\right)\le 0\\ 9(B-A)\left[\left(\sigma_{mean}/\sigma_{eq}\right)\right]^2+A & 0\le\left(\sigma_{mean}/\sigma_{eq}\right)\le\dfrac{1}{3}\\ \dfrac{B}{3\left(\sigma_{mean}/\sigma_{eq}\right)} & \dfrac{1}{3}\le\left(\sigma_{mean}/\sigma_{eq}\right)\end{cases}$$

and the parameters A and B can be determined by a series of tests under different stress conditions including notched tensile tests, with specimens of varying notch radii, and tensile-shear tests with different ratios of tension to shear stress.

Although these material tests were used to develop the constitutive and failure model parameters, the resulting constitutive models were used to simulate the tests. This provides a validation that the material parameters were properly incorporated into the analyses and that the constitutive and failure model is capable of simulating the range of material behaviors under different loading conditions. The first of these material test series was the notched round bar (NRB) test (shown here on TC128B). A comparison of the calculated and measured stress-strain behavior across the notch for the three different radii specimens is shown in Figure 5. The comparison shows that the constitutive and damage model were capable of reproducing both the increase in stress level and reduction in ductility that occur as the notch radius is reduced. The BW failure parameters used provide a good correlation to the observed failures of the specimens.

For the various steels evaluated in this program, the component punch test [59] was the primary laboratory material test used to validate the constitutive and failure models. An example of a model and simulation of a punch test on a 0.488-inch-thick TC128B plate is shown in Figure 6. The corresponding comparison of measured and calculated punch force-displacement curves for a series of three different tests on the TC128B plate is provided in Figure 7. In addition to the force-deflection curve, the final profile of the plate specimens after the punch tests were digitized and compared to the analyses. Again, the overall agreement between the testing and analyses was good. This agreement provides a further validation that the BW failure model is appropriate for predicting puncture of the tank cars.

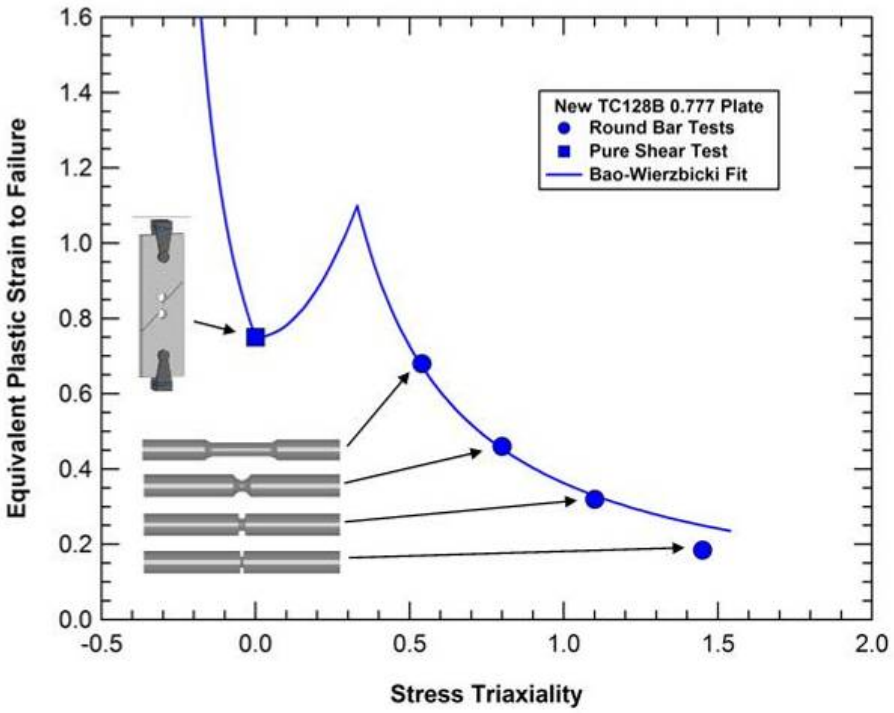

Figure 4. Bao-Wierzbicki failure surface and tests used for model calibration.

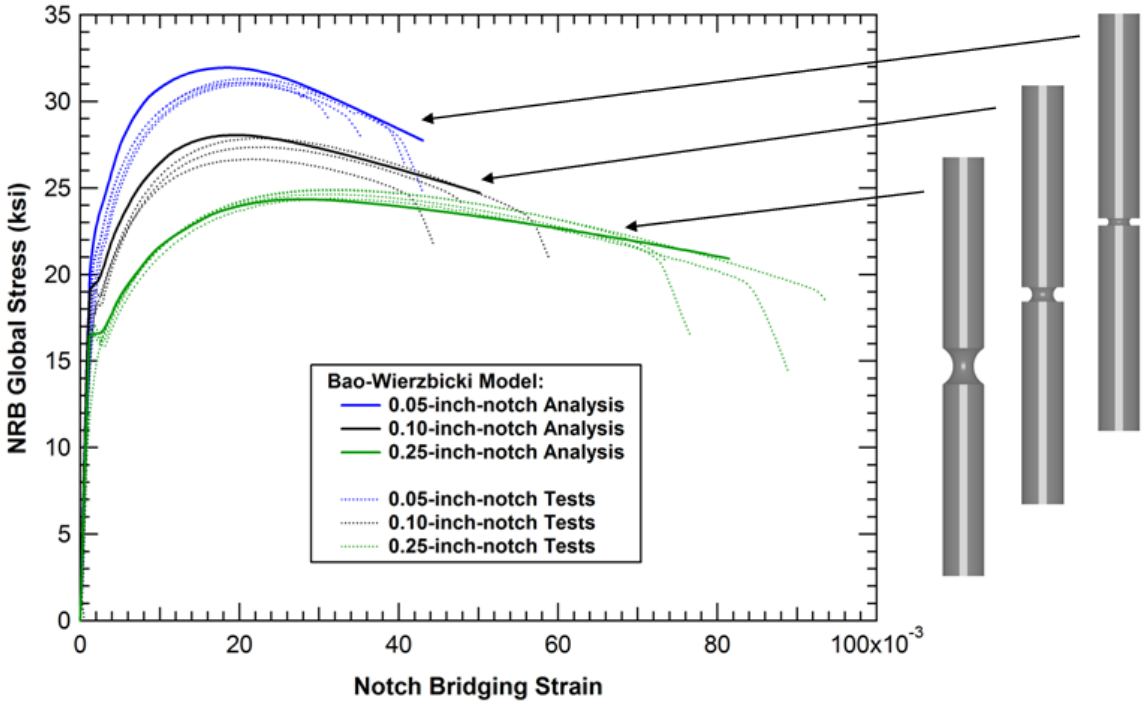

Figure 5. Validation of the notched round bar test behavior for TC128B.

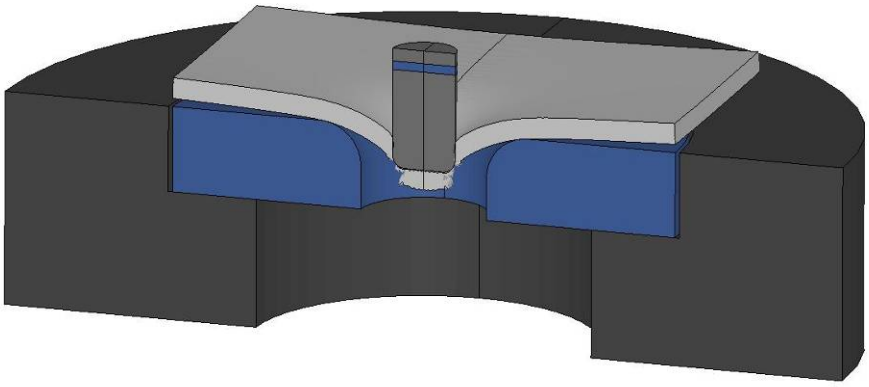

Figure 6. Simulation of the punch test on the thin TC128B plate material.

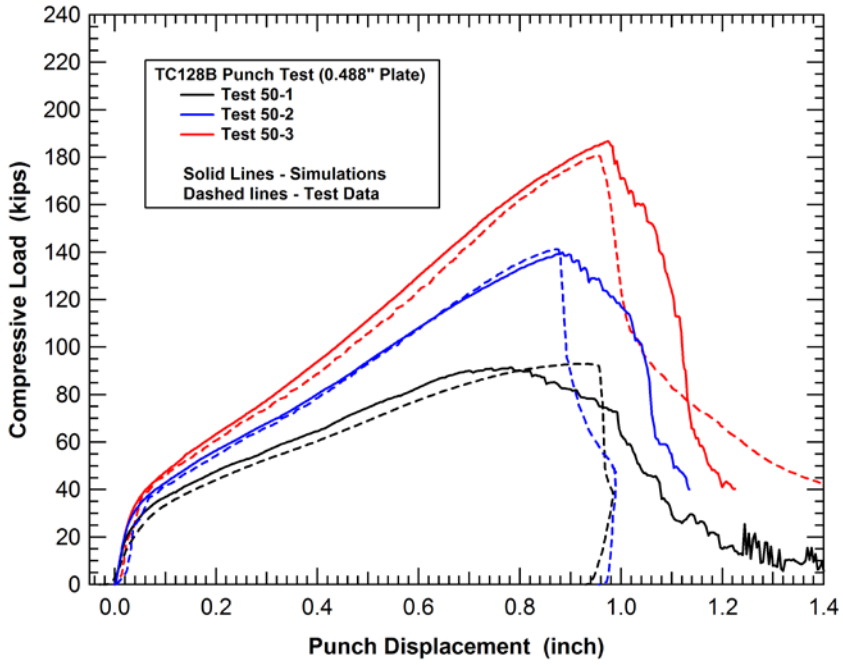

Figure 7. Force-deflection curves for three punch test configurations on TC128B.

2.1.2 Tank Car Puncture Modeling

The BW failure modeling capability was combined with the tank car model to complete the tank car puncture prediction capability. The tank model was also simplified in these analyses to have half-symmetry by removing the manway, bolsters and lading. The simulation of the full-scale tank car impact test (Test 2 - above the puncture threshold) was performed using the tank puncture model, as shown in Figure 8. The model shown was reflected vertically about the symmetry plane (seen as a line in the figure) for improved visualization of the impact behavior. The impactor in this analysis was a rigid 6x6 inch ram with a 0.50-inch radius around the edges and a total weight of 286,000 lbs. The small rectangular patch of elements under the impactor (already punctured in Figure 8) is the fracture zone where the BW failure model was applied. The remainder of the tank structure was again modeled with 4-node shell elements and a tied shell-to-solid constraint was used at the interface of the two model regions.

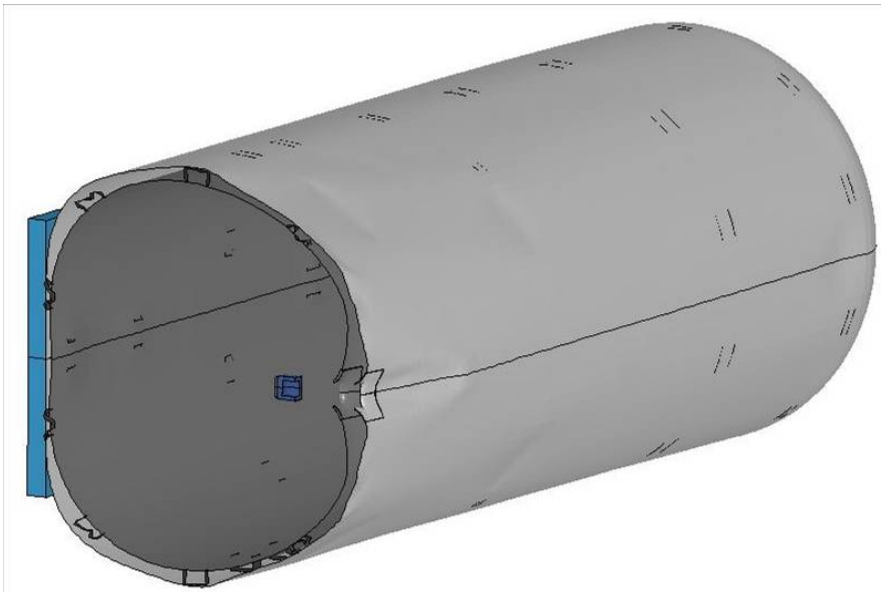

Figure 8. Simplified tank model analysis with Bao-Wierzbicki failure assessment.

The comparison of the measured and calculated force-deflection behavior for Test 2 with the tank puncture model is provided in Figure 9. The comparison shows overall good agreement between the calculation and test. The peak load at which the tank was punctured was very accurately captured by the model. The measured puncture force was 940,000 lbs and the calculated puncture force was 915,000 lbs. The primary discrepancy of the test and model was a slightly more compliant behavior in the model seen at the large displacements. This difference in compliance could primarily be attributed to the removal of the manway from the tank model in this analysis.

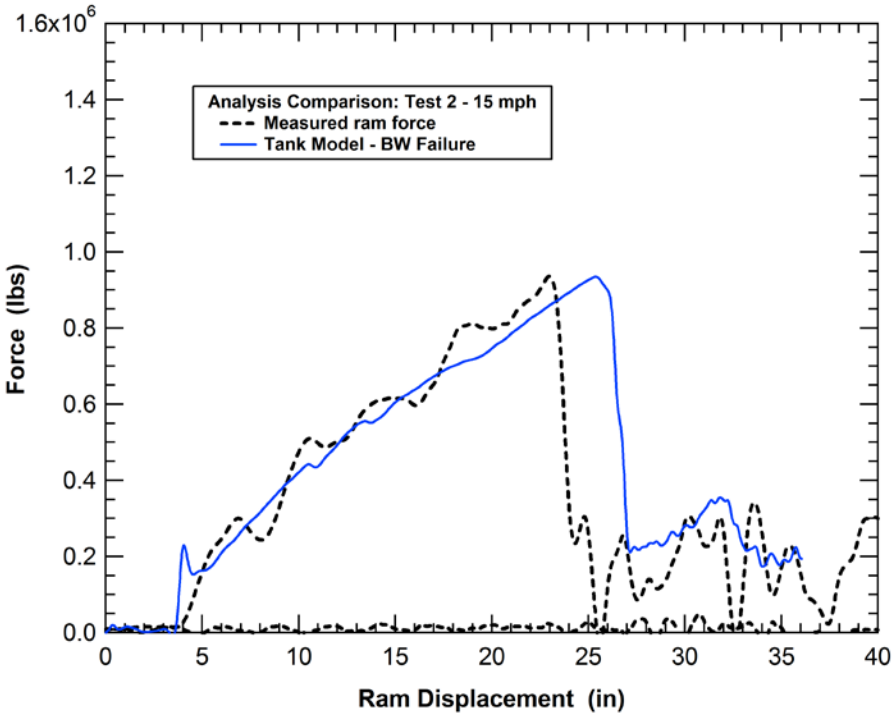

Figure 9. Tank puncture analysis of Test 2 with Bao-Wierzbicki failure assessment

2.1.3 Analysis of Tank Pressure Effects

The formation of the dent in the tank during impact there will be an increasing hydrostatic internal pressure level. For the 6-inch impactor this increase in pressure was relatively small (10%-15%). However, the larger dents produced by the larger impactor sizes would result in a larger internal pressure increase. Using a constant internal pressure modeling approximation was found to introduce significant errors in for larger impactor sizes.

To demonstrate the influence of the variable internal pressure during the impact a series of analyses was performed. In these analyses, a control volume was established for the tank and the change in volume was used to calculate a corresponding change in pressure. The assumption in these analyses is that the tank has a 10.6% outage (corresponding to a loaded chlorine tank car) and the gas in the outage follows an ideal constant temperature compression behavior during impact. The resulting relationship between the relative volume and pressure in the tank is shown in Figure 10.

The force-deflection curves with both constant and variable internal pressure for the 500 lb Cl tanks and the three different impactor sizes are shown in Figure 11. For the updated analyses with the variable pressure, the impact velocities were also reduced by 5 mph to be closer to the expected puncture threshold velocity. Adding variable pressure to the model results in a stiffening of the later portions of the force-deflection curve and a reduction in the ram displacements prior to the tank puncture. The reductions are more significant for the larger ram

sizes. This is expected since the larger rams have larger displacements prior to the puncture with a larger associated pressure change inside the tank. The comparisons show that the variable internal pressure does not have a significant influence on the puncture forces but does reduce the puncture energies by approximately 25-30% in the analyses with the 9x9 and 12x12 inch impactors.

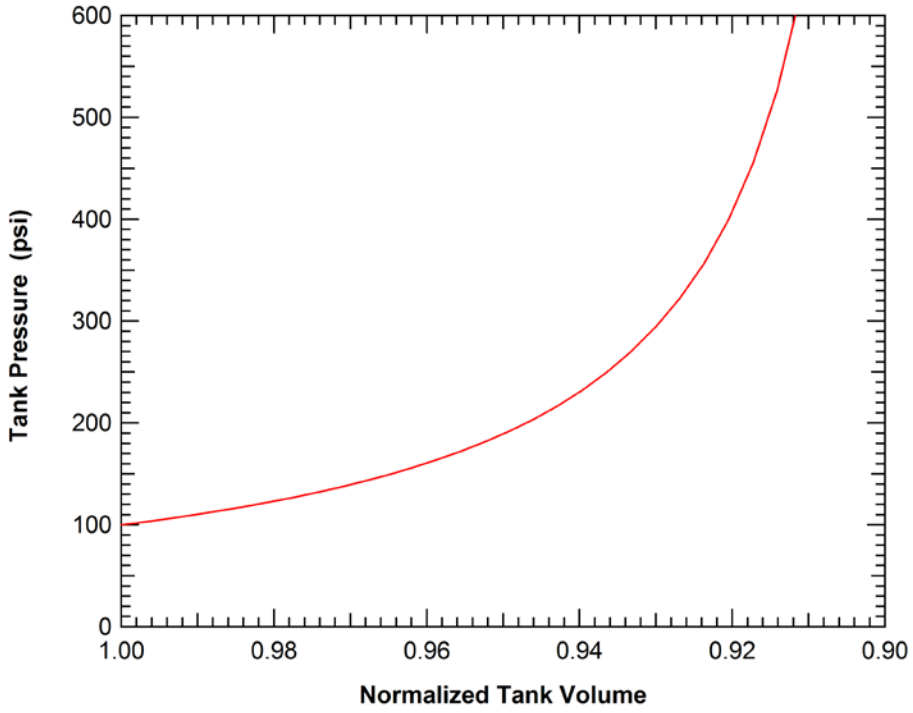

Figure 10. Pressure-volume relationship used for the tank control volume (10.6% outage).

The pressure histories for the tank control volume for the three 500 lb Cl tank impact analyses are plotted as a function of the ram displacement in Figure 12. In the 6x6 inch impactor analysis, the pressure change is less than 10% and the previous approximation of a constant 100 psi internal pressure is a reasonable simplification for the analyses. For the 9x9 and 12x12 inch impactors, the internal pressures increase to approximately 120 psi and 140 psi, respectively, at the point of the puncture initiation. These pressure increases are becoming sufficiently large to influence the tank effective stiffness during the impact.

2.2 Constitutive Model Development

Detailed constitutive and failure models for a range of tank car materials had been previously developed and validated in previous tank car safety research programs [3, 4]. In general, these constitutive models have been directly adapted to these analyses performed on the NGFTs. The one unique new material that needed to be added is the behavior of the stainless steel LNG tank at cryogenic temperatures.

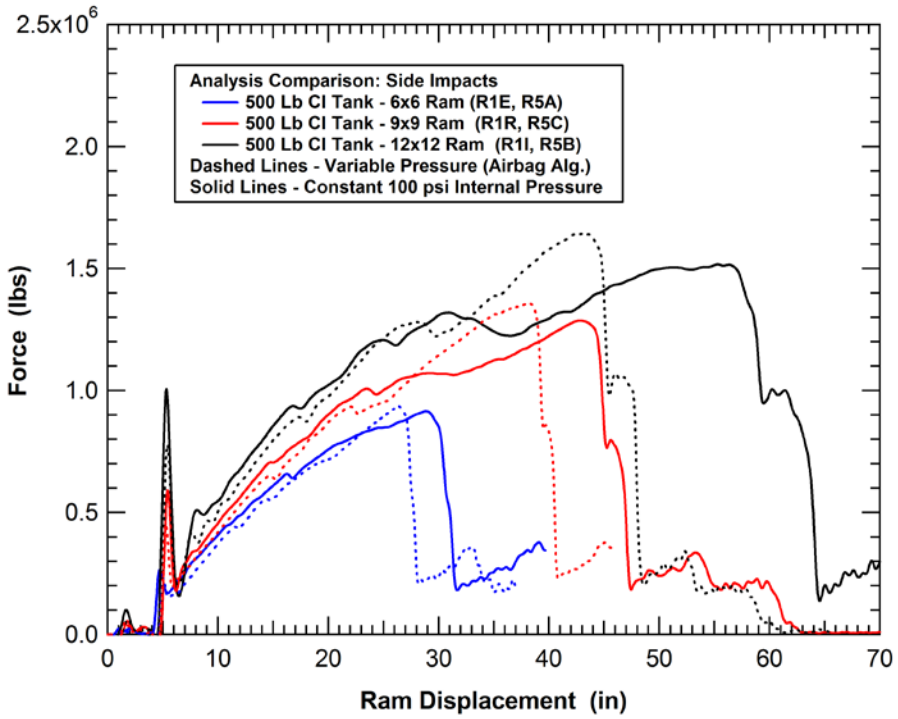

Figure 11. Effect of variable internal pressure on 500 lb tank impact response.

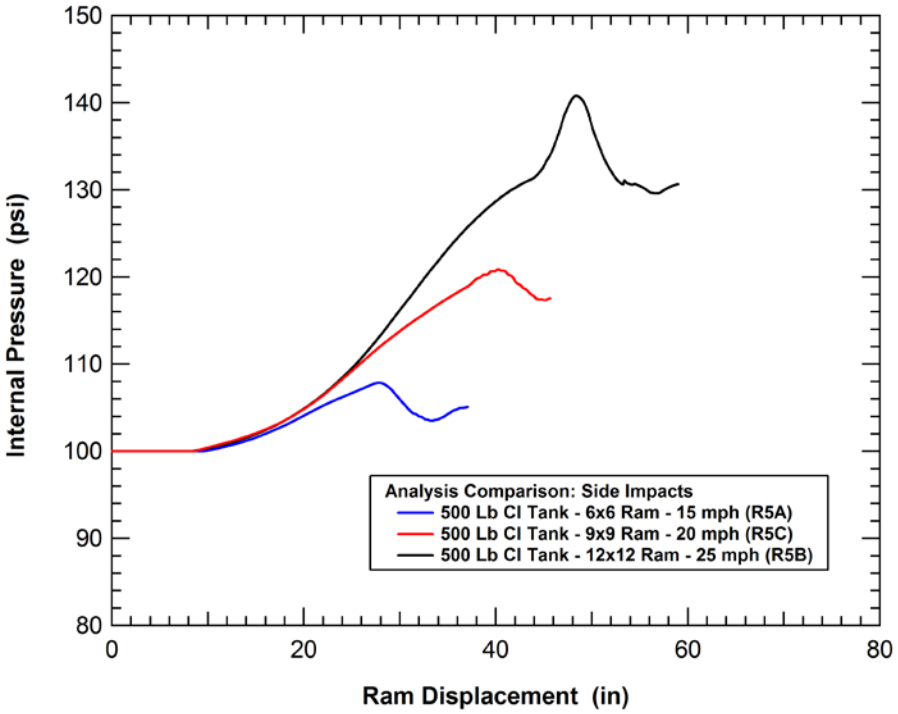

Figure 12. Calculated internal pressure variations in the 500 lb tank impact analyses.

2.2.1 Cryogenic Stainless Steel Material Properties

The analyses performed in this study required a nonlinear constitutive model for the NGFT inner cryogenic vessels. The first step in the development of a constitutive model is the development of the nonlinear stress-strain behavior. This governs the mechanical response of the material and prescribes the internal forces (stress) that are developed as the material is deformed (strained). For the analyses performed in this study, the model is based on test data for 304L stainless steel at room and cryogenic temperatures found in open literature sources [53, 54]. The data shown in Figure 13 are the measured engineering stress-strain behaviors. This engineering stress was obtained by dividing the measured loads by the original cross-sectional area of the specimen. Similarly, engineering strain was obtained by dividing the change in the specimen gauge-section length by the original length.

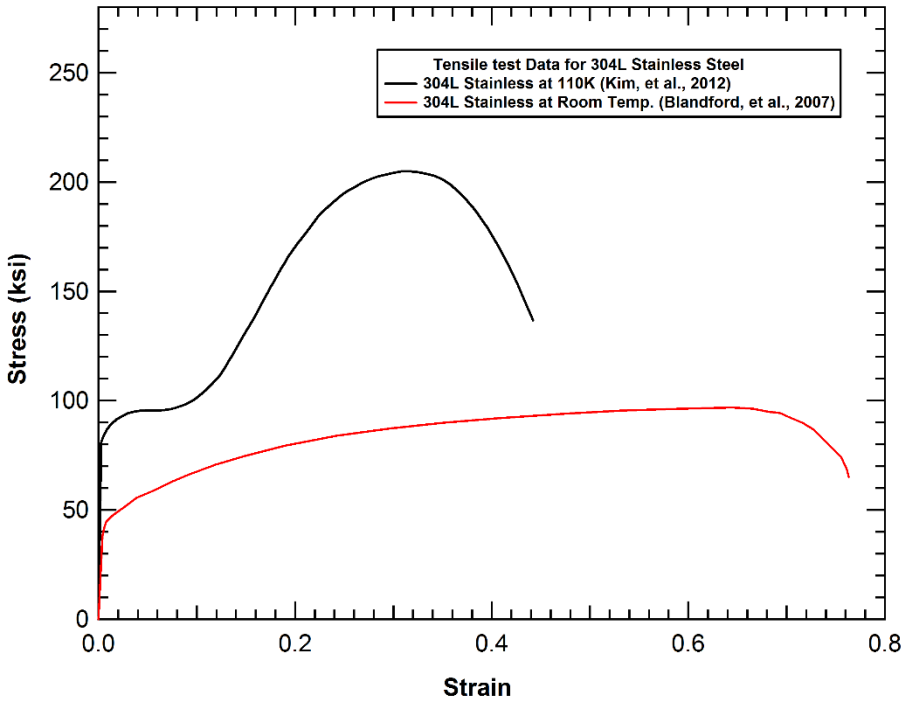

Figure 13. Material testing data for 304L stainless at room and cryogenic temperatures.

The constitutive model in the finite element analyses requires that the engineering data be converted to true stress and true strain. This conversion accounts for the changing cross section of the specimen as it deforms. The specimen cross section changes (shrinks) significantly during the test, and the engineering stress does not yield the "true" stress in this cross section. Similarly, the engineering strain is not representative of the material behavior, especially when a general three-dimensional state of strain exists. As a result, the engineering stress decreases as some materials approach failure, implying a weakening of the material. In reality, the stress in the cross section is increasing due to the reduction in the cross-sectional area (i.e., necking).

There are several different ways to measure stress and strain based on the coordinate system used [55]. Some are based on material (Lagrangian) coordinates and some on spatial (Eulerian) coordinates. These give rise to terms such as "Green" and "Almansi" strain tensors. These are important in writing a computer code to solve large strain problems. An alternate approach is to define a "true" or "natural" stress and strain. The true stress is based on the load divided by the actual cross-sectional area of the specimen and is equal to the engineering stress multiplied by a term to correct for the change in cross section.

$$\sigma_T = \sigma_{eng}(1+e) \tag{1}$$

where σ_T and σ_{eng} are the true and engineering stresses, respectively, and e is the engineering strain.

Prior to the onset of localization (necking), the natural or true strain, ε_T, is defined as

$$\varepsilon_T = \ln(\frac{l}{l_o}) = \ln(1+e) \tag{2}$$

This definition comes about from defining the incremental true or "natural" strain as the current "change in length" divided by the current length, or

$$d\varepsilon_T = \frac{dl}{l} \tag{3}$$

This is in contrast with the definition of engineering strain that references the change in length, Δl, divided by the original length, l_0, or

$$e = \frac{\Delta l}{l_0} \tag{4}$$

After the onset of localization, the determination of the true strain in the necked region becomes more complex and requires measurement of the local neck geometry.

The 304L stainless steel engineering test results are compared to the converted true stress and true strain data in Figure 14 (solid lines). The true stress curves in this figure do not include a correction for the necking behavior. As a result, they are only valid up to the onset of necking at a true strain of approximately 20-25%. The actual true stress and true strain curves for the material continue to strain harden throughout the loading if the effects of necking were corrected. An extrapolated true stress curve that corrects for the effects of the necking behavior is added to Figure 14 (dotted blue line). This extrapolated curve is used in the material constitutive model.

The final step in obtaining the tabular stress-strain parameters for the 304L stainless steel constitutive model was to fit a smooth set of points to the extrapolated true stress data. This final tabular fit for the 304L stainless steel is shown by the markers on the true stress versus plastic strain curve in Figure 14. The specific values for the tabular stress-strain curve are also listed in Table 1. As a validation that this curve accurately captures the true stress-strain behavior of the material, a tensile specimen model was generated and the constitutive parameters were applied to simulate the tensile test response. The calculation was analyzed to determine the engineering stress-strain behavior consistent to the tests (using an equivalent gauge section length). A plot of the calculated engineering behavior compared to the test data is shown in Figure 14. The simulated tensile test is indicated by the dashed black line in the figure. The comparison shows that the constitutive parameters accurately reproduce the material behaviors including the onset and development of necking in the specimen.

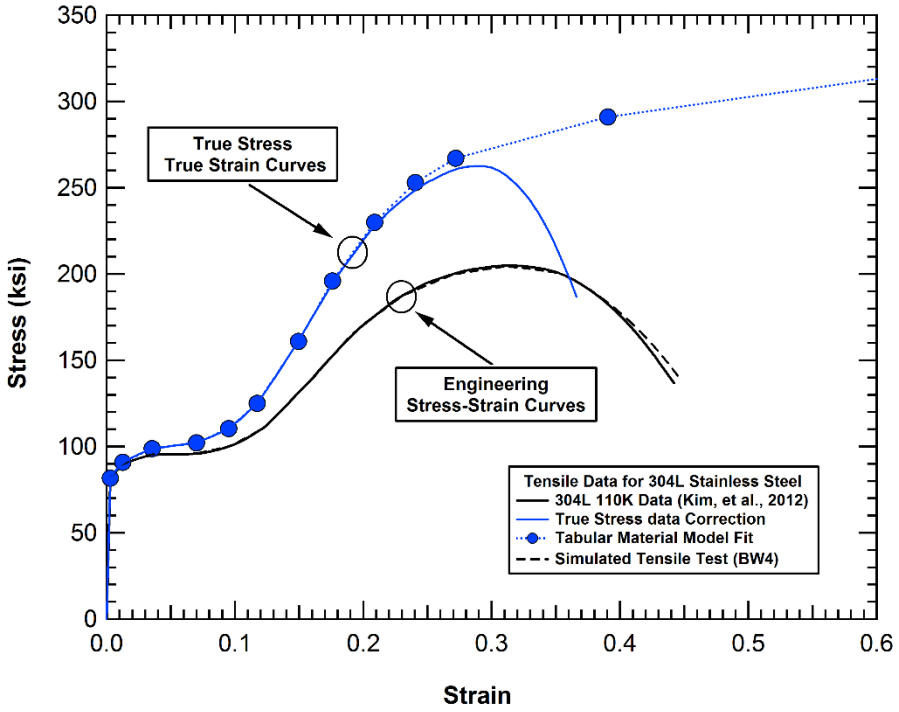

Figure 14. Comparison of engineering and true stress-strain data for 304L SS.

Table 1. Tabular 304L SS stress-strain curve values at cryogenic temperatures

Point No.	Plastic Strain (in/in)	True Stress (ksi)
1	0.00e+00	81.70
2	9.157E-03	90.80
3	3.190E-02	98.70
4	6.630E-02	102.2
5	9.100E-02	110.4
6	1.128E-01	125.0
7	1.437E-01	161.0
8	1.689E-01	196.0
9	2.006E-01	230.0
10	2.315E-01	253.0
11	2.625E-01	267.0
12	3.800E-01	291.0
13	9.855E-01	355.0

Subsequent to the completion of the analyses described in this report, the NGFT TAG funded a material characterization test program to confirm the response of A240 304 Stainless Steel at LNG cryogenic temperature. A240 304 Stainless Steel has a well-established performance history in several hundred DOT-113 tank cars as well as in many thousands of other cryogenic tanks and trailers and is the likely material for use in NGFTs. The behavior was expected to be very similar to that of the 304L data presented in Figure 13. The testing included tensile tests, notched tensile tests, and elevated strain rate testing. A summary of that data is provided in Appendix A. Although some differences were observed in the measured behaviors in this material characterization compared to the material model above, the differences were relatively small and would not significantly influence the conclusions of the analyses presented in the report.

3 Development of Vehicle Models

The development of the tender models is required to support the analyses to be performed under both Task 2 and Task 3. The models created included two legacy tender designs, and a modified tender design used to evaluate performance of various potential design options.

3.1 Legacy Tender Design 1 Model

The legacy tender design 1 model is shown in Figure 15. The tender was created with 1-inch elements and has about 215K total elements. For the baseline analyses conditions, the inner tank was pressurized to 50 psi with a 1 atmosphere vacuum between the jacket and inner tank. The weight of the inner commodity tank was increased to model a tank partially filled with LNG. The resulting tank weight was approximately 120,000 lb.

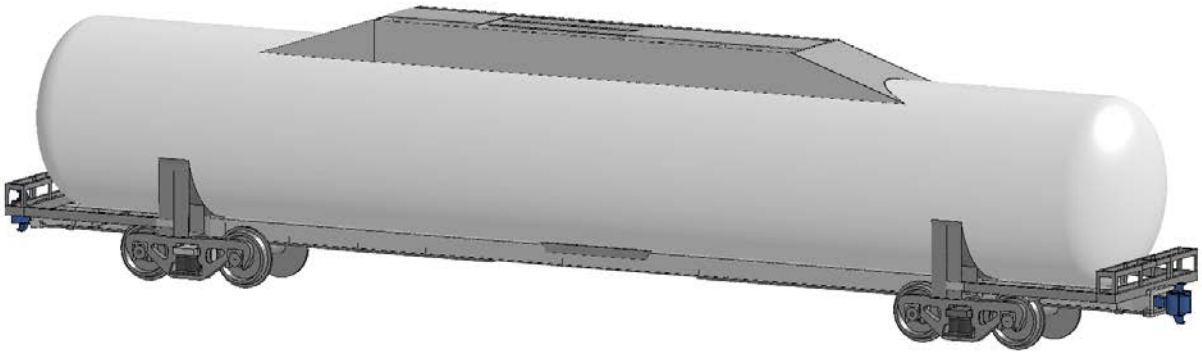

(a) Model geometry

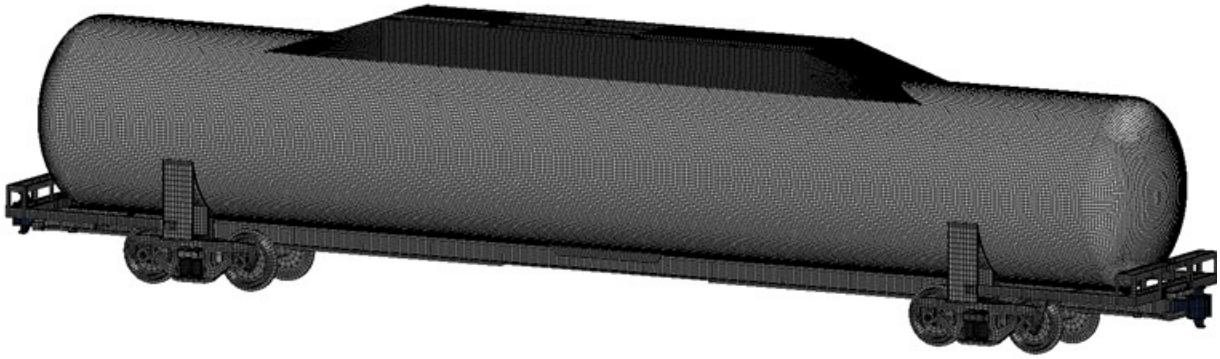

(b) Mesh resolution

Figure 15. LS-DYNA finite element model of the through sill tank tender design 1.

The development of these models was performed in stages with additional details and structures added to the model as needed for the various load cases. For example, the first load case analyzed was the train-to-train collision scenario so the primary structures of the model that were important are the tank, center sill, and underframe components that are load carrying and

transmit the train loads. Other features of the tender, such as the cabinets, top fittings, etc., would be added to the model when needed for the other load cases.

3.2 Legacy Tender Design 2 Model

The legacy tender design 2 model is shown in Figure 16. The tender was created with 1-inch elements and has about 215K total elements. The model has several significant design changes from the legacy tender design 1 such as the positioning of the bolsters and the safety equipment such as the protective cabinet designs and top fittings arrangement and protective housing. For the baseline analyses conditions, the inner tank was pressurized to 50 psi with a 1-atmosphere vacuum between the jacket and inner tank. The weight of the inner commodity tank was increased to model a tank partially filled with LNG. The resulting tank weight was approximately 120,000 lb.

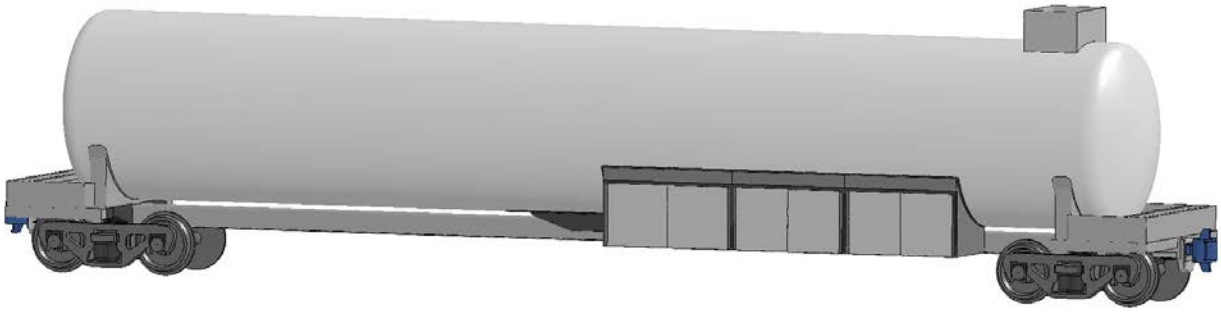

(a) Model geometry

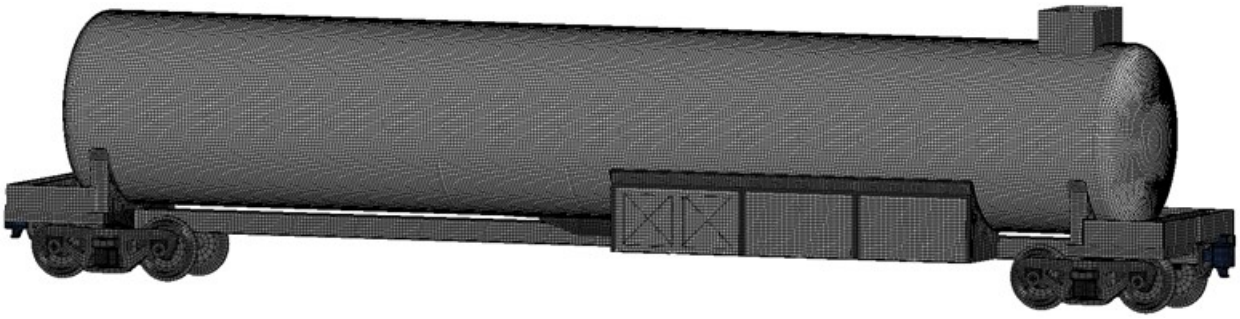

(b) Mesh resolution

Figure 16. LS-DYNA finite element model of the through sill tank tender design 2.

3.3 Enhanced Tender Design Model

In addition to the two legacy tenders, additional design modifications were evaluated to assess the performance of a potential enhanced tender design that might be built with improved crash safety performance. This tender was developed in stages as different collision scenarios were developed and different design requirements were considered by the NGFT TAG.

An example of the first generation of the Enhanced Tender Design is shown in Figure 17. This enhanced tender design was based on the Legacy Tender Design 2 platform. Note that subsequently, the AAR specification included requirements that a future conforming tender design to have a maximum length of 85 feet, width of 10 feet and will have truck centers of 58 feet. These dimensions would result in a longer overhang sill from the bolster to the striker than in the enhanced design shown. Some additional design work would likely be required to maintain a controlled crush response with the longer sill length. However, the types of modifications made in this example contribute to the controlled collision behaviors.

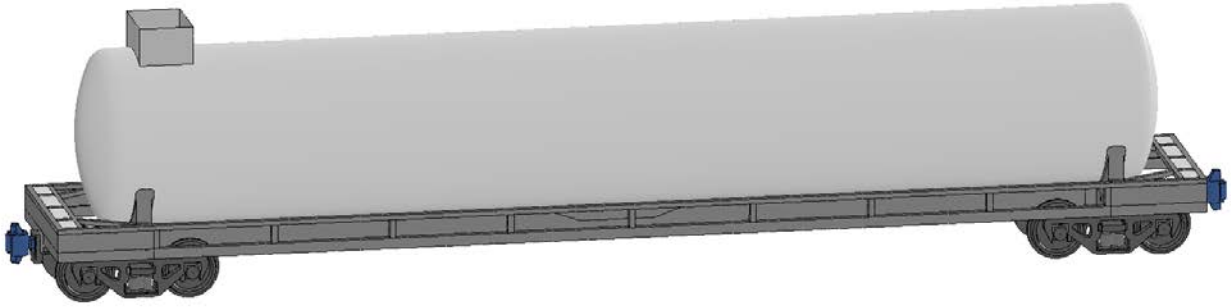

(a) Model geometry

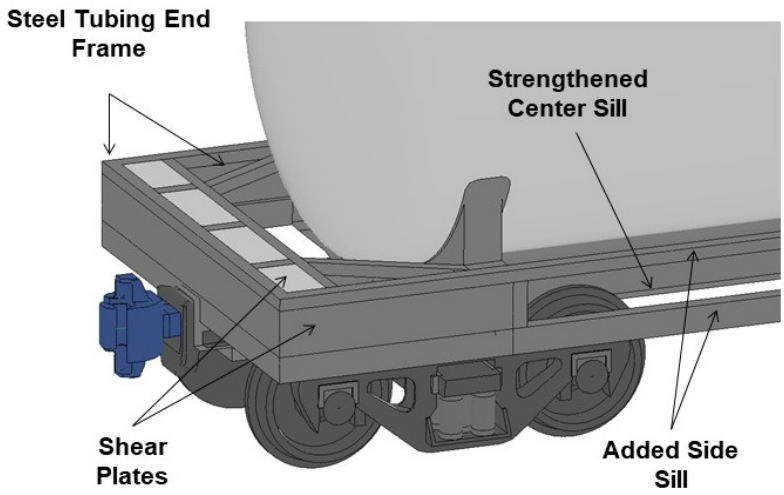

(b) Underframe design modifications

Figure 17. LS-DYNA finite element model of the initial enhanced tender design.

The significant underframe modifications incorporated into the initial Enhanced Tender Design are shown in Figure 17. The end frame structures that were initially constructed using angle sections are upgraded to rectangular tube sections. Shear plates are included in the outer end frame openings for a significant increase in the crush strength and energy absorption. Additional closure plates were added over the length of the center sill to increase the buckling strength.

Finally, a side sill or side frame was added over the full length of the tender to protect against side impacts (e.g. a grade crossing collision).

Subsequent modifications were made to the end frame configuration to incorporate switching steps as a required safety appliance for the tender. The modifications to the end frame structure for the addition of the switching steps are shown in Figure 18. The tubular end frame was narrowed at the end of the tender to make room for a ladder style step well. The design also includes additional strengthening of the end frame as well as shear plates and end enclosure plates around steps (not shown in the figure).

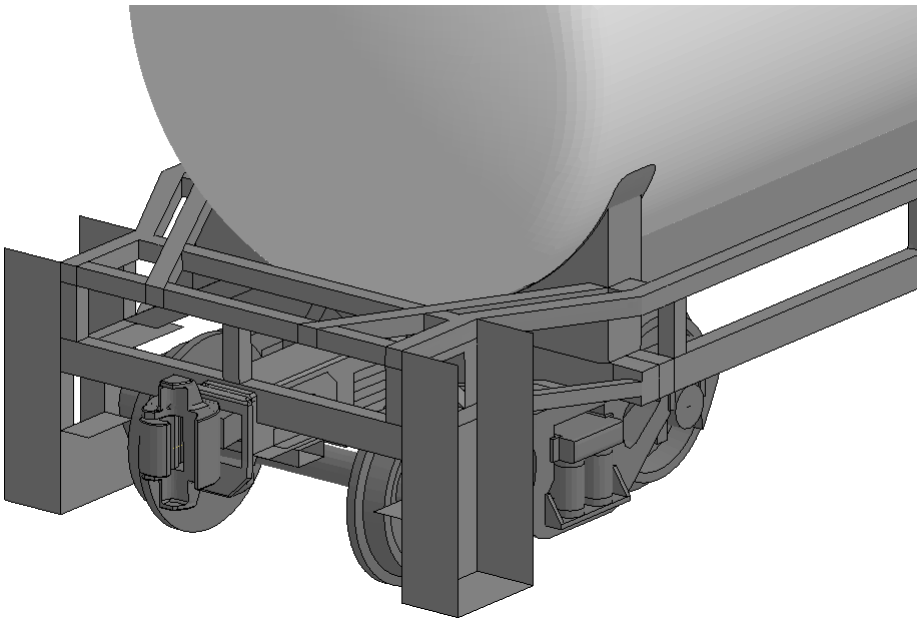

Figure 18. End frame geometry modifications to incorporate switching steps.

As the step well design and overall crash response was evaluated a few additional design modifications were incorporated into the enhanced tender design. The bolster and trucks were moved two feet inward away from the tender ends. This provided additional clearance between the wheels and the switching step well. In addition, it allowed for additional crush length in the end frame outboard of the bolster for additional energy absorption in the train-to-train collision scenario. The comparison of the modification to the design is shown in Figure 19. In addition, lateral bracing was added between the center sill and side sills (side frame) to provide stability and strength to resist side impact collisions. It is likely that additional framing or enclosure plates would be added at locations where equipment or piping was located outside the tender tank.

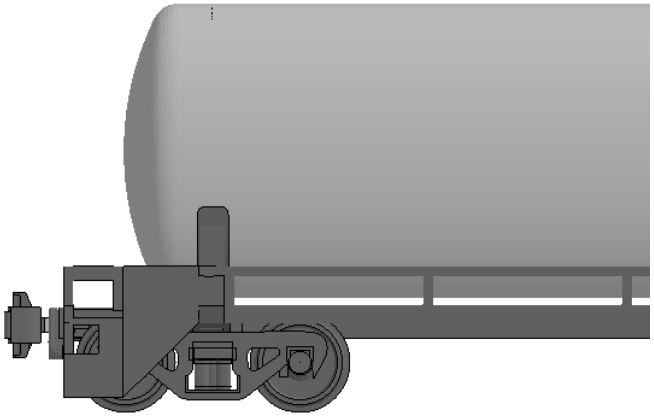

(a) Original bolster position

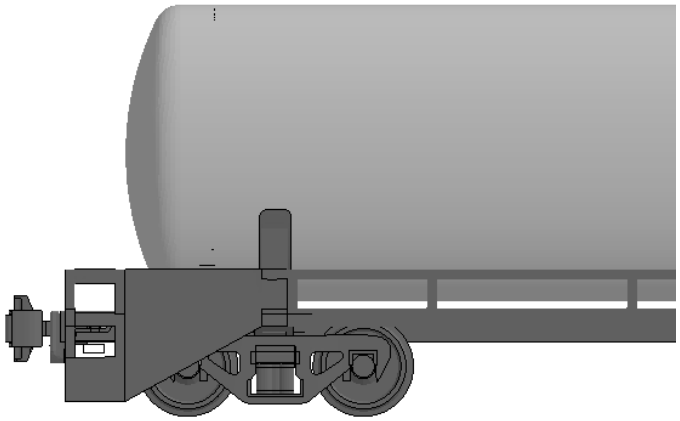

(b) Adjusted bolster position

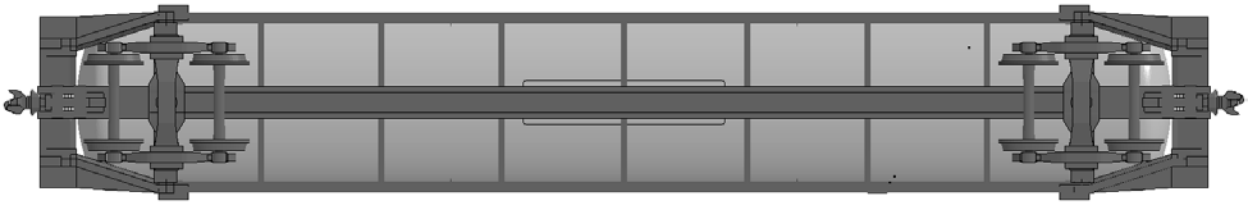

(c) Underframe design modifications

Figure 19. Modification of the bolster position for the updated enhanced tender design.

3.4 Locomotive Model Development

The analysis of the tender response in train collision scenarios required development of a suitable locomotive model that will be is coupled to the tender. The approach selected is to adapt an existing model for a locomotive, developed under a previous FRA research program, as shown in Figure 20. The model shown as SD-70 is actually an SD40T-2 ("tunnel motor" variant of an

SD40-2) with an S-580 cab/nose added and would be suitable as a reference model for analysis. However, it is expected that some modifications will be required such as improvements to the mesh resolution, material models, and components such as the trucks, suspension, and draft gear.

The FE analysis approach of the Two Harbors collision scenario was similar to Volpe's in that we primarily evaluated the locomotive crash behavior. Thus, Volpe's analysis results provide a good comparison to our FE analysis results. A locomotive model was provided by QinetiQ North America, Inc. (QNA). This model was developed for the Federal Railroad Administration (FRA) Office of R&D. A few modifications were made to the model provided to create the ARA FE model. The original QNA locomotive model has 3-5 inch elements with approximately 315,000 elements.

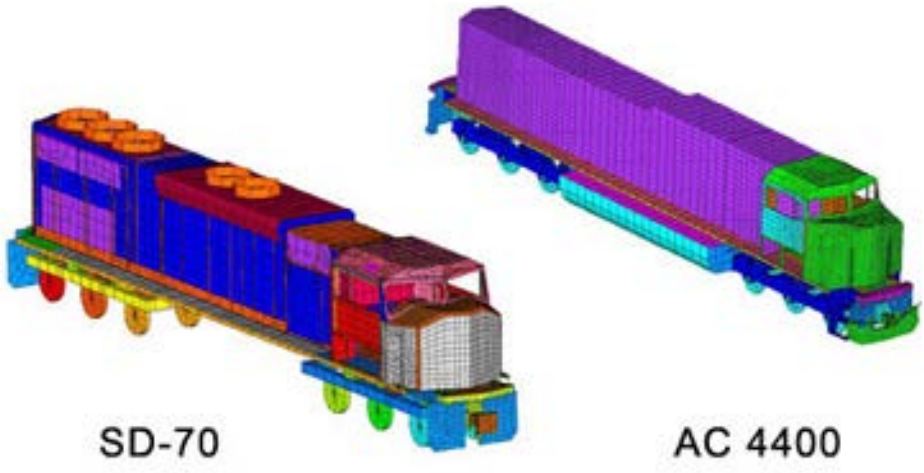

Figure 20. Locomotive models developed in previous FRA crash safety programs.

The final FE locomotive model used in the analyses is shown in Figure 21. The original QNA model had constraints to tie components of the locomotive, such as the long hood to the underframe and crew cabin. However, these constraints were rigidly tying components over large areas, producing an overly rigid locomotive underframe and superstructure. The rigid constraints were changed to tied contacts between the components, including: the crew cab, short hood and long hood to the underframe; underframe components to each other; and the anti-climber and draft box attachments. These tied interfaces provide a more realistic response between structures by tying only the local bonded sections as would result with a weld.

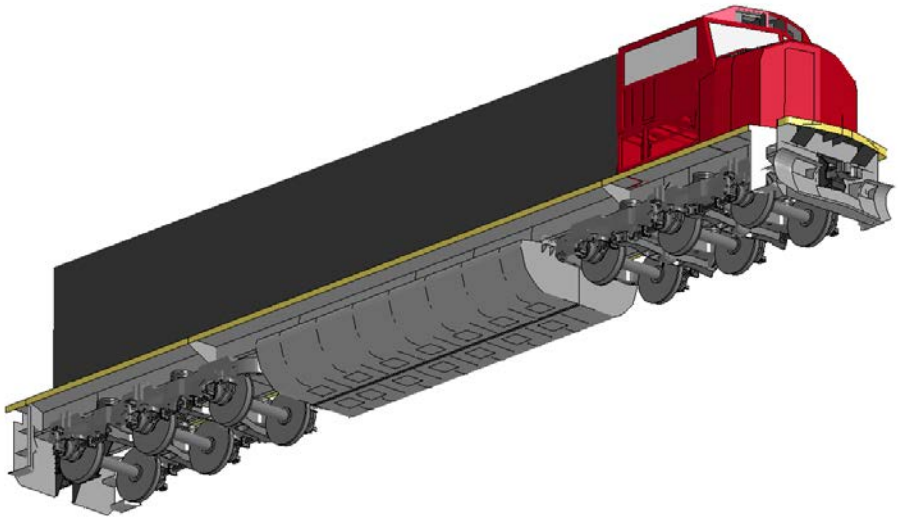

(a) Oblique underframe view

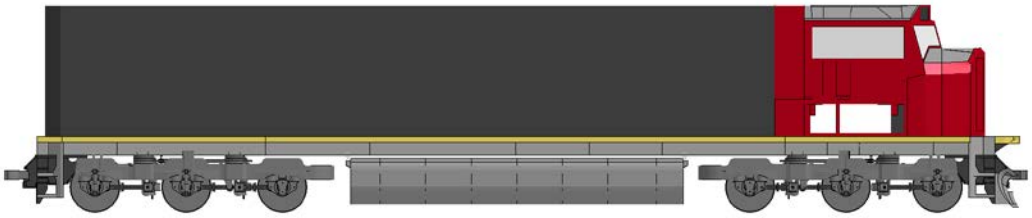

(b) Side view

Figure 21. ARA's FE locomotive model based on a QNA locomotive model.

The anti-climber in the original model was removed and replaced with an anti-climber based on Electro-Motive Diesel (EMD) drawings. The new anti-climber is wider with different stiffeners and attaches to the front of the locomotive underframe with a tied contact as described above. Figure 22 shows the original and modified anti-climbers. The breastplate was also expanded to accommodate the wider anti-climber. The anti-climber and its components were created with 1-inch elements to better capture the stress distribution and failure.

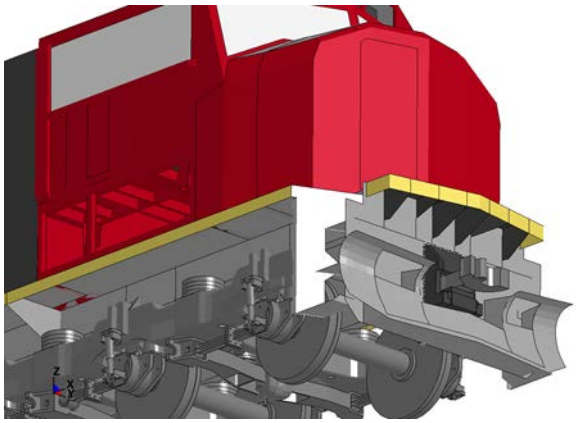

(a) Original anti-climber

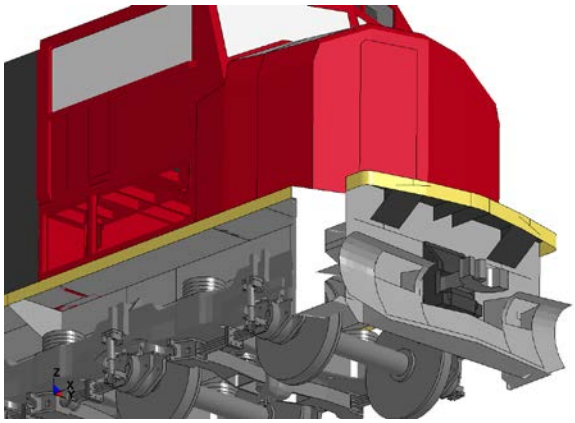

(b) Modified anti-climber

Figure 22. Original and modified anti-climber.

The front draft box was modified based on information provided by EMD and the resulting draft box model is shown in Figure 23 (the original QNA coupler and draft gear models were still used). The original connections were removed and the draft box was attached to the underframe with a weld zone that allows for failure. The rear draft box was replaced with the front draft box design and a coupler, stairs, and breastplate were added to the rear of the locomotive. The draft box was modeled with 0.5-inch elements to better capture failure of the draft box and its components.

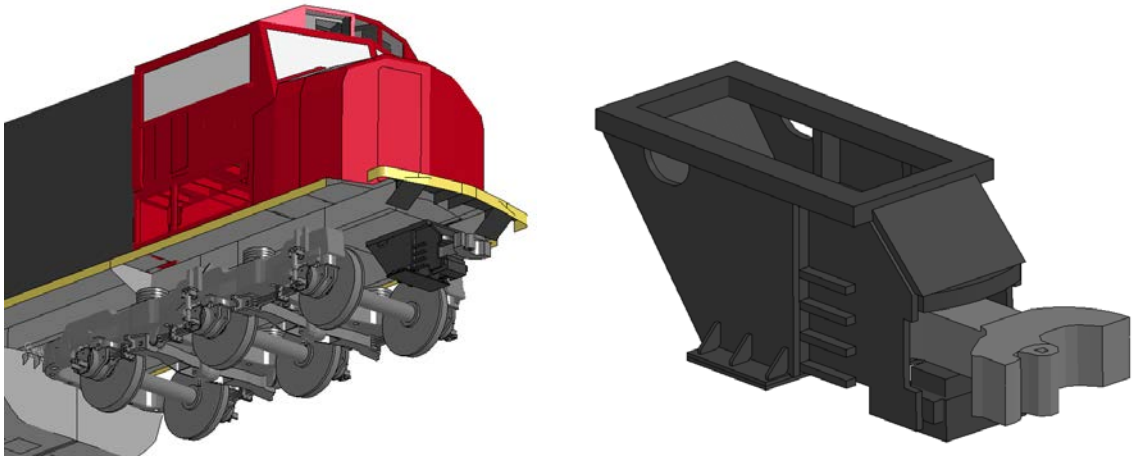

Figure 23. Modified draft box. The snow plow, breastplate, and stairs have been removed from the picture on the left to show the draft box and coupler.

Cargo equipment mass was added to get the locomotive weight to about 420,000 lb. In the original model, the long hood components were modeled with point masses distributed throughout the underframe and at five locations within the long hood. In the FE model, we added three parts within the long hood to represent the engine, radiator, and internal air filter, as shown in Figure 24. The resulting modified FE model has about 470K elements.

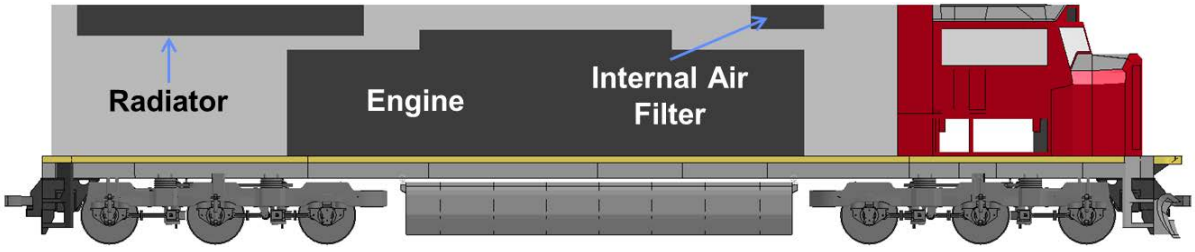

Figure 24. Locomotive showing cargo masses. The long hood is shown as transparent.

3.5 Tractor-Trailer Model Development

The tractor-trailer FE model was provided by the National Transportation Research Center Inc. (NTRCI). The NTRCI has various tractor and trailer FE models that they have validated against full-scale crash tests against barriers. For these analyses, we used the 129-inch wheelbase tractor

with a 48-foot trailer. The total tractor-trailer weight is 80,000 lb. The model is shown in Figure 25. The tractor-trailer weight is 28,819 lb and the ballast weight is 50,922 lb for a total weight of 79,741 lb. the ballast represents concrete highway barriers surrounded by foam. In the tractor-trailer side view in Figure 25, the trailer sides are shown as transparent to visualize the ballast. The original tractor-trailer model has approximately 380,000 elements and was created in units of mm-Mg-s. Only minor changes to the model were made, apart from converting to the model to an in-lb-s system of units.

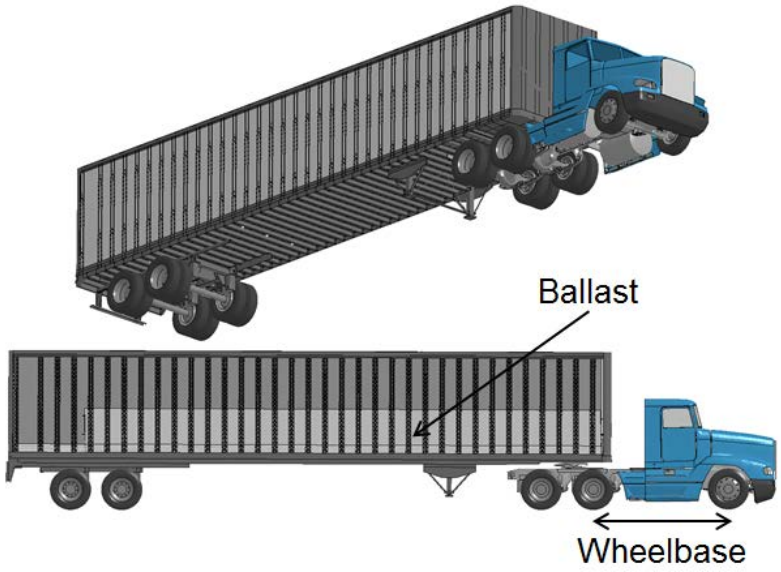

Figure 25. Tractor-trailer FE model from NTRCI.

4 Analysis of Collision Load Cases

4.1 Head-on Train Collision Load Case

A specific train crash was selected as a suitable example for the head-on collision load case. The collision conditions selected are those of the Collision of Two Canadian National Railway Freight Trains near Two Harbors, Minnesota on September 30, 2010 [47].

The collision occurred when the Canadian National Railway freight train U78982-30 (southbound train), consisting of three locomotives and 116 railcars loaded with iron ore, collided head on with CN freight train U78983-30 (northbound train), consisting of three locomotives and 118 empty iron ore railcars. According to the event recorders, the southbound train was traveling at about 15 mph when, about 12 seconds before the collision, the brakes were applied and the train's speed decreased slightly, to about 13 mph, at the time of collision. The northbound train was traveling at about 39 mph prior to braking, about 10 seconds before the collision, and the train's speed decreased to about 29 mph at the time of the collision. A total of three locomotives and 14 railcars derailed. All five crewmembers on the two trains were injured and transported to hospitals. Four crewmembers were treated and released; one crewmember remained hospitalized for further treatment. An overview of the condition of the two colliding trains is shown in Figure 26.

The collision represents a good example for a head on collision since it is a severe collision but still within limits that are survivable by the crew if the collision responses remain controlled and the collision energy dissipated. The approach to analyzing this load case will be to first analyze the collision as it occurred, to validate the models. The collision will then be modified to include an LNG tender in one or both trains and the collision conditions will again be analyzed to assess the impact of the tender on the collision behaviors and crash safety for this load case.

One advantage of this collision scenario is that the trains have a similar set of vehicles and only two types of cars are involved (locomotives and iron ore hoppers). To accurately model the entire collision scenario would require models for both the locomotive and iron ore cars. However, previous research by the Volpe National Transportation Systems Center has determined that the trailing hopper cars, which are smaller, lighter, and weaker than the locomotives, only provide a small contribution to the collision forces of the locomotives. As a result, the majority of the collision scenario of interest can be analyzed by simply modeling the collision of the three locomotives in each train.

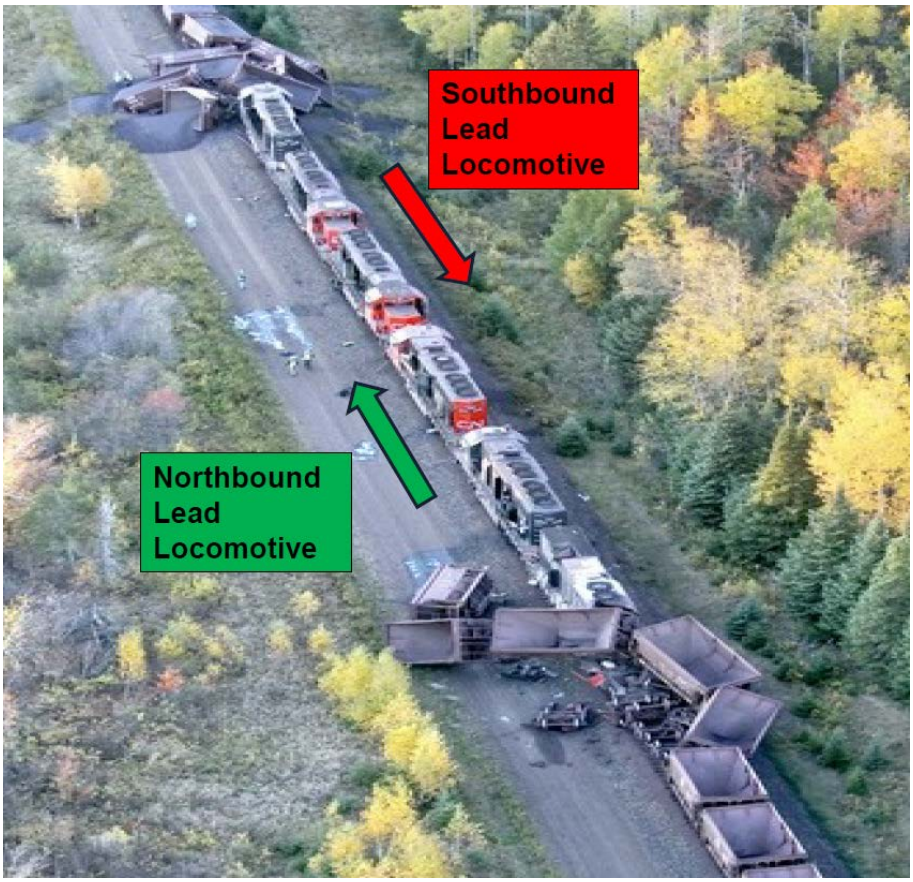

Figure 26. Collision of Two Freight Trains near Two Harbors, MN on September 30, 2010.

4.1.1 Two Harbors Collision Simulation

The locomotive model was used to analyze the impact conditions of the Two Harbors collision as a validation scenario for the model. The complete FE model of the Two Harbors locomotive collision scenario has about 2.9 million elements and on twelve processors takes about 10 days to complete the first 500 ms of the collision (with an initial 100 ms of gravity initialization). The FE calculation setup is shown in Figure 27 with three northbound locomotives (NB L1, L2, and L3) on the left and three southbound (SB L1, L2, and L3) locomotives on the right. In both trains, the trailing locomotive is rear facing. The northbound locomotives were initialized at 29 mph and the southbound locomotives at 13 mph.

Figure 27. Locomotive collision setup with northbound locomotives on the left and southbound locomotives on the right.

The calculated velocity histories for each of the six locomotives in the Two Harbors collision are shown in Figure 28. In addition to the FE results, the predicted velocity histories from the Volpe

Center lumped mass analyses are shown in Figure 28 and the two analyses methodologies are in good agreement. The crush between the two leading locomotives occurs in the initial 100 ms and the subsequent interaction of the leading and secondary locomotives occurs primarily between 100 and 300 ms. Both trailing locomotives in the FE analyses are decelerating at a slower rate (see red and purple curves) compared to the Volpe lumped mass analysis.

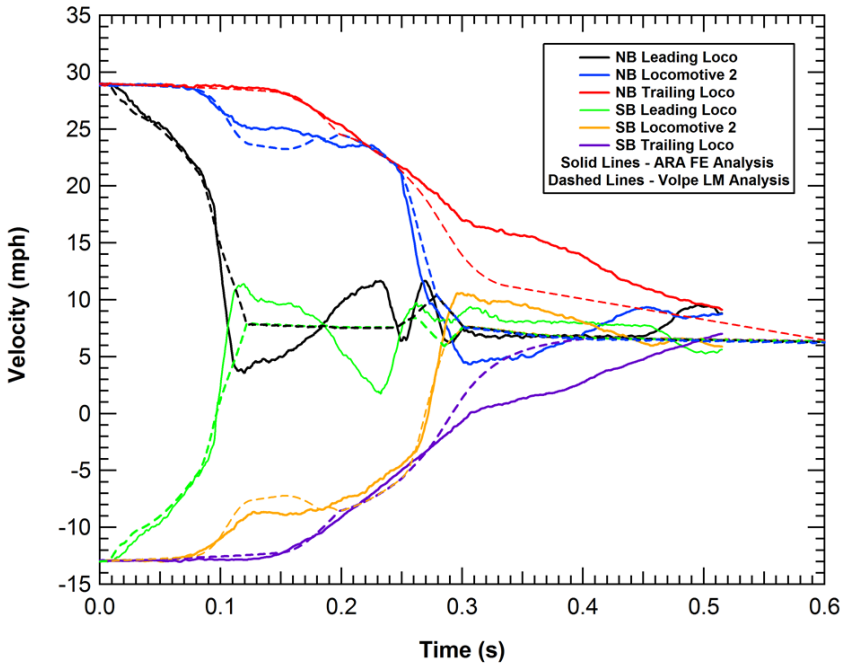

Figure 28. Locomotive velocities compared to Volpe analysis.

Additional details of the collision behaviors can be obtained by comparing the predicted collision forces between the various locomotives. Forces for the collision interface and the northbound L1-L2 and L2-L3 interfaces are shown in Figure 29 and Figure 30, respectively. The timing and character of the calculated force histories between the FE analysis and the Volpe lumped mass analyses are in good agreement.

The largest discrepancy is in the force magnitude between the two colliding locomotives. The finite element model has a significantly higher dynamic crush strength for the locomotive underframe than assumed in the lumped mass model. As a result, the FE analyses calculate crash forces as high as 17 million lbs compared to the lumped mass analyses that cap these forces at 10 million lbs. Although this discrepancy magnitude is significant for the forces at the collision interface, is has a much smaller effect on subsequent interfaces that would be the critical locations for the tender collision behavior.

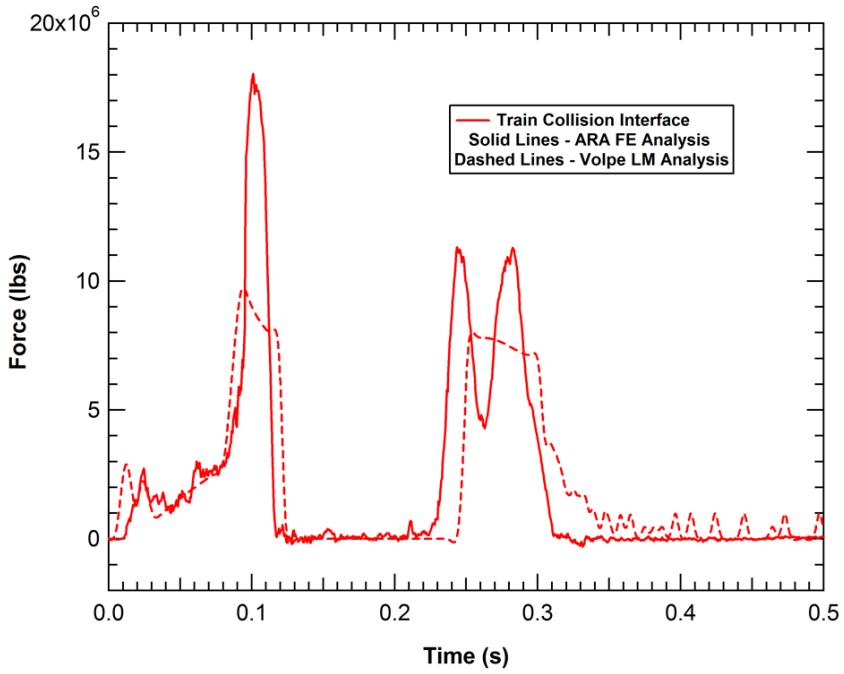

Figure 29. Forces at the collision interface.

The calculated fringes of plastic strain in the locomotives at the various collision interface positions in the northbound locomotives are shown in Figure 31. In the primary collision interface, both draft gear boxes failed and both anti-climbers were destroyed (either crushed solid or sheared under). Damage was evident to the breast plates and stepwells. The locomotives remained essentially in-line. In the secondary collision interface, the rear draft gear box in the first locomotive (L1) was heavily damaged and the front draft gear box in the second locomotive (L2) failed. The anti-climber was crushed and rode over the front locomotive (L1) underframe. Significant damage was evident in the breast plates and stepwells and the locomotives remained essentially in-line. In the third collision interface, both draft gear boxes failed. At 500 ms in the calculation, the breast plates were not yet fully engaged and the locomotives remained essentially in-line.

These collision behaviors are consistent with those observed in the Two Harbors collision as seen in Figure 32. Wherever possible, we are working to validate the FE analyses with the observable damage seen in the two harbors collision. The combination of matching the observed response and the agreement between the FE and lumped mass analyses each help provide confidence in the quality of the locomotive FE model.

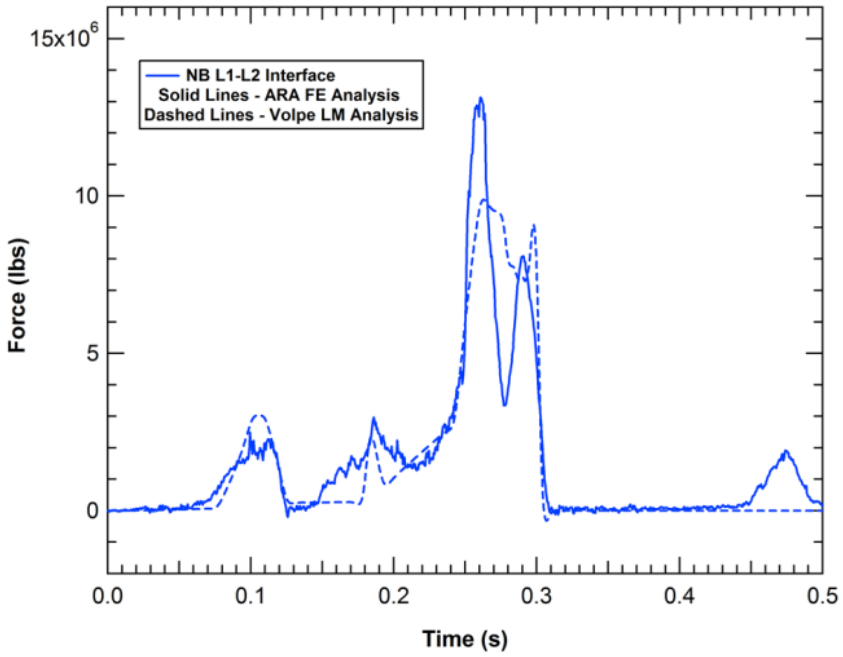

(a) Collision forces between the first and second locomotives

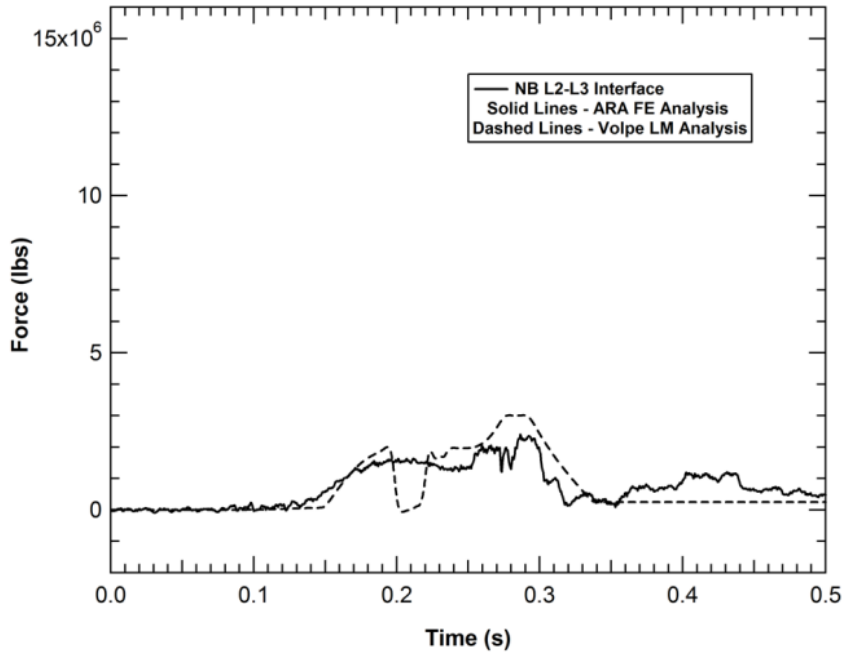

(b) Collision forces between the second and third locomotives

Figure 30. Forces at the secondary collision interface positions in the northbound train.

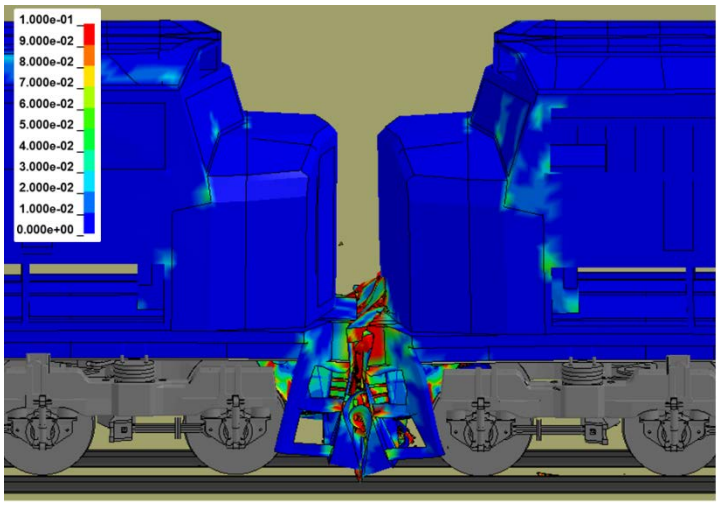

(a) Primary collision interface.

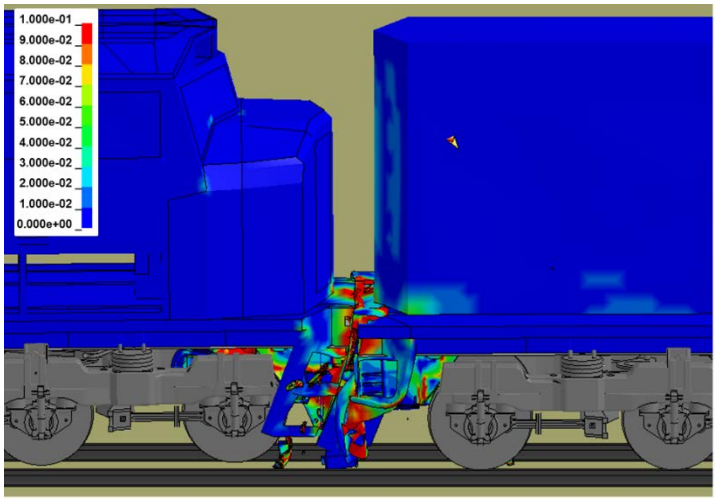

(b) NB L1-L2 interface.

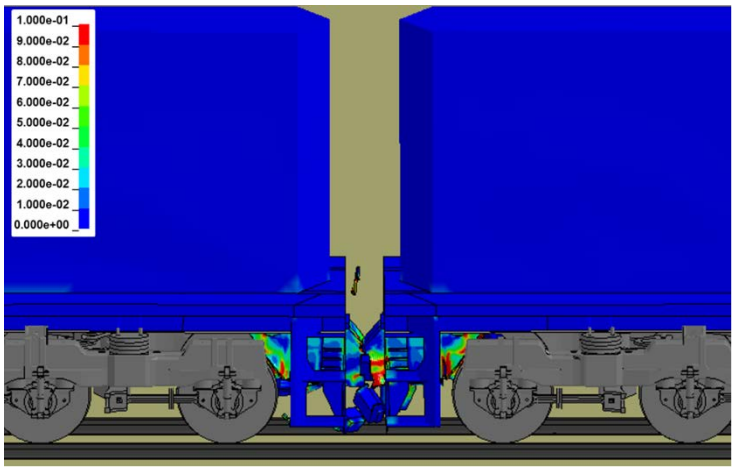

(c) NB L2-L3 interface.

Figure 31. Calculated damage and plastic strain in the Two Harbors collision scenario.

(a) Damage at the leading locomotive end.

(b) Damage at the NB L1-L2 interface.

Figure 32. Photographs of locomotive damage in the Two Harbors collision scenario.

4.1.2 Train-to-Train Collision Simulation with the Legacy Tender 1

The collision scenario used for analysis of the LNG tender response in the Two Harbors crash scenario is shown in Figure 33. The calculation setup is obtained by replacing the LNG tender model in the position of the original southbound L2 locomotive.

Figure 33. LNG tender model setup for the Two Harbors collision scenario.

The calculated velocity histories for each of the five locomotives and one tender in the Two Harbors collision are shown in Figure 34 along with the velocity histories form the six locomotives collision analysis. The velocity histories for the northbound locomotives and the leading southbound locomotive are in good agreement until about 250 ms (see black and green curves). The tender mass is significantly lower compared to the locomotive mass, which contributes to a reduced deceleration of the trailing southbound vehicles. The velocity difference at 320 ms after impact is about 17 mph.

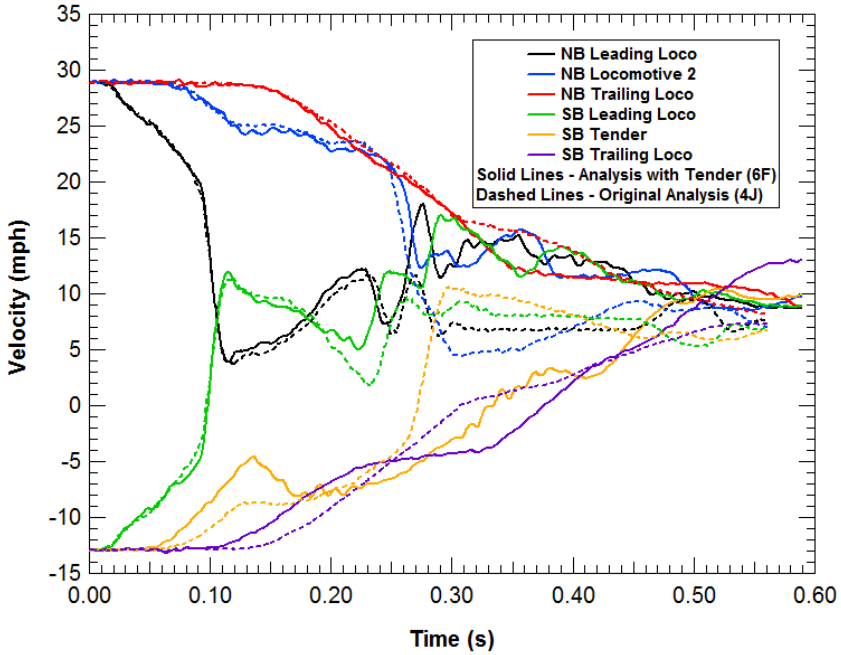

Figure 34. Locomotives and tender velocities compared to original (no tender) Two Harbors collision analysis.

The locomotive collision interface response is very similar to the original six locomotive Two Harbors analysis. The response is shown in Figure 35. Both draft gear boxes failed and both anti-climbers were either crushed solid or sheared under. Damage was evident to the breast plates and stepwells. The locomotives remain essentially in-line. Figure 36 shows the tender to leading locomotive collision interface at 530 ms after impact. The underframe heights of the locomotive and tender are not compatible causing the locomotive underframe to override the tender underframe structure.

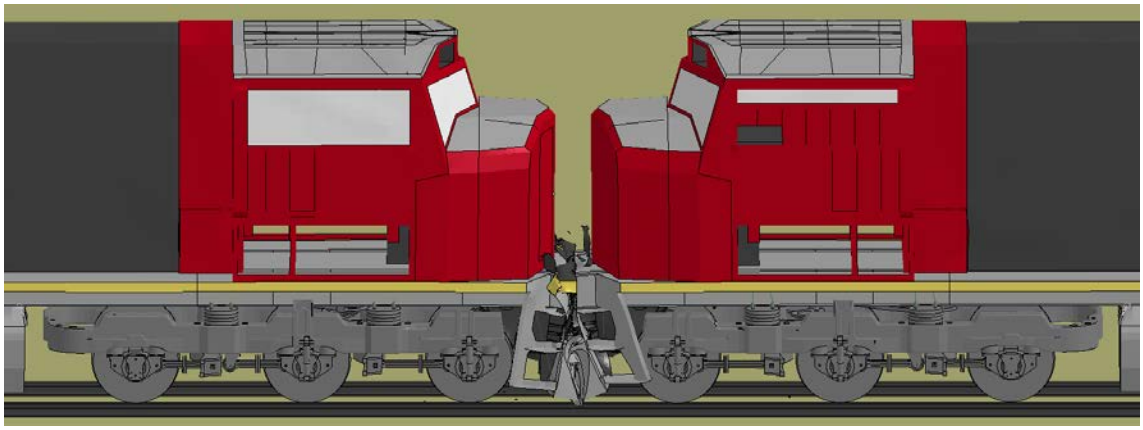

Figure 35. Primary collision interface at 530 ms after impact.

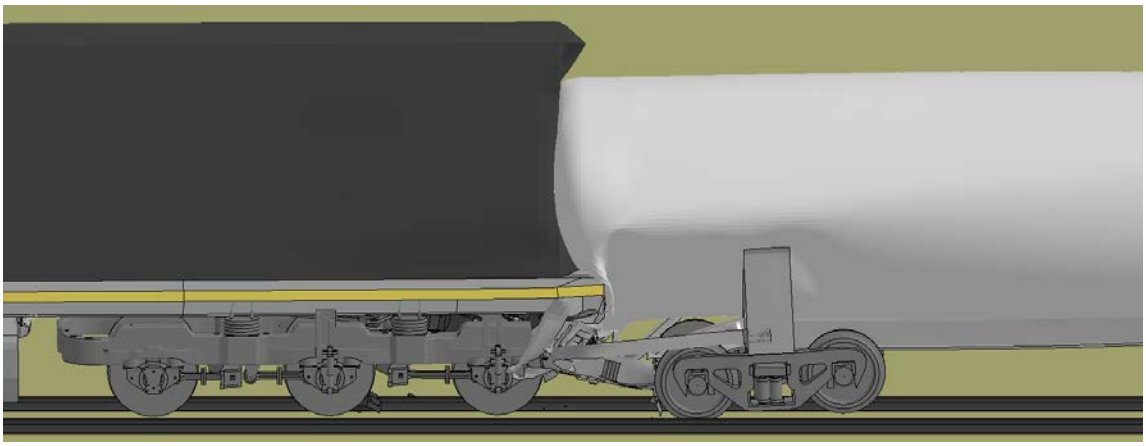

Figure 36. Tender to leading locomotive collision interface at 530 ms.

An underside view of the tender to leading locomotive interface at various impact times is shown in Figure 37. At 200 ms (a), the leading locomotive rear draft box has mostly failed. The tender coupler has impacted the striker face and breast plate. There is plastic deformation in the tender sill, but the sill continues to carry most of the collision loads. At 250 ms (b), the locomotive draft box has completely failed. The tender coupler has punched through the striker face and breast plate causing the tender underframe to impact the locomotive breast plate. At 300 ms (c), the tender underframe structures have begun to collapse and the tender jacket head has impacted the locomotive long hood and underframe. At 450 ms (d), the tender underframe structures continue to crush and the impact of the tender draft gear on the locomotive cripples the center sill. The inner tank impact occurs around 370 ms.

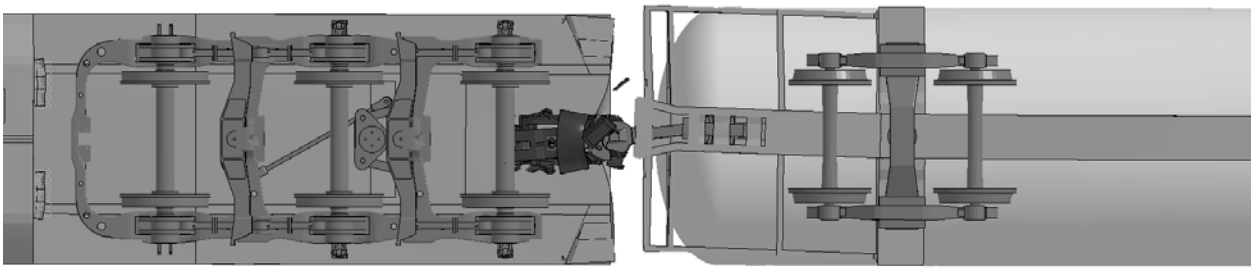

(a) 200 ms.

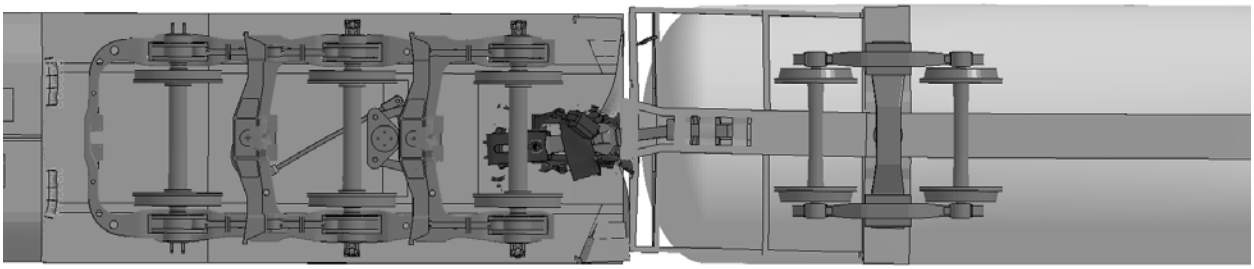

(b) 250 ms.

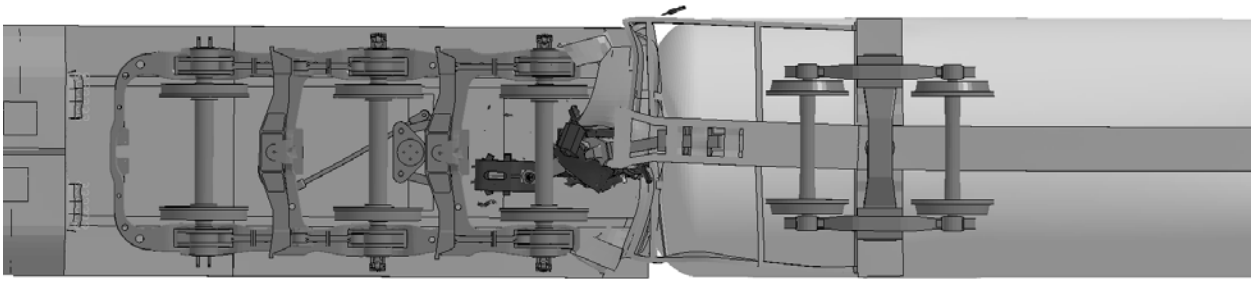

(c) 300 ms.

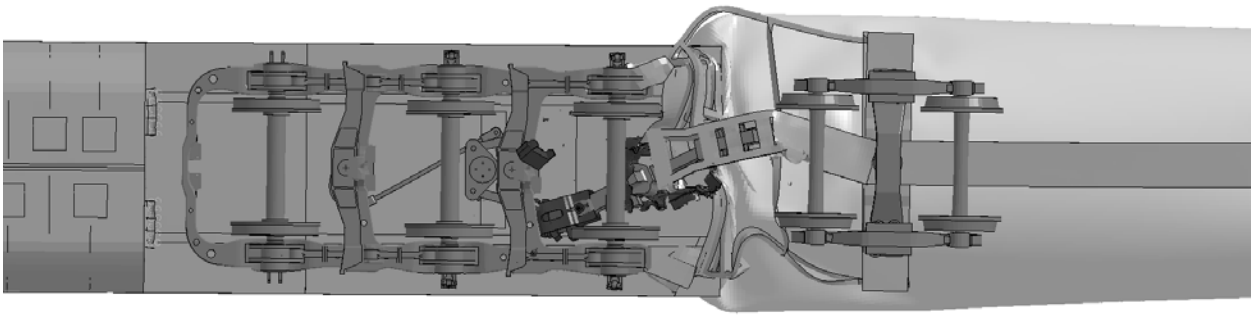

(d) 450 ms.

Figure 37. Underside view of leading locomotive to tender interface at various impact times.

The final crush mechanisms include large displacement of the jacket head and contact and denting of the inner tank head is also observed. The maximum indentation on the inner tank is approximately 18 inches. The calculated fringes of plastic strain on the tender inner tank head at

the collision interface are shown in Figure 38. The maximum plastic strain magnitude calculated on the inner tank head is 23%. This level is still well below the expected fracture strain threshold for 304LSS at cryogenic temperatures (as shown previously in Figure 13).

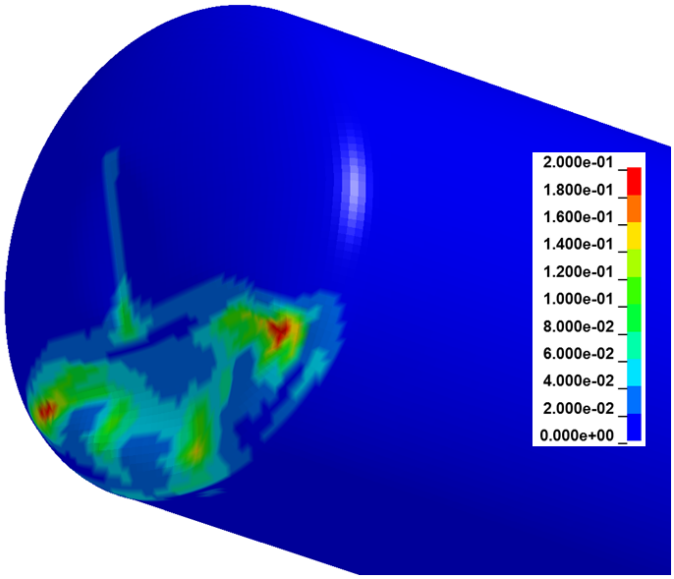

Figure 38. Fringes of plastic strain on the inner tank head at the collision interface at 530 ms.

Forces for the tender collision interface to the leading locomotive are shown in Figure 39. A few key collision events are indicated on the collision force history. The locomotive draft box failure occurs at approximately 6-inches displacement (120 ms) with a load of 2.2 million pounds. Direct loading through the tank initiates around 40-inches of displacement (250 ms).

To further investigate the collision loads in the tender, the forces were extracted from the tender model through various cross sectional force definitions. Two force definitions were created for the total transmitted force and the force transmitted through the center sill at a position near the end of the tender. Time histories for these two cross-sectional force definitions are compared in Figure 40. The. The comparison shows that the majority of the forces at this interface are transmitted through the center sill of the tender. Only when the tender jacket head contacts with the leading locomotive (about 250 ms), does a significant alternative load path develop for the collision loads.

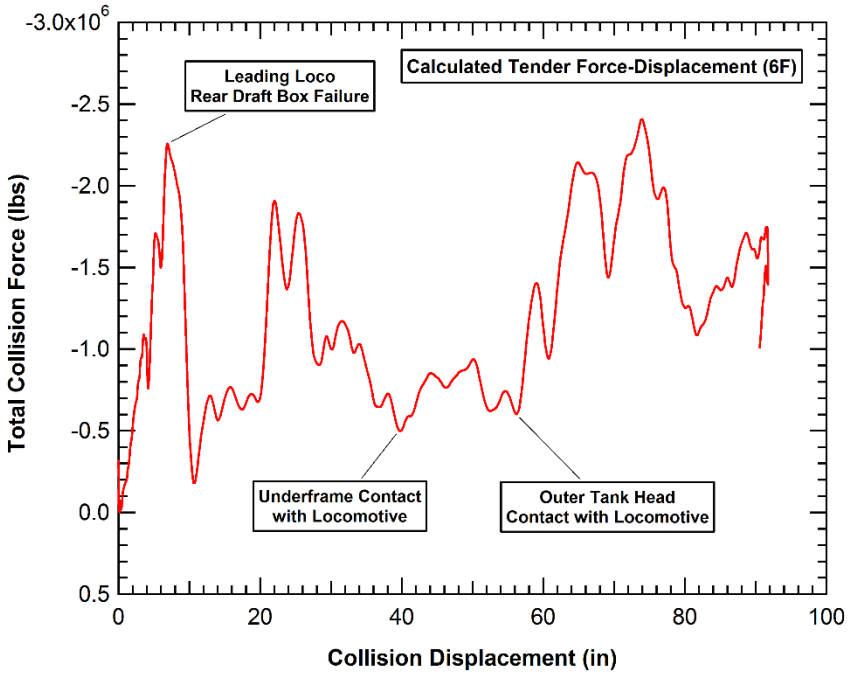

Figure 39. Tender force-displacement curve at the collision interface.

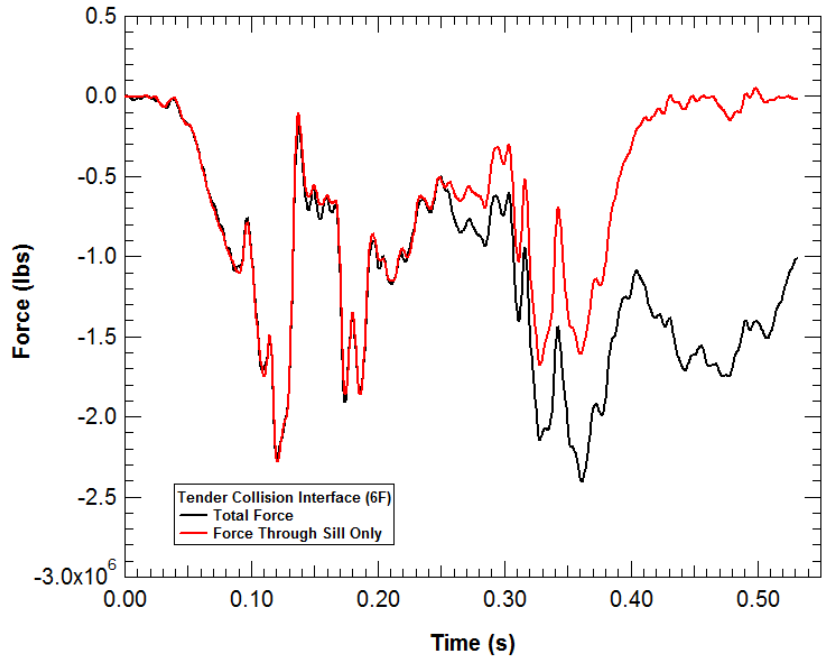

Figure 40. Forces at the tender to leading locomotive collision interface.

Integrated energy dissipation was added to the force-displacement curve and shown in Figure 41. About half of the energy is dissipated before the tank impacts the locomotive structures (about 250 ms).

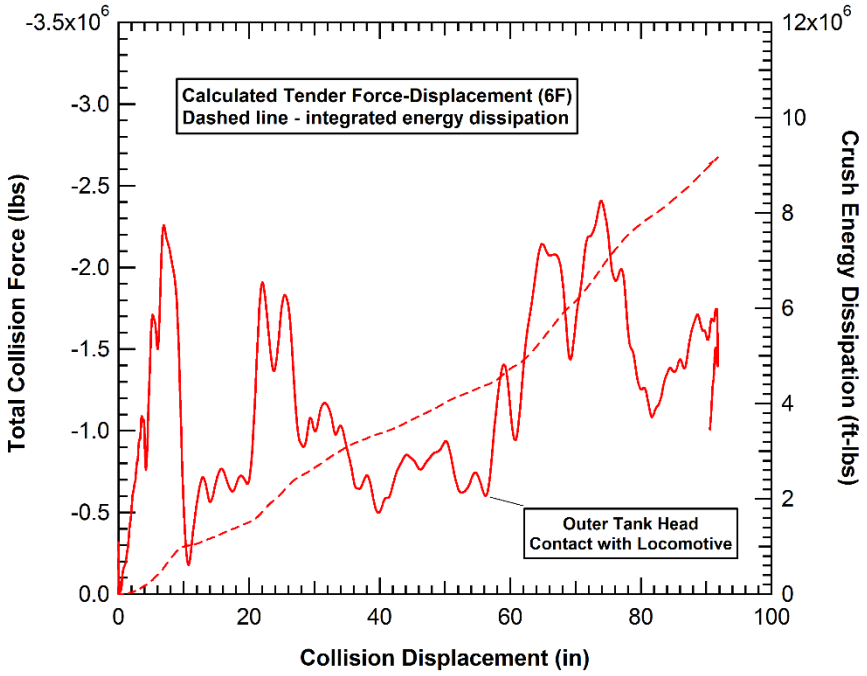

Figure 41. Force-displacement curve and integrated energy dissipation at the tender collision interface.

The damage at the tender to trailing southbound locomotive interface is minimal. A side view of this interface at 530 ms is shown in Figure 42. Plastic deformations are evident in the tender sill, but the sill is still able to support significant collision loads. The calculated force history for the rear collision interface to the trailing locomotive is shown in Figure 43. All the forces throughout the collision are transmitted through the center sill of the tender.

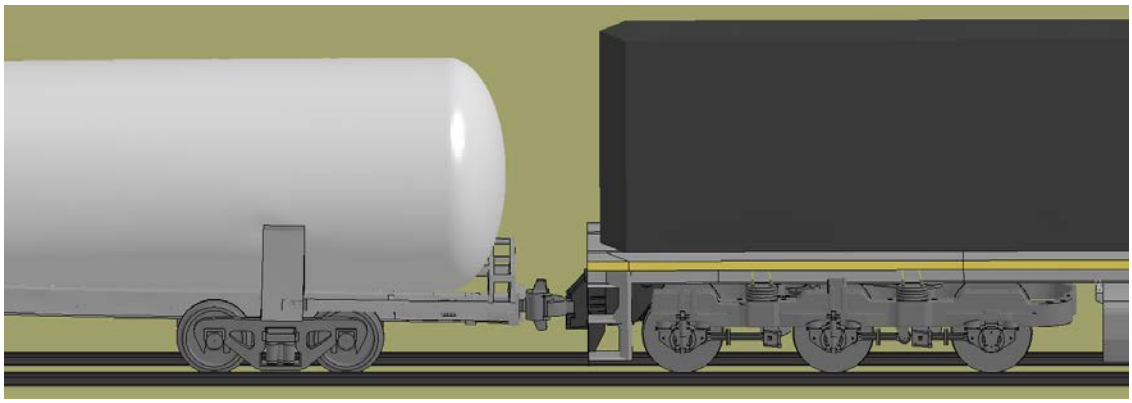

Figure 42. Tender to trailing locomotive interface at 530 ms.

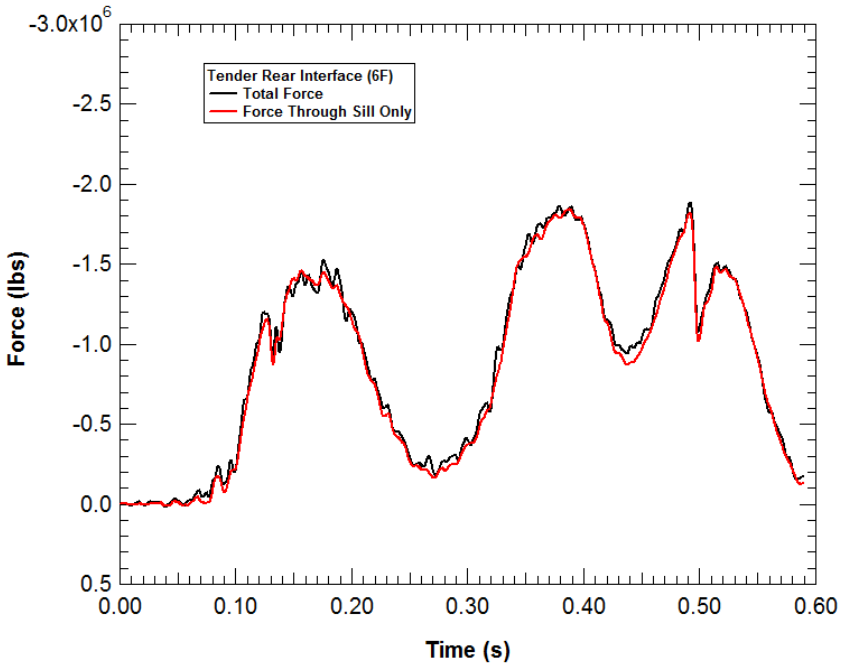

Figure 43. Forces at the tender to trailing locomotive collision interface.

4.1.3 Train-to-Train Collision Simulation with the Enhanced Tender design

The collision scenario used for analysis of the Future LNG tender response in a train-to-train crash scenario is shown in Figure 44. The calculation setup similar to the previous tender collision scenario but the model has been modified to be a tender between two locomotives running into a rigid wall at 22.5 mph. This is approximately equivalent to a symmetric collision between two identical locomotive and tender configurations at a closing speed of 45 mph (twice the impact speed against the rigid wall). The primary difference of the simplified rigid wall scenario is that it does not allow for unstable behaviors such as an override of the colliding locomotives. However, these responses were not seen in the Two Harbors collision or in any of the train-to-train simulations performed. As a result, the collision environment on the tender in this rigid wall scenario should be more severe in this collision than in the 42 mph Two Harbors collision scenario. For comparison the scenario was also used to calculate the collision response for a 21.0 mph collision (42 mph closing speed).

Figure 44. LNG tender model setup for the Two Harbors collision scenario.

The calculated crash behavior between the leading locomotive and the tender for the 22.5 mph rigid wall impact is shown in Figure 45. The response exhibits a more controlled crushing of the tender end structures that absorb the required collision at smaller displacement levels. There is no direct contact between the tender jacket head and the locomotive. A small amount of denting occurs from an end frame plate that deforms upward and is pushed into the jacket head. However, this response could be eliminated with additional design modifications.

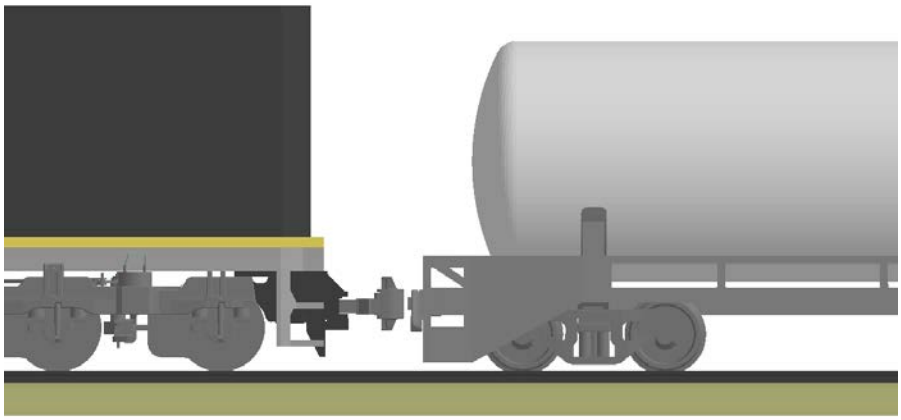

(a) Model geometry

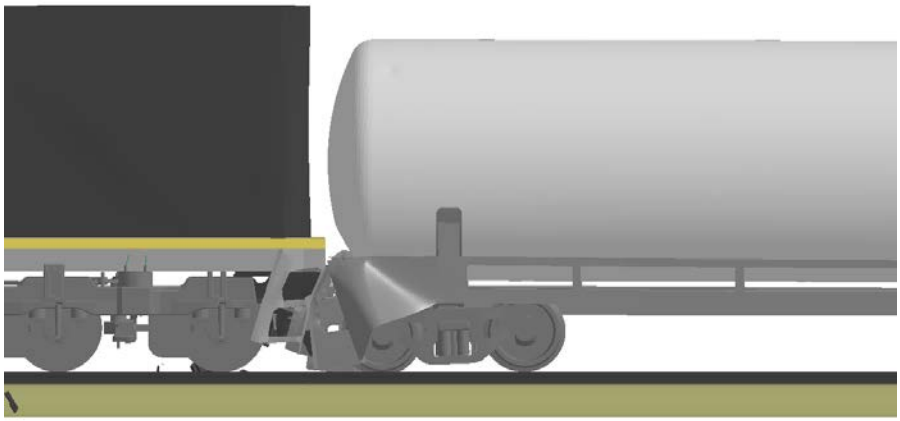

(b) Crash response at the leading locomotive interface

Figure 45. Analysis of the train crash scenario with the enhanced tender design (45 mph closing speed).

The corresponding calculated plastic strains in the jacket for the 22.5 mph rigid wall collision (45 mph closing speed) are shown in Figure 46. The damage is localized to the dent where the end frame was pushed against the jacket head and the maximum plastic strain is 22%. At this damage level, we would not expect the jacket to be breached. The response of the inner tank is completely elastic.

The additional calculation was performed with a 21.0 mph rigid wall collision (42 mph closing speed) to more closely match the severity of the Two Harbors collision. The corresponding calculated plastic strains in the jacket for the 21.0 mph collision are shown in Figure 47. The maximum plastic strain is 7% and mostly an artifact of a specific inner tank support design. Again, the response of the inner tank is completely elastic.

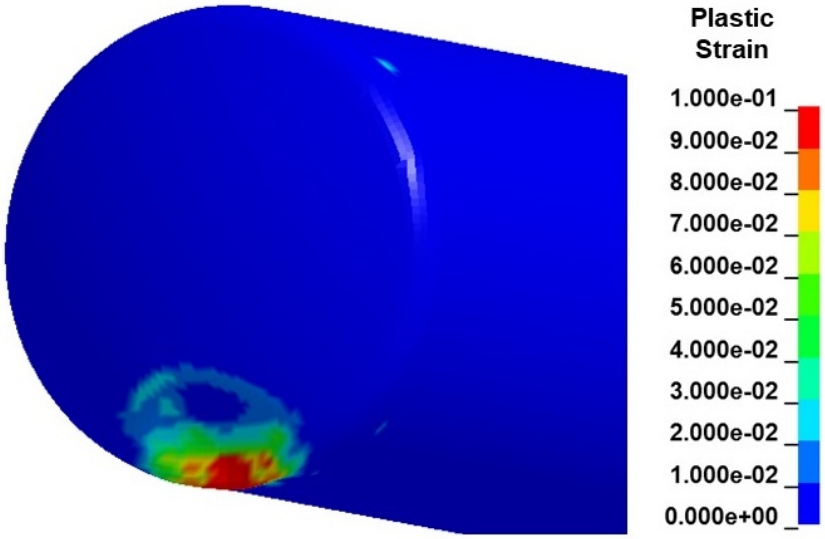

Figure 46. Calculated jacket plastic strains for the train-to-train collision scenario (45 mph closing speed).

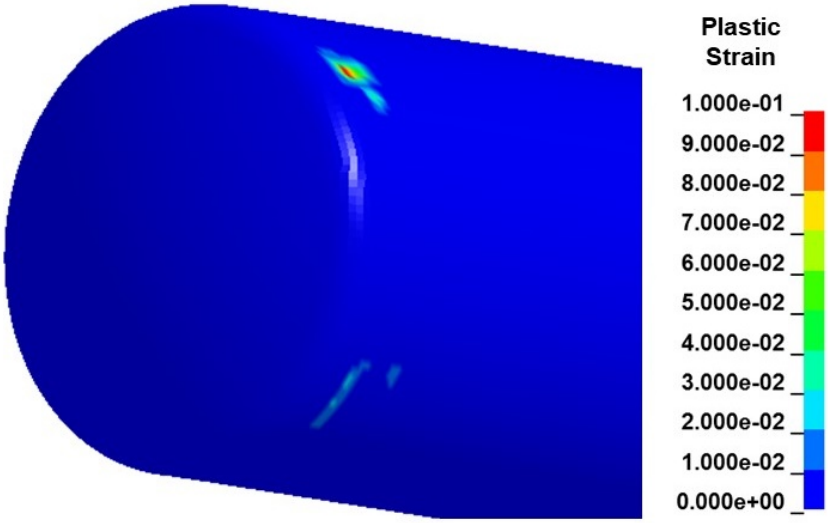

Figure 47. Calculated jacket plastic strains for the train-to-train collision scenario (42 mph closing speed).

4.2 Grade-Crossing Collision Load Case

The grade crossing collision scenario selected was a tractor-trailer impacting the LNG tender at a grade-crossing as shown in Figure 48. The tractor-trailer is traveling at 40 mph and the tender is assumed to be stationary and coupled to the locomotives at both ends.

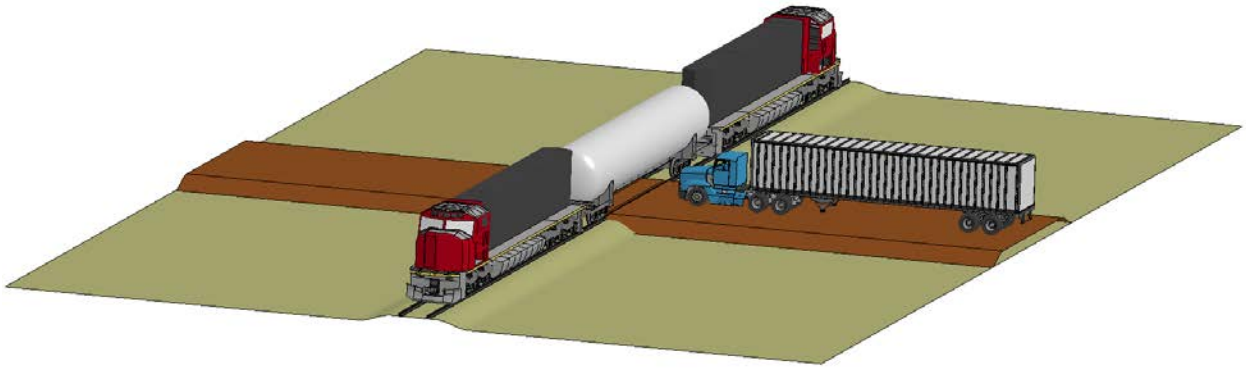

Figure 48. Tractor-trailer into LNG tender at grade-crossing collision scenario.

4.2.1 Initial Legacy Tender Grade Crossing Impact Response

The initial analysis reported here is for an impact point centered on the tender without protective housings or side impact protection. A cross section through the impact plane on the tender illustrating the collision response (at approximately maximum indentation) is shown in Figure 49. The cab of the tractor is completely crushed and the ballast slides forward and collides against the trailer. The corresponding crash velocity histories for the tractor-trailer engine and ballast are shown in Figure 50. The tractor engine comes to rest in approximately 200 ms and the ballast in 350 ms.

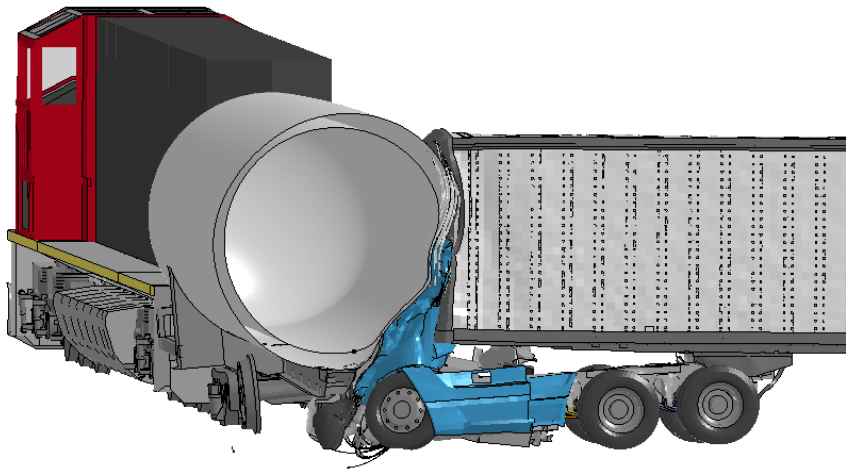

Figure 49. Tractor-trailer impact response on the tender.

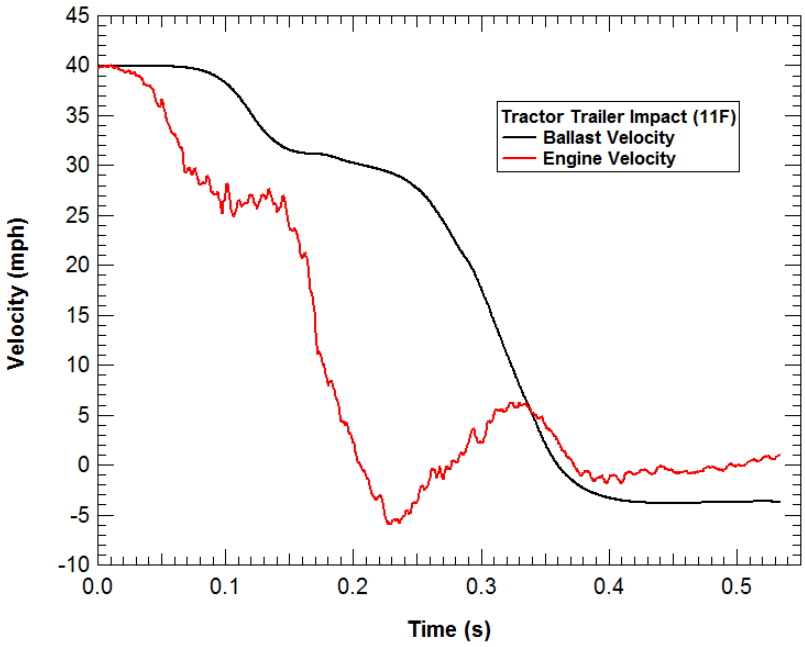

Figure 50. Tractor-trailer deceleration from impact against the tender.

The calculated plastic strains in the jacket and inner tank are shown in Figure 51. The maximum plastic strains in the jacket and inner tank for this collision were 12% and 13%, respectively. We would not expect these damage levels to be sufficient to puncture either of the jacket or inner tank. Furthermore, the peak strains on the inner tank were influenced by an inner tank support structure that was located within the impact zone and would probably be reduced at other impact locations along the tank. The alternate concern that needs to be investigated further for this scenario would be the damage to any piping or equipment that may be located in the impact zone.

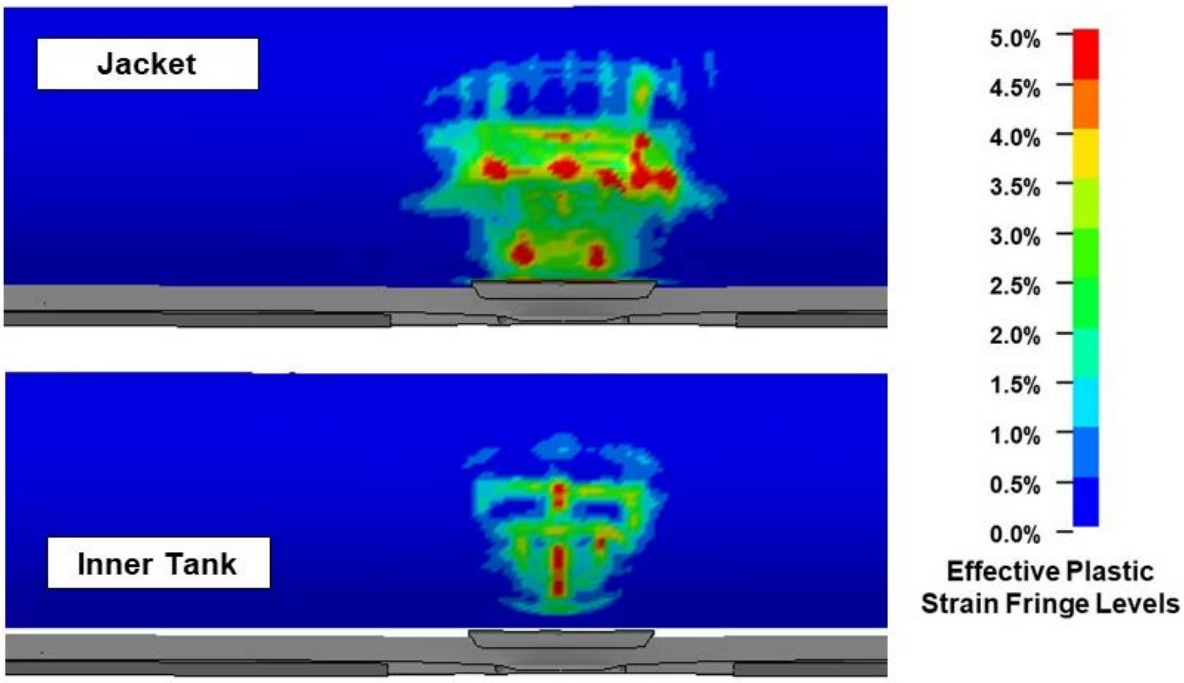

Figure 51. Calculated damage to the LNG jacket and inner tank for the grade crossing center impact.

Additional analyses were performed to investigate additional parameters for a grade crossing collision using this legacy tender model. One question is the response resulting from a different longitudinal impact point on the tender. An example collision scenario investigated is a collision centered on the bolster as shown in Figure 52. The corresponding calculated damage to the jacket and inner tank is shown in Figure 53. The maximum plastic strains in the jacket and inner tank for this collision were 7% and 6%, respectively. Thus, the bolster structures and truck provide a significant level of impact protection for the tender tank structures compared to the center impact configuration.

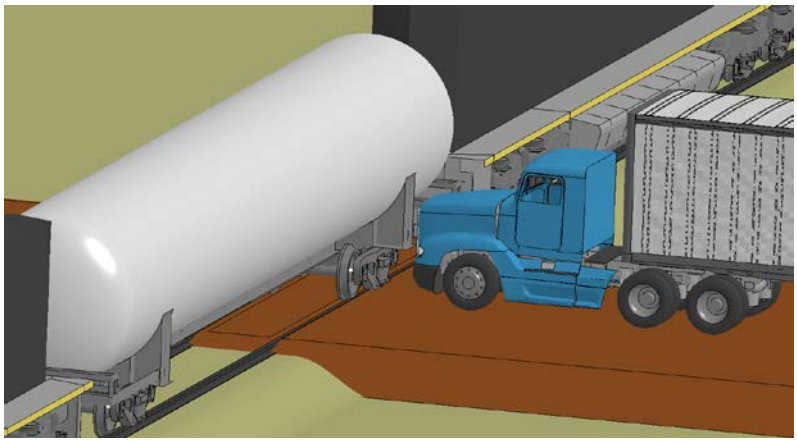

(a) Impact configuration

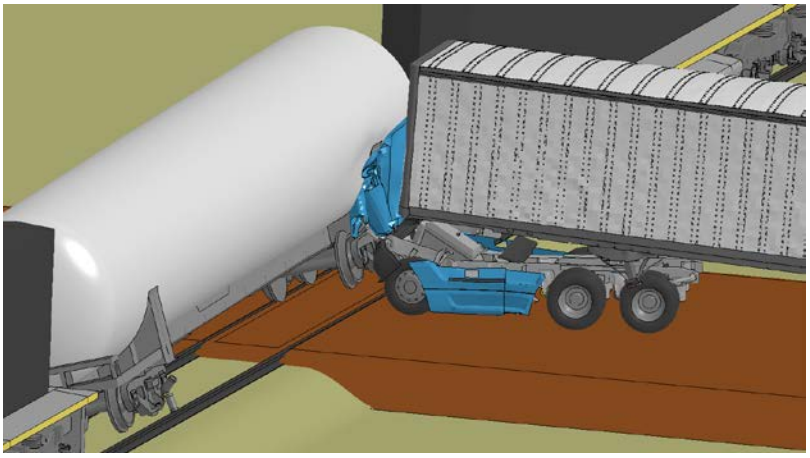

(b) Calculated collision response

Figure 52. LS-DYNA finite element model of the initial enhanced tender design.

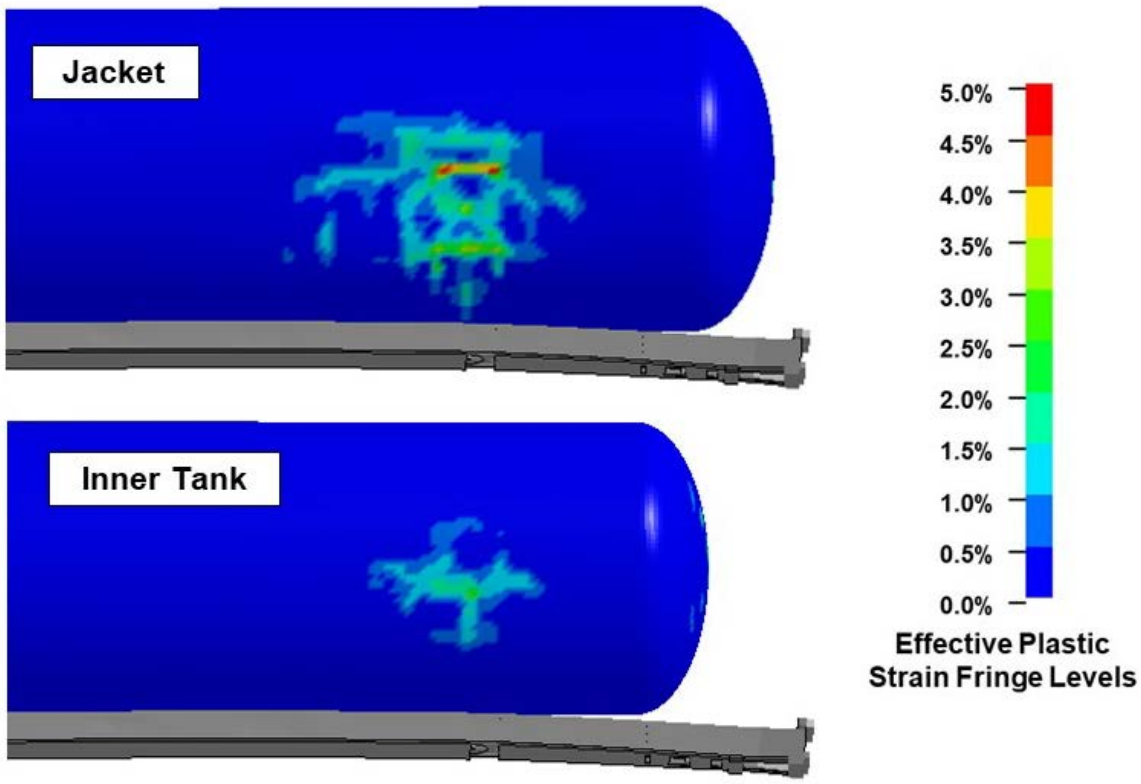

Figure 53. Calculated damage to the LNG jacket and inner tank for the grade crossing bolster impact.

4.2.2 Pipe Damage Analysis

Modifications to the tender models were made to assess schedule 40 piping for the grade crossing collision condition. Generic fill and liquid pipes were added to the tender model the tank bottom and top penetrations, as shown in Figure 54. These include both a 3-inch unpressurized fill pipe and a 2-inch pressurized liquid pipe. Initial analysis was performed that showed the non-reinforced protective housing design provided limited protection, and the fill line was crushed. A conceptual design was developed for added protection. Additional piping protection features modeled in this concept geometry were the dry break outside jacket penetrations and jacket skid protection, as shown in Figure 55. The breakaway connections were modeling through a tiebreak interface.

Figure 56 shows the results of a 40 mph side impact between the tractor-trailer and the stationary tender, with the protective housing transparent for viewing. The breakaways performed as expected, allowing disconnection without additional damage to the penetrating pipes. In Figure 57, the jacket has been removed as well to show the plastic strains within the jacket skid plates and internal pipes. The unpressurized fill line was partially crushed. This does indicate that reinforced protective housings will be needed for improved grade crossing impact protection.

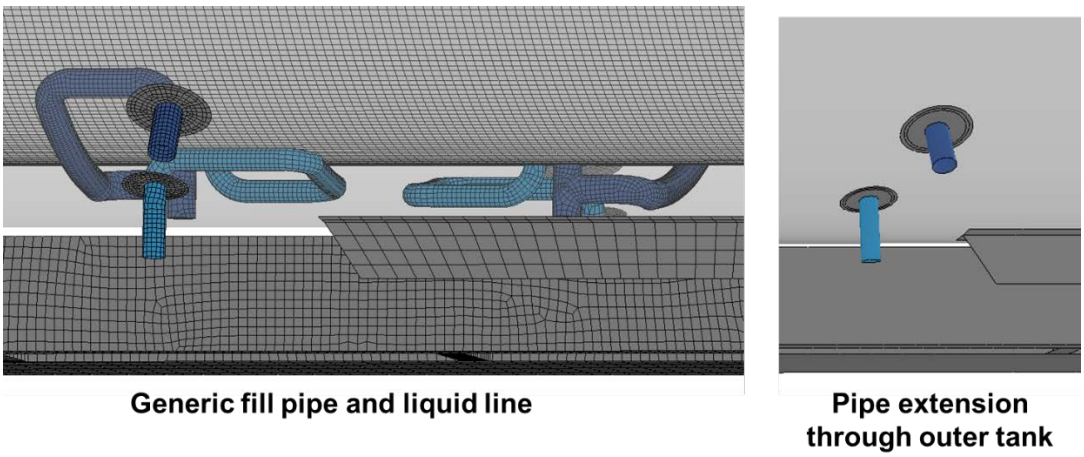

Figure 54. Pipe configuration.

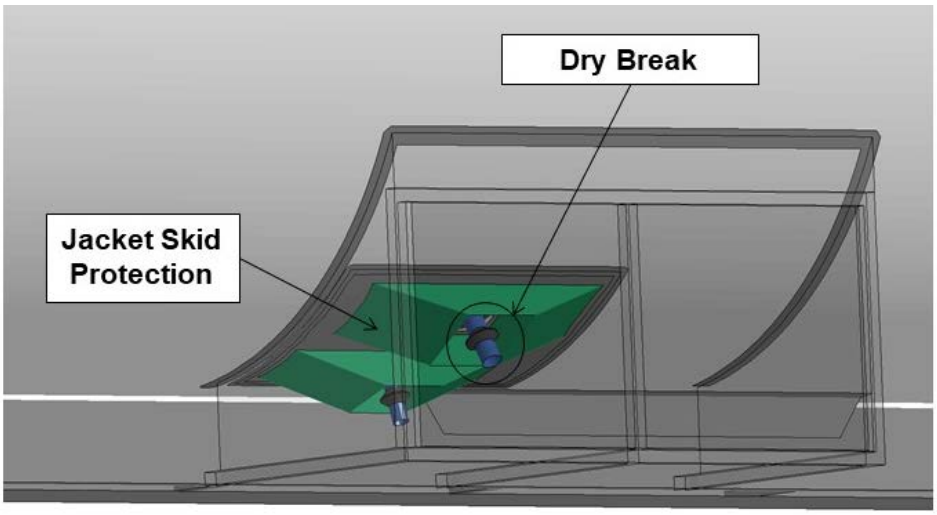

Figure 55. Tender piping model.

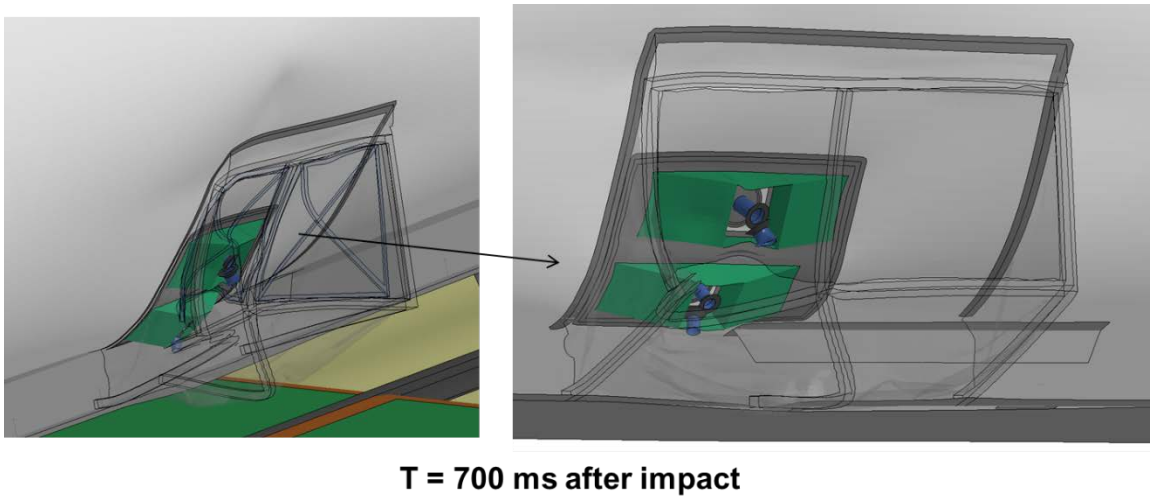

Figure 56. Side impact at 40 mph (protective housing shown transparent).

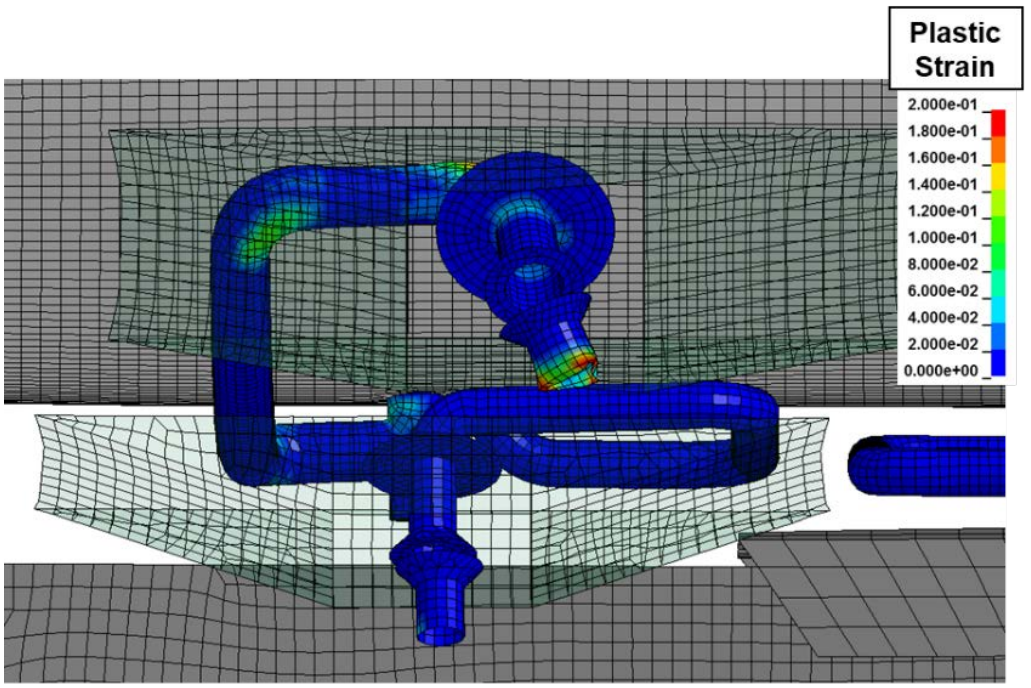

Figure 57. Plastic deformation after impact.

To demonstrate that this type of damage can be mitigated with an improved protective housing, a modified design was developed and an additional grade crossing analysis performed. The protective housing design was modified to include a reinforced structural frame. The original design used a simple construction with plates welded to an angle iron framework. In the reinforced design, shown in Figure 58, the angle iron frame is replaced with a 2-inch box section frame. In addition, the lower framework was further strengthened by stacking three levels of the box section frame vertically. This includes both the lower frame at the bottom of the protective housing outer face as well as rails that run from the outer face back to the center sill at the sides and middle of the protective housing.

An additional modification was made to the legacy tender design 1 model for this this analysis. The piping was modified to remove the bottom outlets in the cryogenic tank and replace them with a design that has the outlets at the top of the tank. As a result, there is a section of pipe running vertically in the annular space between the jacket and inner tank. The impact was on this section of pipe in the annular space (behind the protective housing) to evaluate the potential for damage to the piping.

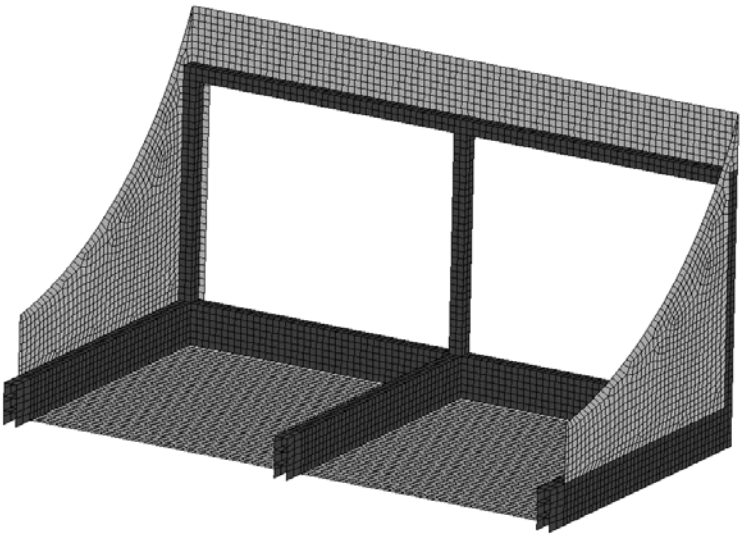

(a) Internal view of framing

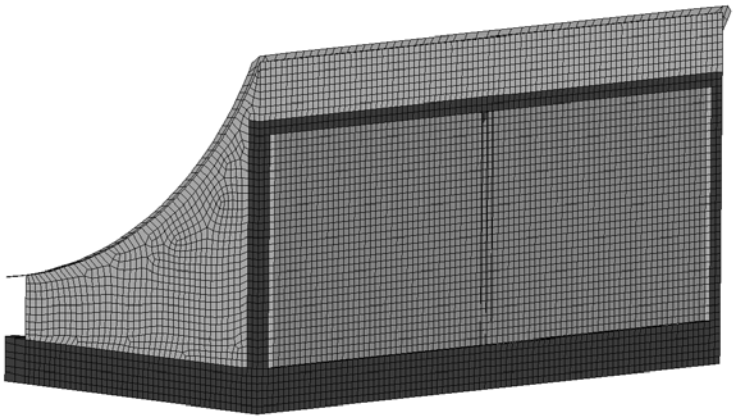

(b) External geometry

Figure 58. Reinforced protective housing with box beam frame.

The collision scenario and calculated impact response into the reinforced protective housing design is shown in Figure 59. The resulting impact damage to the reinforced protective housing is shown in Figure 60. The protective housing reinforcement significantly improved the impact strength, and the volume inside the protective housing was mostly unchanged. The corresponding damage to the piping is shown in Figure 61. The piping in the annular space has minimal damage from the side loading of the protective housing on the jacket. This design should meet requirements of physical and functional survivability of the piping.

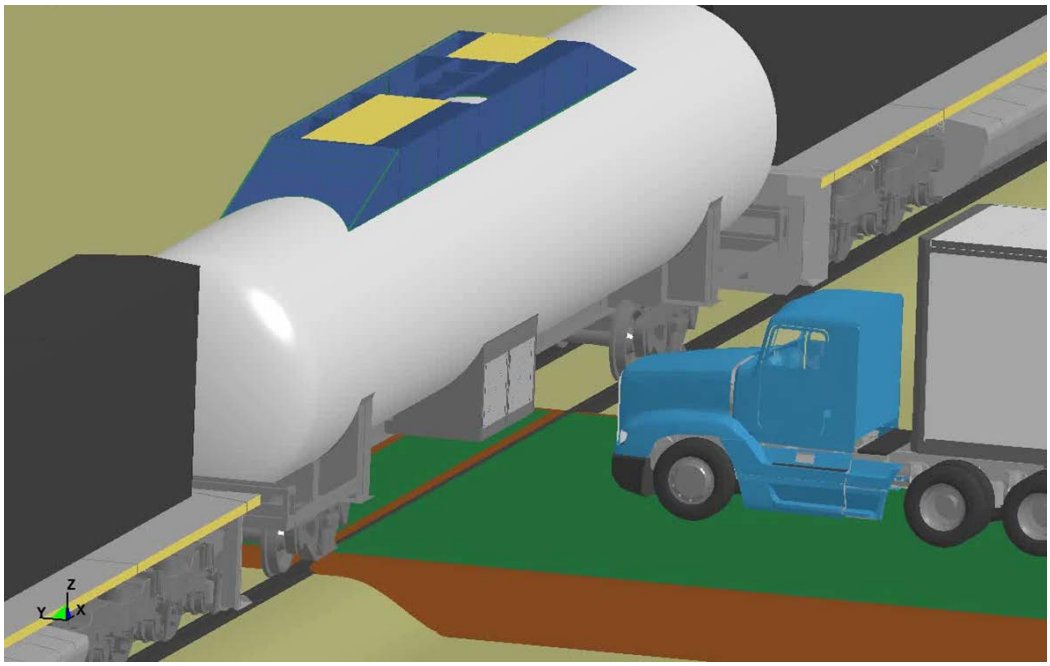

(a) Collision scenario

(b) Collision behavior

Figure 59. Calculated side impact collision response with the reinforced protective housing structure.

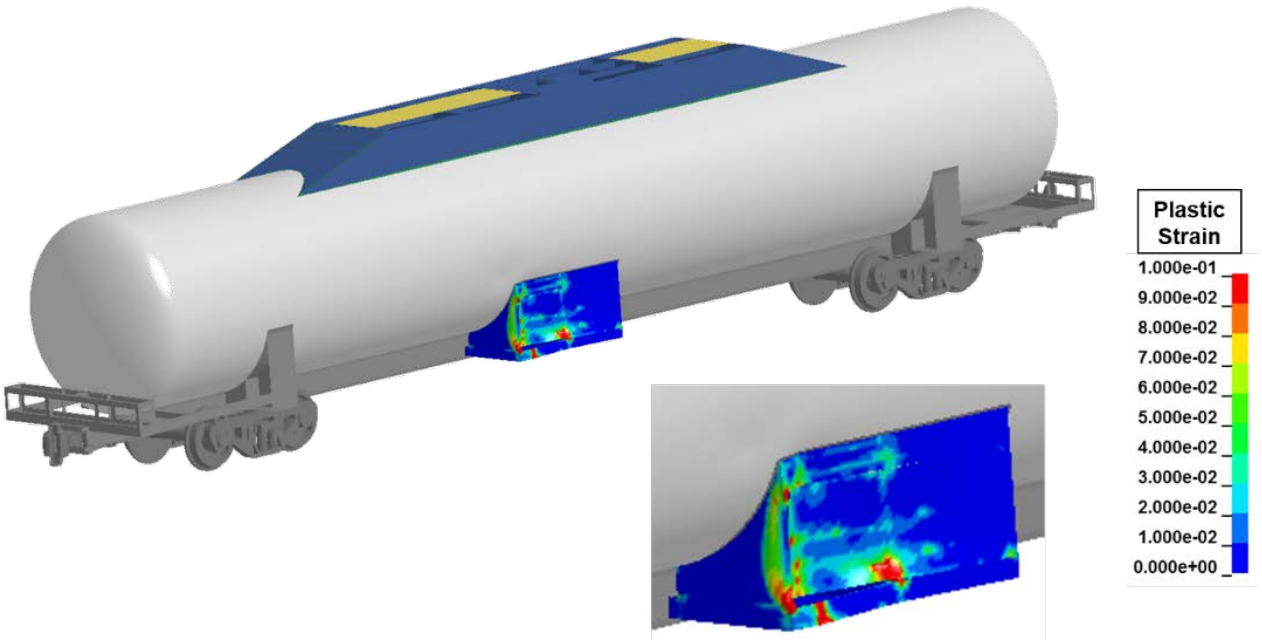

Figure 60. Calculated impact damage to the reinforced protective housing structure.

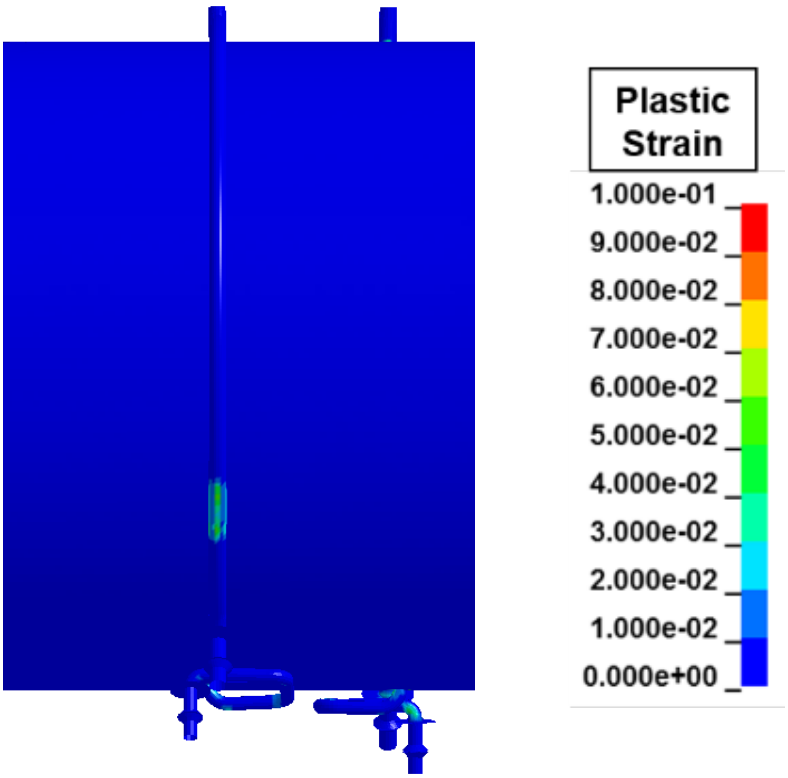

Figure 61. Pipe and fittings damage for the side impact with reinforced protective housing.

4.2.3 Side Impact Protection Enhancement Analysis

The legacy tender model was also modified to investigate preliminary concepts for adding grade crossing impact protection for the tender. A side frame was added to the tender underframe as shown in Figure 62. The side frame is constructed from rectangular section tubing tied to the center sill for lateral strength. The calculated grade crossing impact scenario was again evaluated with this modified tender concept as shown in Figure 63. The analyses demonstrates that additional side impact protection structures can be developed and incorporated into a enhanced tender design.

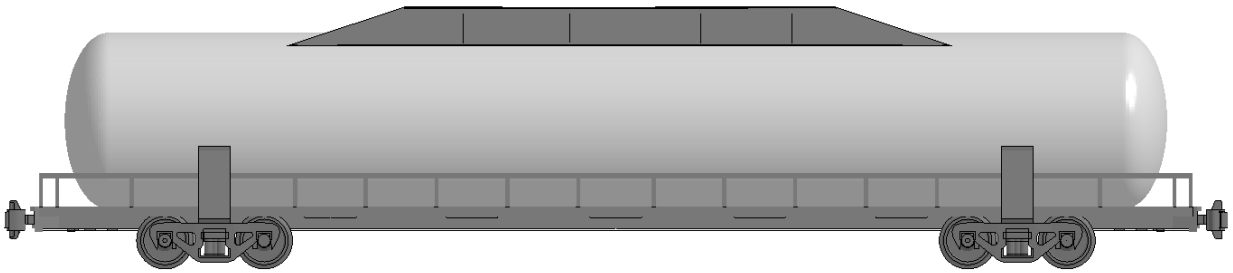

(a) Side view

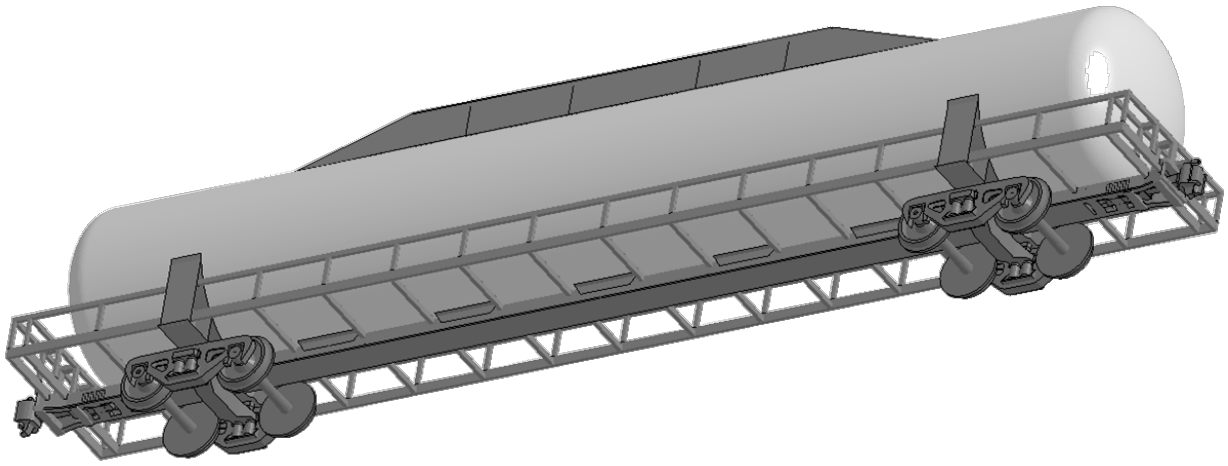

(b) Oblique underframe view

Figure 62. Preliminary side frame concept for grade crossing impact protection.

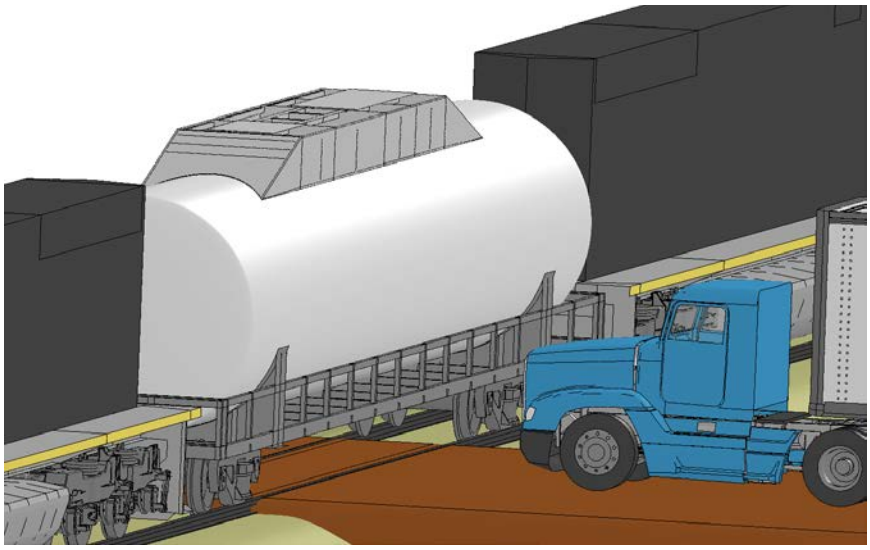

(a) Impact configuration

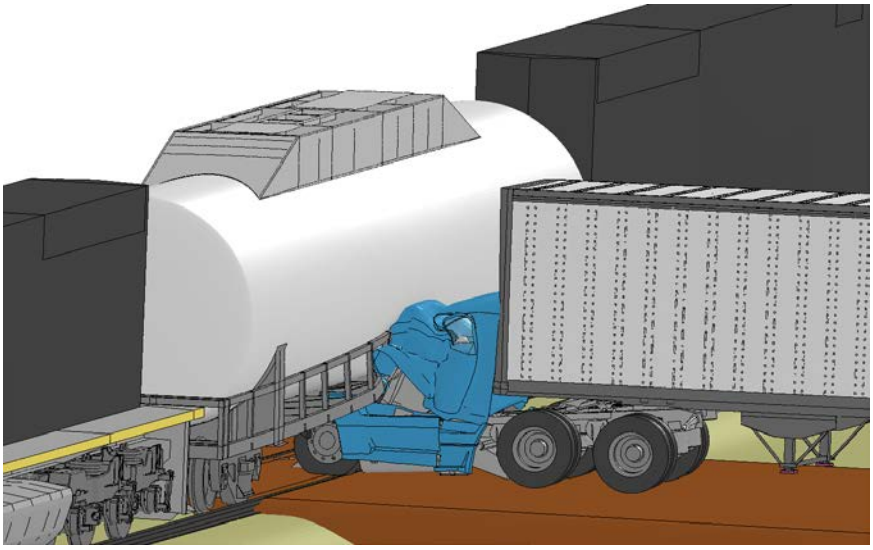

(b) Calculated impact response

Figure 63. Analysis of the side frame concept for the grade crossing impact.

4.2.4 Alternate Load Case – Grade Crossing

In addition to evaluating the tender performance in the grade crossing collision scenario, there was an effort to develop an alternative prescriptive loading condition that can be used to provide side impact protection in a tender specification. As an alternative prescriptive loading condition of the grade crossing scenario, the following criteria was developed:

> "The protective housing shall withstand, without exceeding the ultimate strength or buckling, a 400,000 lb load distributed over an area of 6 in. high × 48 in. wide, centered at a height 33 in. above the rail."

Originally, the language for this load case was adapted from 49 CFR Appendix D to Part 238 - Requirements for External Fuel Tanks on Tier I Locomotives. It is a similar loading condition as the locomotive fuel tank Load Case 3 – Side Impact in the Appendix D. However, the load magnitude in that case is 200,000 lbs total.

We initially evaluated this loading condition at the 200,000 lb load level for the protective housing on the Legacy Tender Design 1 model. The interpretation of this rule is that the load should start at a height of 30 in. from the top of the rail, as shown in Figure 64. When we apply this to the initial protective housing design for the legacy tender model, this loads the structure at a level above the primary framing of the protective housing, which may be problematic.

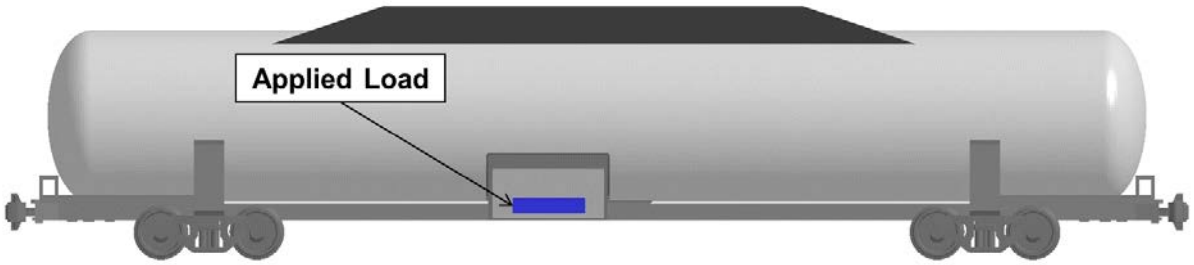

Figure 64. Applied loading area in grade crossing alternate load case.

The results of the 200,000 lb loading in this analysis are shown in Figure 65. Maximum stresses are greater than 80,000 psi, and the maximum deflection after prescriptive load application is 7 inches. While this exceeds the minimum ultimate stress specification for the material, it is likely below the true stress failure level. The plastic strains reach 25%, but the overall structure response is more of a denting or bending behavior than a true buckling response.

In order to mitigate this effect, a reinforced protective housing design was developed using box beam framing. The design of the framing stacked three 2”x2” box beams directly in the load path, as shown in Figure 66. The results of applying the identical prescriptive load to the reinforced protective housing are shown in Figure 67. The protective housing experiences very little deformation and the maximum stresses are well below 70,000 psi, indicating a much better resistance to this load case.

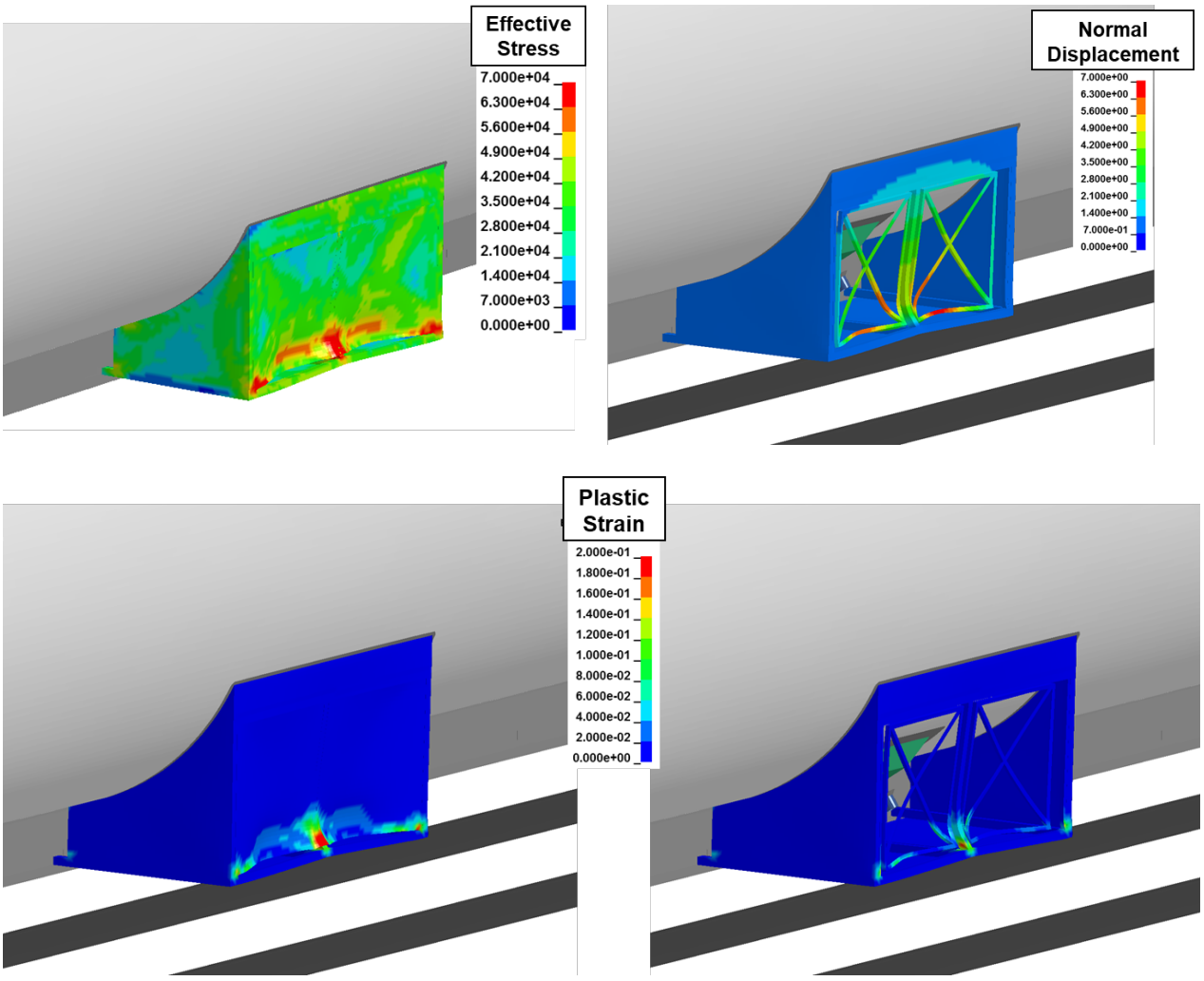

Figure 65. Initial alternate load scenario for grade crossing results.

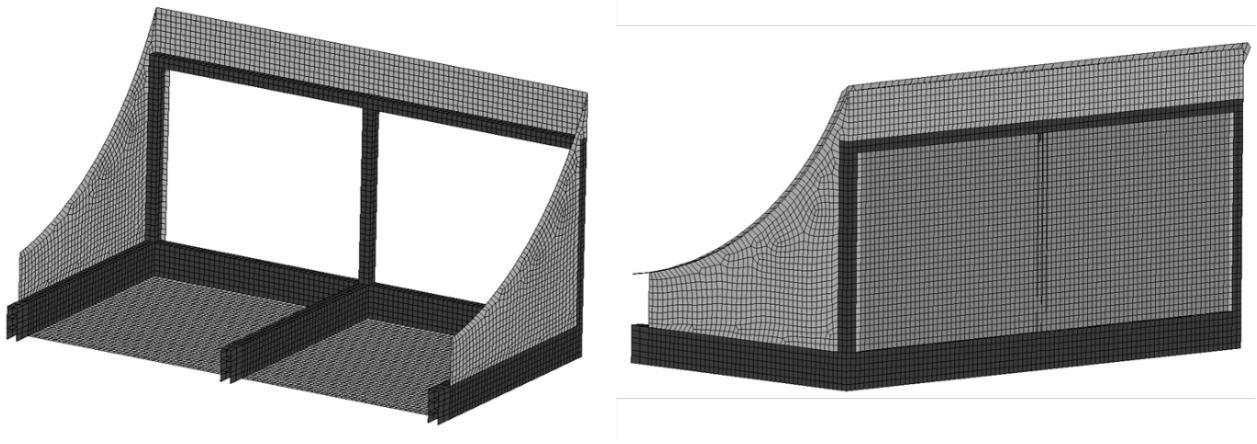

Figure 66. Reinforced protective housing structure.

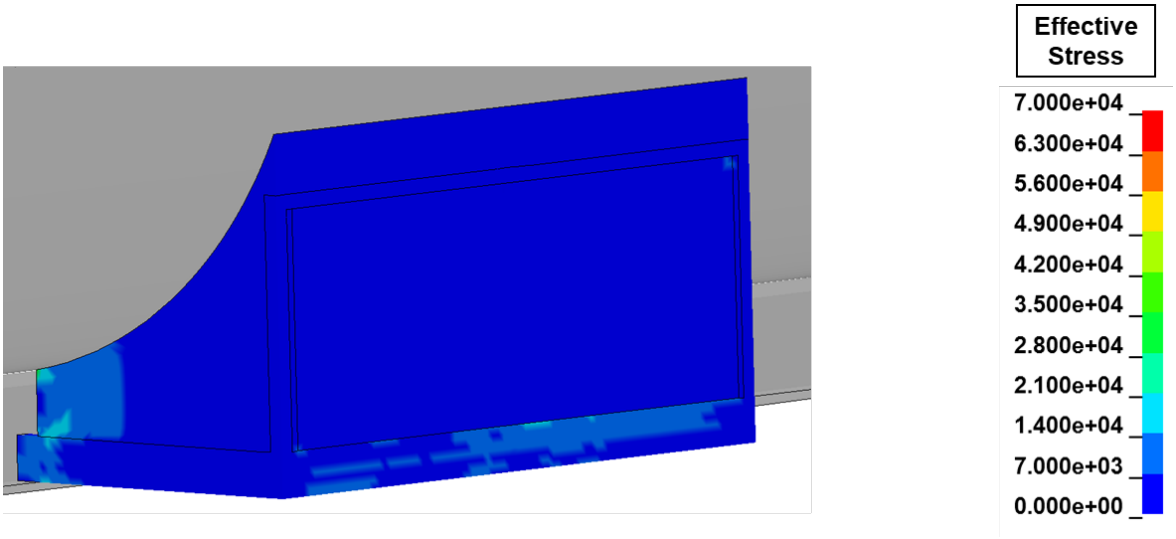

Figure 67. Reinforced protective housing structure results for the 200,000 lb load level.

A comparison to the grade crossing collision scenario determined that the initial 200,000 lbs prescriptive load is much easier to pass and would not provide for a comparable level of protection. The simulation shows that this proposed requirement could probably be met with a protective housing structure design that would not be sufficient to protect in the more detailed collision simulation. Based on a comparison of the analyses, the prescriptive loading condition is less severe than the performance-based grade crossing scenario.

A further evaluation of the appropriate loading for the grade crossing was determined by a simplified analysis of the physics of the collision. The average force required to stop an 80,000 lbs vehicle from 40 mph over a 0.4-second collision duration is 366,000 lbs. Therefore, a final analysis was performed to ensure that the reinforced protective housing could withstand a 400,000 lbs prescriptive load in the same configuration. The results of that analysis are shown in Figure 68 and pass the ultimate stress specification, with a maximum stress of 47,563 psi, well under the 70,000 psi limit.

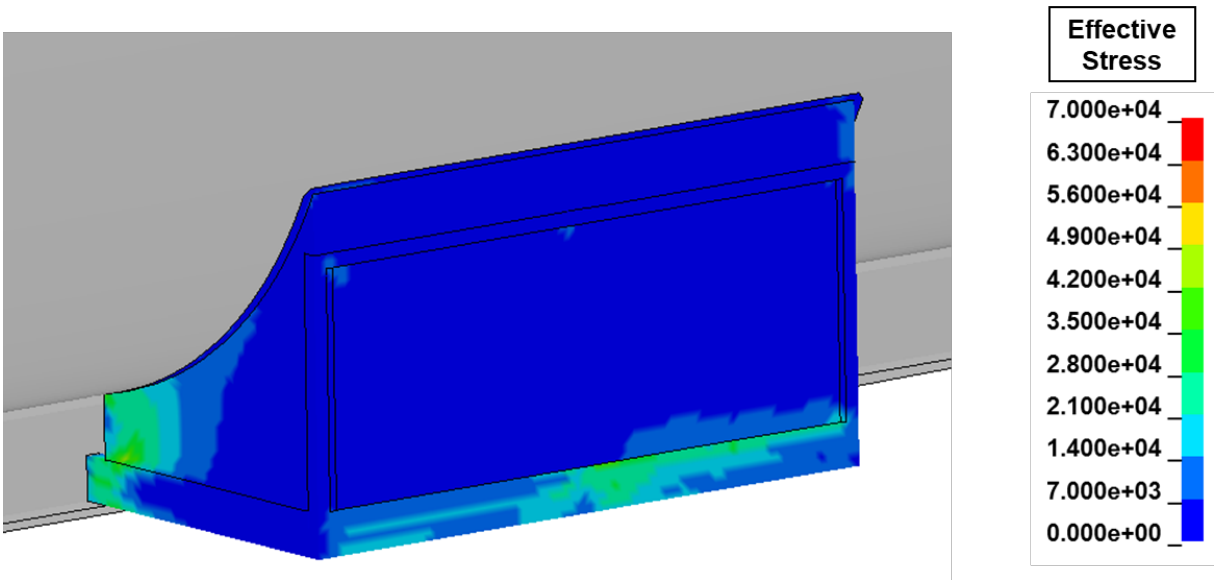

Figure 68. Reinforced protective housing structure results at the 400,000 lb force magnitude.

4.3 LNG Tender Rollover Collision Load Case

The rollover scenario evaluated for the tender is shown in Figure 69. The tender is rolling on a flat rigid surface at a lateral velocity of 9 mph with a corresponding rotational velocity to produce the rolling response. The tender continues to roll until the top fittings jacket skid protection impact against the ground. The combination of the rolling velocity and gravitational loads control the impact severity.

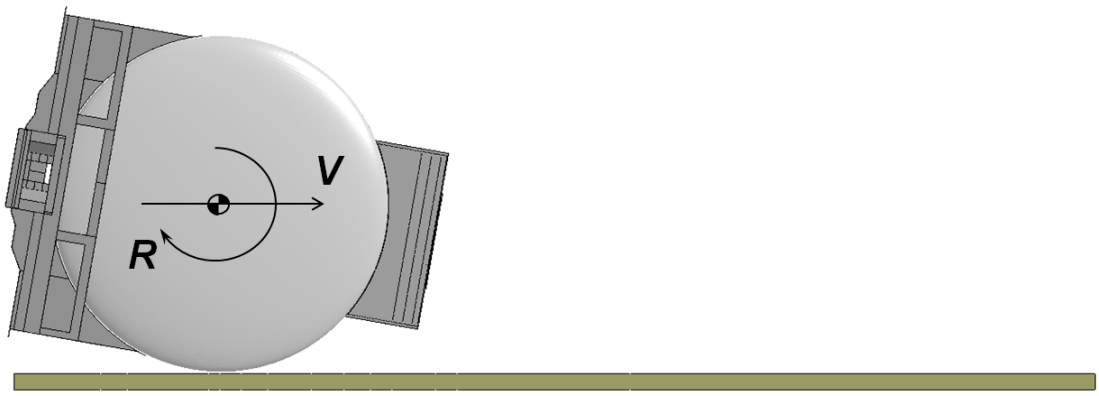

Figure 69. Tractor-trailer rollover collision scenario.

The legacy tender design 1 top fittings jacket skid protection was analyzed to assess protection for this load case. The calculated impact damage for the rollover scenario on the top fittings protective structures are shown in Figure 70. The plastic strain levels are small and localized to the hard point connection points on the structure. The impact displacements are small and would not be expected to impinge on any of the enclosed equipment. This example demonstrates that a

suitable protective structure can be incorporated in a tender design that will protect against this collision scenario.

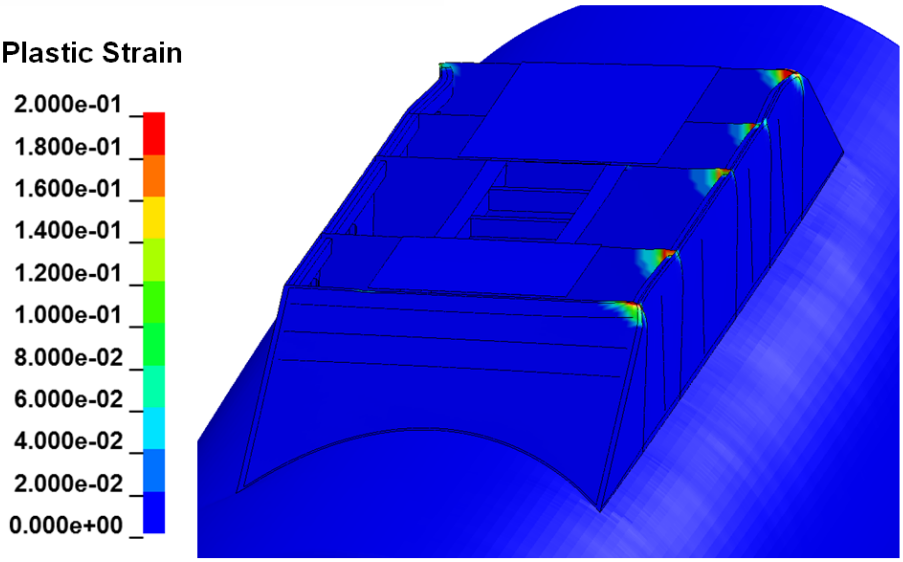

Figure 70. Calculated rollover scenario damage to the top fittings protective structures.

4.3.1 Alternate Load Case – Tender Rollover

As an alternative evaluation of the grade crossing scenario, the following criteria have been developed:

> The top jacket skid protection shall withstand, without buckling or material failure, the following compressive loads equal to 100% of tender GRL, applied separately:
>
> - Vertical load applied along any 48 in. length of longitudinal edge, or the full longitudinal length of the protective structure, whichever is less. This load can be distributed on the top edge (up to a 2 in. wide strip) of the protective structure. Edges of the 3:1 slope portions of the skid are excluded.
>
> - Longitudinal load applied the full width of the protective structure. This load can be distributed over a 2 in. strip at the top edge of the protective structure's 3:1 slope.
>
> - Lateral load applied along any 48 in. length of longitudinal edge, or the full longitudinal length of the protective structure, whichever is less. This load can be distributed along the top edge (up to a 2 in. high strip) of the protective structure. Edges of the 3:1 slope portions of the skid are excluded.

These prescriptive loading conditions are shown in Figure 71.

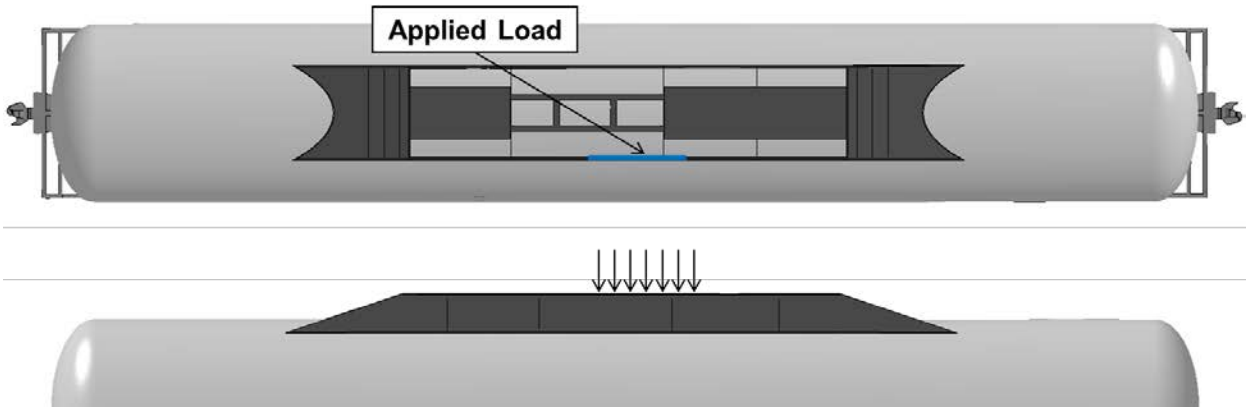

(a) Vertical load

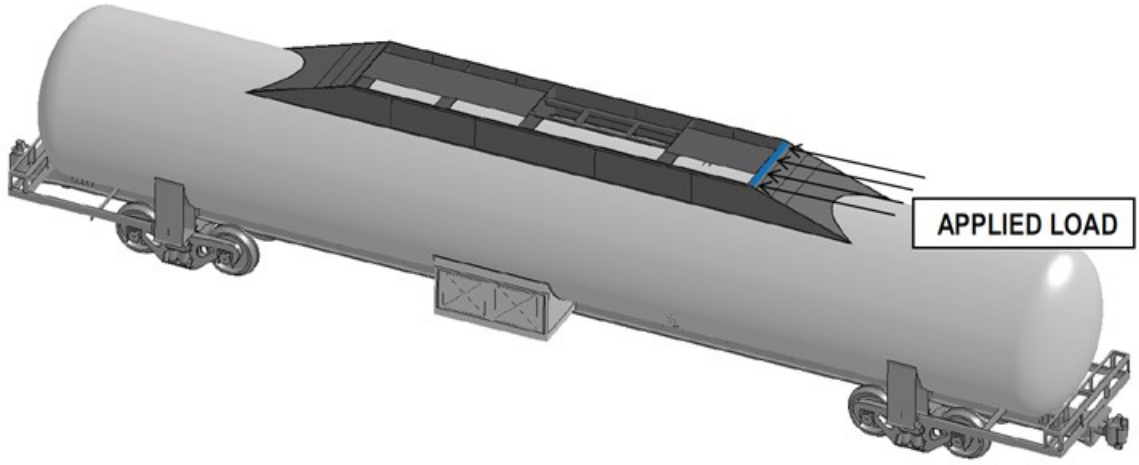

(a) Longitudinal load

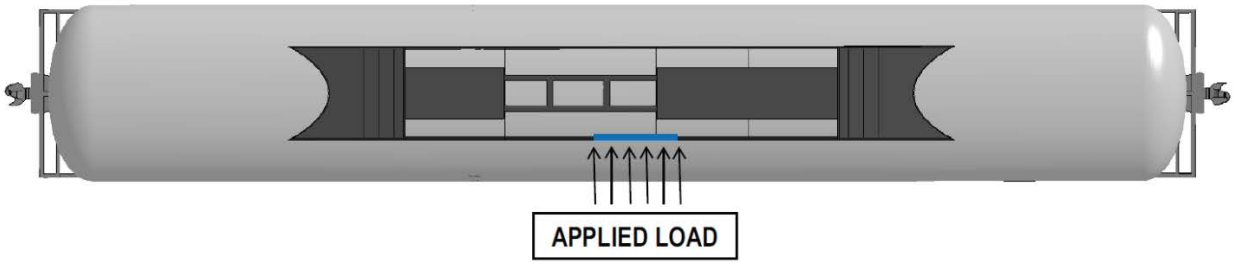

(a) Lateral load

Figure 71. Applied loading area in proposed rollover alternate load case.

Analyzing the vertical load case first, the maximum stresses slightly exceed 70,000 psi, causing some concern. While the plastic strains remained below 12% locally, the bending response of the top fittings was unacceptable. These results are shown graphically in Figure 72. To mitigate the incompatibility between the prescriptive loading condition and the top fittings design, the roof structure was redesigned by increasing the box beam framing dimensions to 4”x4”, adding

additional supports, and decreasing the distance between the bulkheads to 48 in., as shown in Figure 73.

Figure 74 shows the results of the proposed loading scenarios with the new roof design. In all cases, the maximum stresses do not exceed 70,000 psi, and there is minimal strain and deformation, indicating the roof structure would be able to protect the top fittings in a rollover.

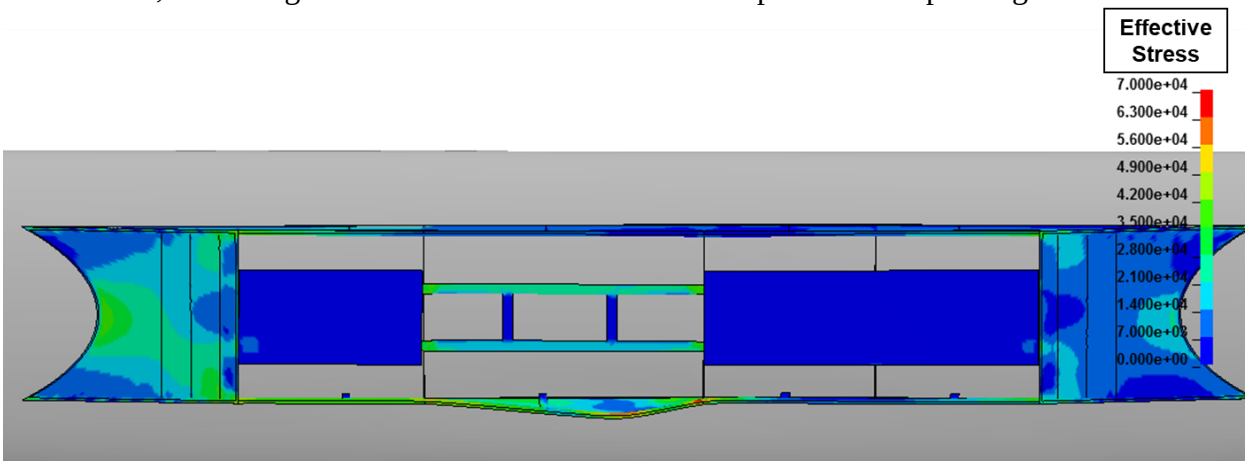

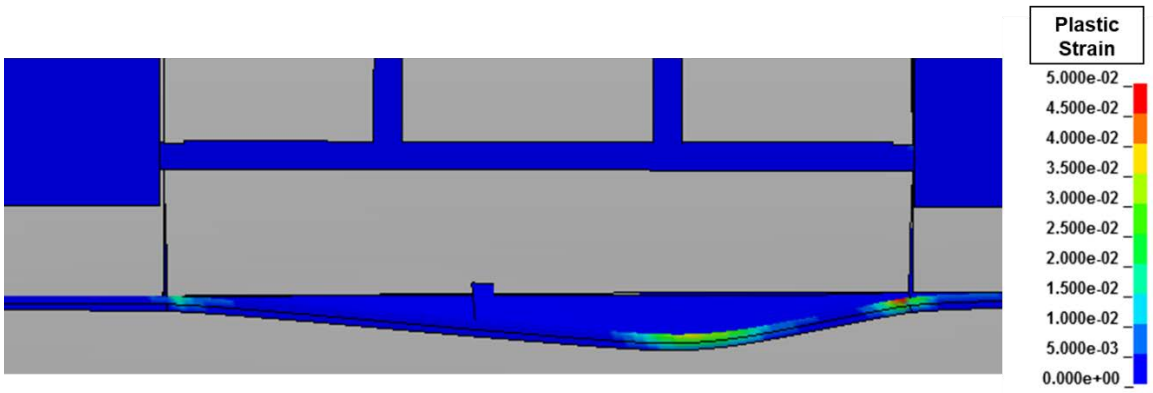

Figure 72. Initial proposed alternate load scenario for rollover results (vertical).

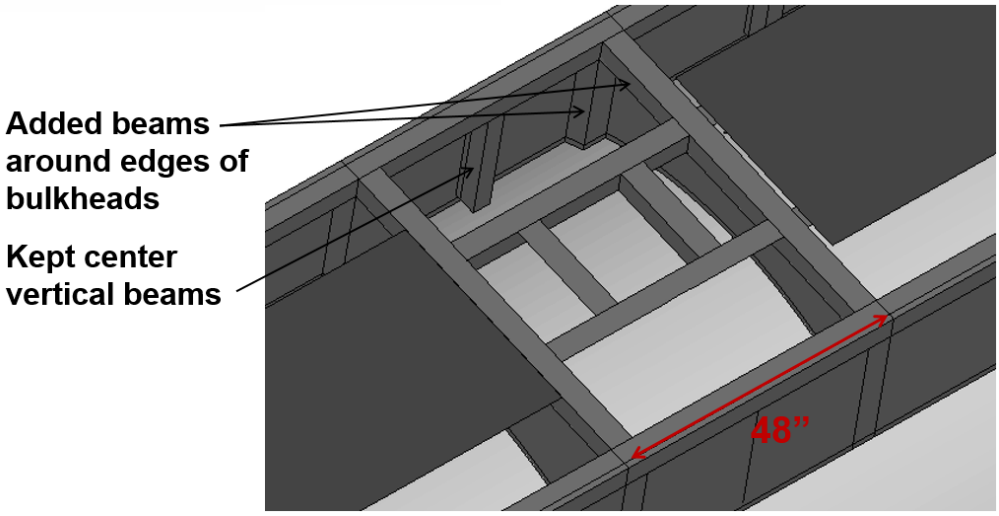

Figure 73. Roof structure redesign.

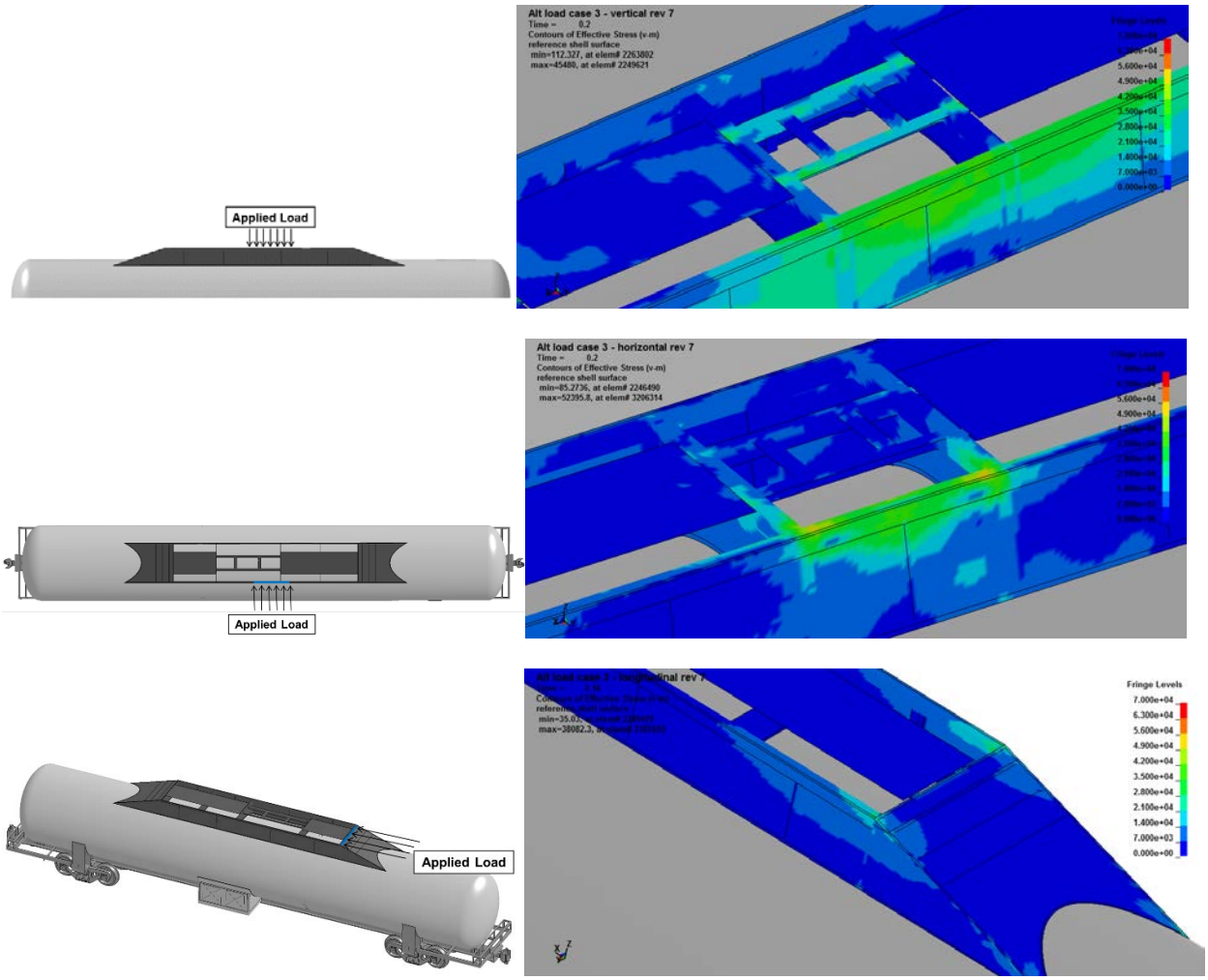

Figure 74. Roof redesign structure results (vertical, top; horizontal, middle; longitudinal, bottom).

4.4 Side impact Puncture Analyses

There are a variety of tank impact scenarios that can occur in either derailments or uncontrolled sideswipe conditions. The side and head impact conditions analyzed here are designed to protect against these collisions. This is similar to the approach used to analyze impact behaviors and puncture resistance of tank cars [3, 4]. The primary emphasis of these analyses is to prevent a puncture of the LNG tank.

The side impact condition included in the specification is:

> The fuel tank of the tender shall be placed with its side next to a rigid fixed barrier, 25 ft. wide and 18 ft. high. The impactor shall be 12 in. × 12 in. with edges rounded 1 inch. The impactor shall be mounted to a rail car weighing at least 286,000 lb.
>
> The fuel tank of the tender shall be impacted on the horizontal centerline and at the vertical centerline between body bolsters. However, if there is a side protective housing centered on the fuel tank, then the impact target shall be centered between the body bolster and side protective housing. In the case where the impact target includes a circumferential weld on the jacket, the target shall be moved 24 in. to the side of the initial target having the least distance from the weld to the edge. The speed at impact shall be 25 mph.

The required result for the side impact is:

> The tender jacket must not be punctured, and the inner tank must not be breached. The only fuel release allowed is through the automatic opening and reclosing of the pressure-relief valve(s), resulting from pressure changes due to inner tank deformation or liquid surge, and from piping external to the jacket.

In this section, analyses are performed to assess the side impact performance of the legacy tender tanks under side impacts of various severity and to investigate enhancements that can be made to the tender tanks to improve side impact puncture protection.

4.4.1 Baseline Side Impact Puncture Analyses

The baseline puncture analyses were performed using the legacy tender tank dimensions and thicknesses. The nominal dimensions for the tender included 0.5-inch thicknesses for the jacket and inner tank with an approximately 10-foot jacket diameter and 6-inch annular space between the jacket and inner tank. The primary impactor used for these impact analyses is a rigid 286,000 impactor with a 12 by 12-inch impact face with a 1-inch radius around the edges. The tank is backed up by a 25-foot wide rigid wall. This configuration has been previously used and validated for tank car puncture modeling [3, 4].

The calculated impact response for a 25 mph impact is shown in Figure 75. The impact is sufficiently severe in this case to puncture the jacket. The fringes shown are a normalized material damage parameter and failure occurs at a damage value of 1.0 (as described in Section 2.1.1). The calculated damage to the inner tank is shown in Figure 76. The calculated damage has a maximum value of 0.53 at the corners of the impactor.

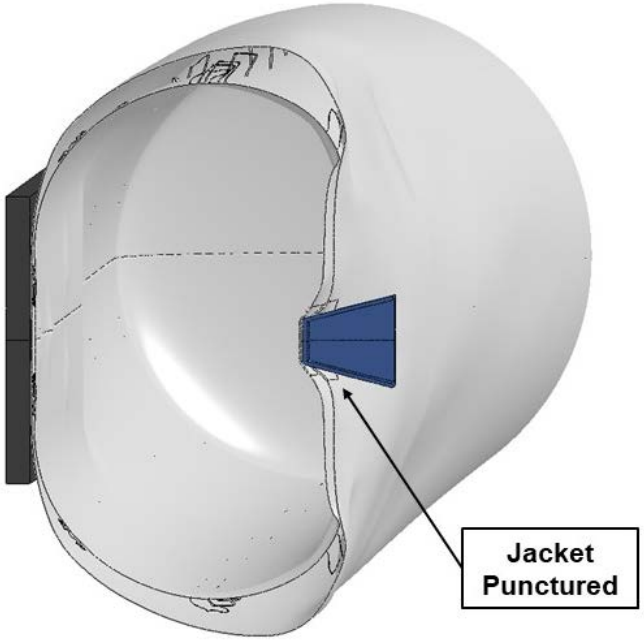

Figure 75. Calculated 25 mph impact behavior with a 12x12-inch impactor.

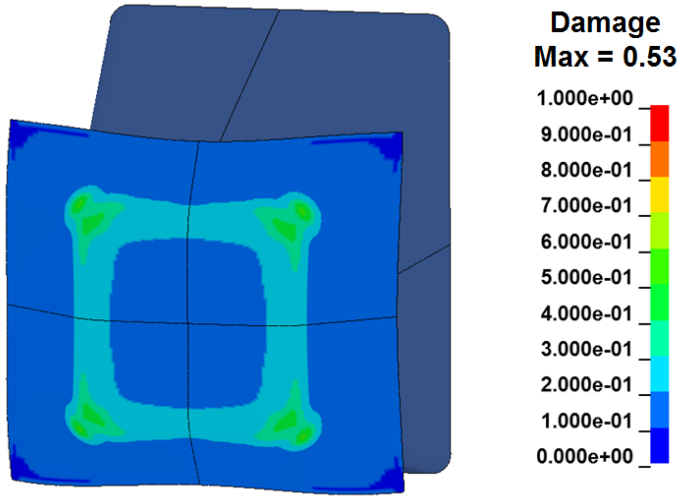

Figure 76. Calculated damage for the 25 mph side impact.

The calculated force deflection histories for 20, 25, and 30 mph side impacts are shown in Figure 77. In these initial analyses, the inner tank was pressurized to 150 psi and the outage volume was set at 4%. A control volume algorithm is used in the inner tank to calculate the change in

volume and corresponding pressure change as the tank is deformed. These calculated tank pressure histories are plotted against the tank indentation in Figure 78. During the initial loading, the behaviors are similar with the exception of a small increase in force at higher impact velocities because of inertial load contributions. At 20 mph, the jacket is not punctured. For both the 25 and 30 mph impacts, the jacket is punctured as the impact force exceeds approximately 2 million lbs.

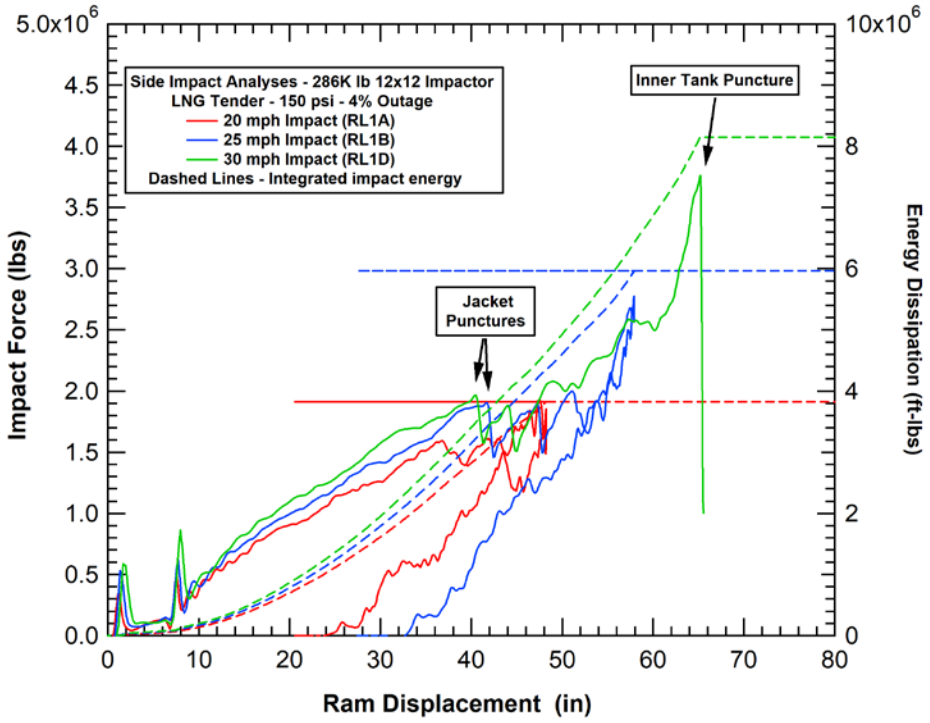

Figure 77. Calculated force-deflection histories for side impacts at various impact velocities.

After the jacket failure, the impact forces continue to rise with increasing rates. This is caused by rapidly increasing tank pressures as the tank approaches a shell full condition. At 25 mph, the calculated maximum calculated pressure in the tank was 352 psi and at 30 mph, it reached 449 psi. These values are well in excess of a rupture disk pressure that would be used in this tank design (250-psi limit).

The most efficient approach to mitigate these peak pressure levels in side impacts is to increase the outage volume. The calculated impact force and pressure histories for 25 mph impacts with 4%, 8%, and 12% outage volumes are shown in Figure 79 and Figure 80. The peak pressure reduces from 352 psi to 252 psi and 216 psi as the outage volume of 4% is increased to 8% and 12%, respectively.

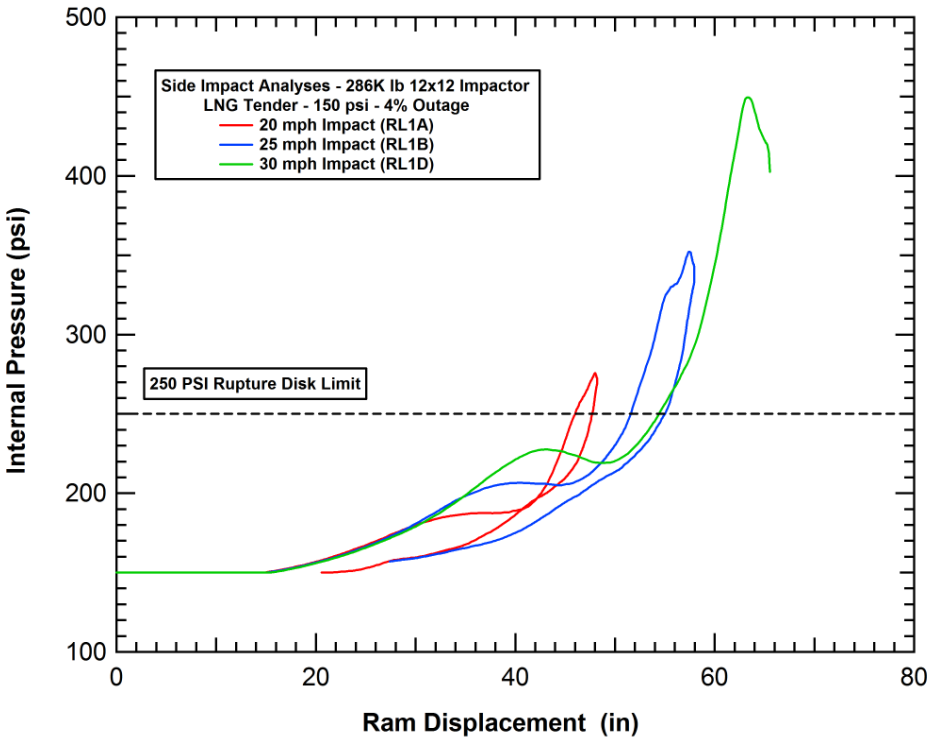

Figure 78. Calculated inner tank pressure curves for side impacts at various impact velocities.

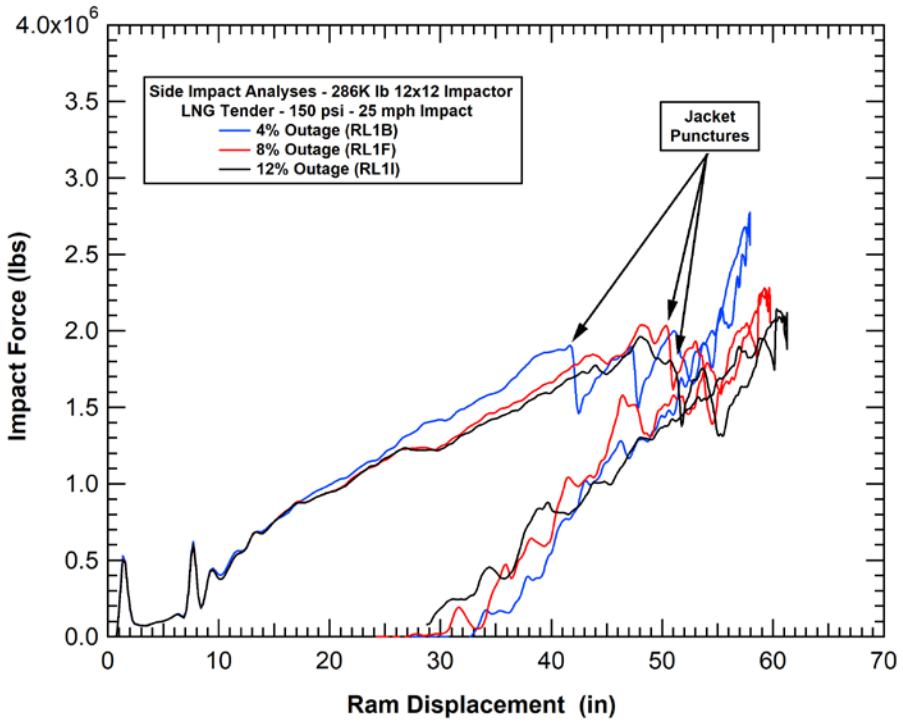

Figure 79. Calculated force-deflection histories for 25 mph impacts and various outage volumes.

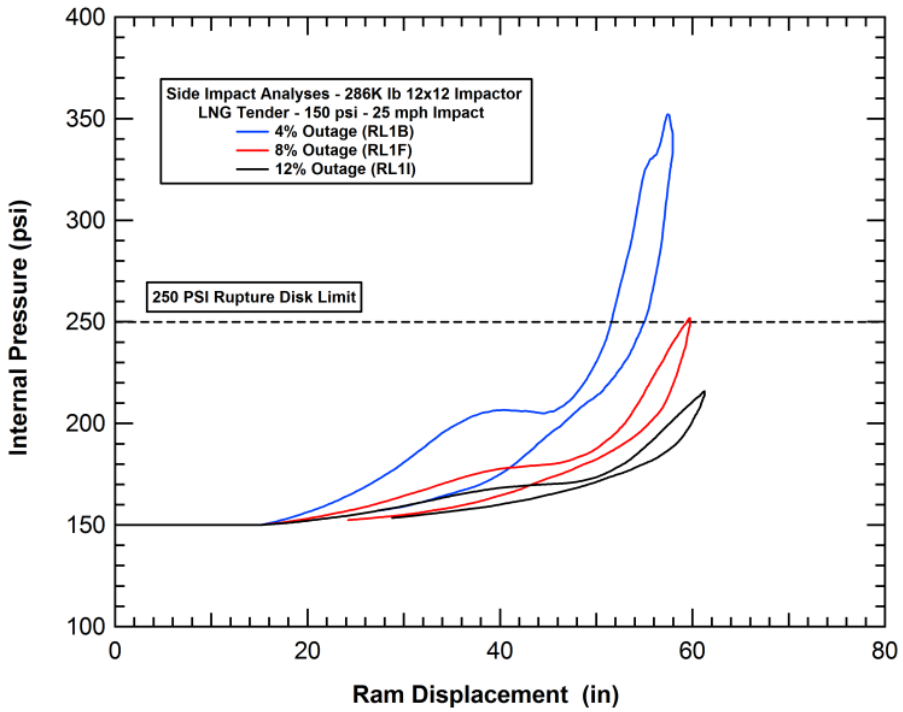

Figure 80. Calculated inner tank pressure curves for 25 mph impacts and various outage volumes.

A summary of the calculated peak pressures in the inner tank as a function of impact velocity and outage volume percentage are summarized in Figure 81. The curves fit through the calculated values can provide guidance in selecting requirements on impact conditions and tank outage restrictions to prevent a release resulting from a rupture disk failure. A corresponding summary of the peak pressures calculated for the various impact conditions are provided in Table 2.

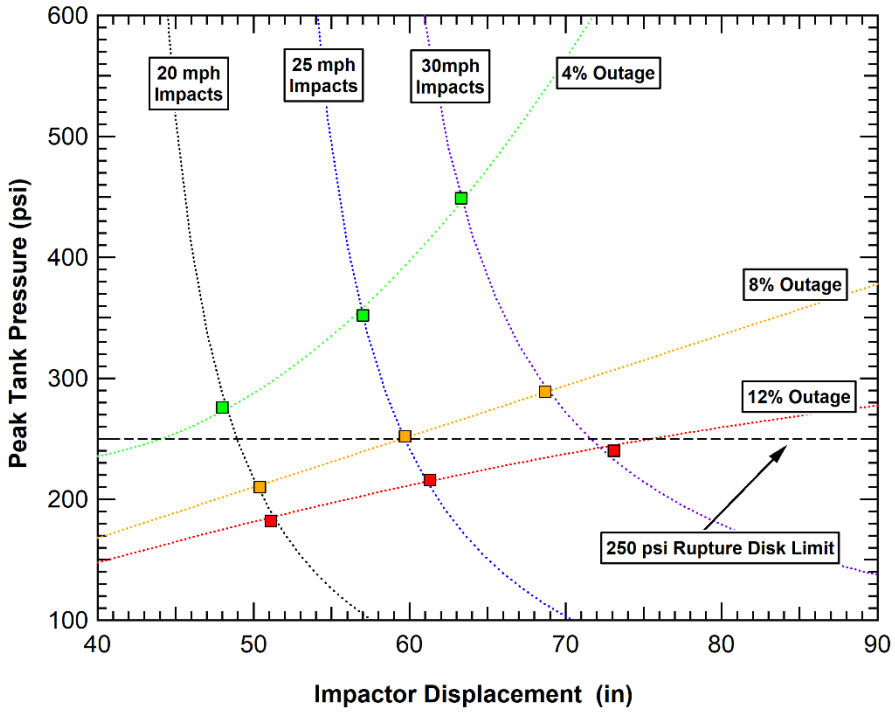

Figure 81. Calculated tank peak impact pressure as a function of impact velocity and outage volume.

Table 2. Calculated Peak pressure values for the 150 psi tender tank

Impact Speed	4% outage	8% outage	12% outage
20 MPH	276 psi at 48.0 inches displacement	210 psi at 50.4 inches displacement	182 psi at 51.1 inches displacement
25 MPH	352 psi at 57.5 inches displacement	252 psi at 59.7 inches displacement	216 psi at 61.3 inches displacement
30 MPH	449 psi at 63.3 inches displacement	289 psi at 68.7 inches displacement	240 psi at 73.0 inches displacement

A further summary of the damage produced in the various impact conditions is summarized in Table 3. The three damage mechanisms evaluated are a rupture disk release caused by an overpressure during the impact load, a loss of vacuum caused by a breach in the jacket, and a puncture of the inner LNG tank. Green indicates that it is expected to survive the loading condition for the specific damage mode. Red indicates that it will not survive the loading for the specific damage mode. Yellow indicates that it is close to the threshold for the specific damage mode.

Table 3. Calculated damage to the tender as a function of impact speed and outage.

Impact Speed	Failure Mode	4% outage	8% outage	12% outage
20 MPH	Rupture Disk Failure			
	Jacket Puncture (Vacuum Loss)			
	Inner Tank Puncture			
25 MPH	Rupture Disk Failure			
	Jacket Puncture (Vacuum Loss)			
	Inner Tank Puncture			
30 MPH	Rupture Disk Failure			
	Jacket Puncture (Vacuum Loss)			
	Inner Tank Puncture			

4.4.2 Enhanced Side Impact Puncture Protection

Additional side impact analyses were performed to evaluate concepts to enhance the side impact puncture performance. Based on the tender design constraints and past research on tank car puncture performance [3, 4], the most effective method for improving puncture resistance is to increase the thickness of the jacket or inner tank. Since the jacket fails at lower impact severities and puncture of the jacket leads to an undesirable loss of vacuum, the emphasis was placed on increasing the jacket thickness. These evaluations could also inform the development of a prescriptive thickness requirement that can be included in the specification.

The comparisons in this section compare the baseline tender tank with a 0.50-inch-thick jacket wall with modifications that increase the thickness by both 1/8-inch and 1/4-inch. The calculated force-deflection characteristics for the three different tender tank designs impacted at 25 mph are compared in Figure 82. The corresponding comparisons of the tank internal pressure during the impact and the calculated damage to the jacket wall are compared in Figure 83 and Figure 84, respectively. The added thickness has very little effect on the calculated force-deflection behavior and the calculate rise in internal pressure from the impact. Both of these response characteristics are dominated by the inner tank with the added stiffness of the internal pressure.

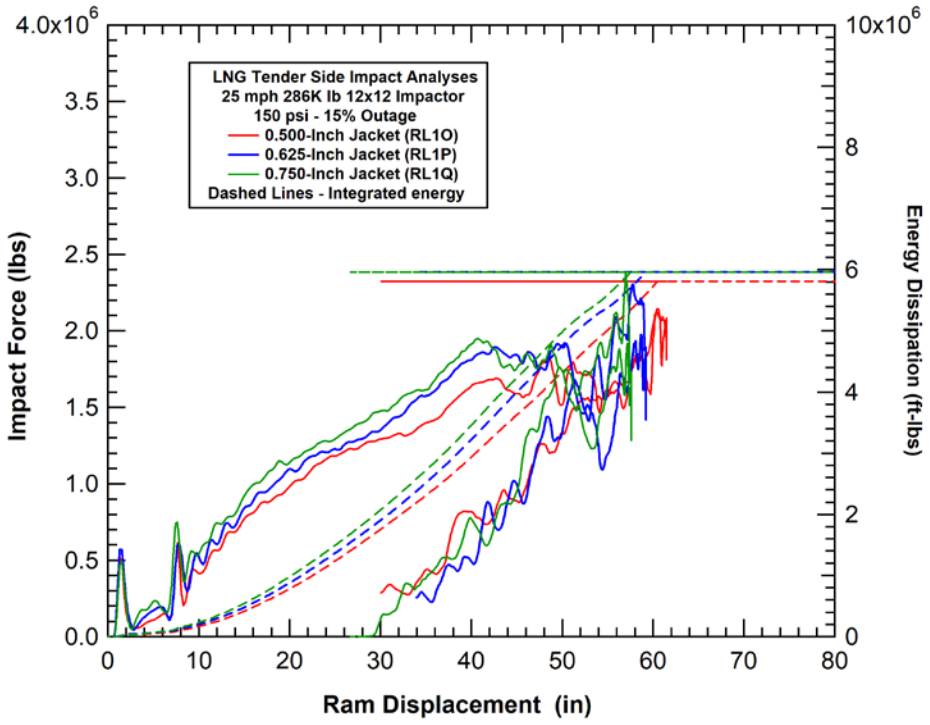

Figure 82. Calculated force-deflection histories for 25 mph impacts and various jacket thicknesses.

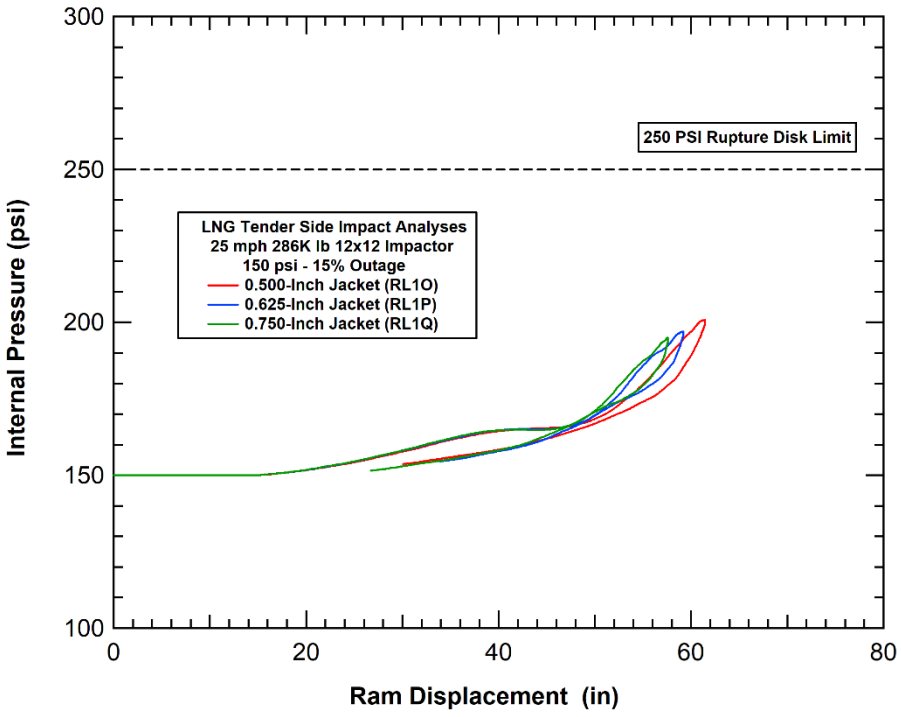

Figure 83. Calculated inner tank pressure curves for 25 mph impacts and various jacket thicknesses.

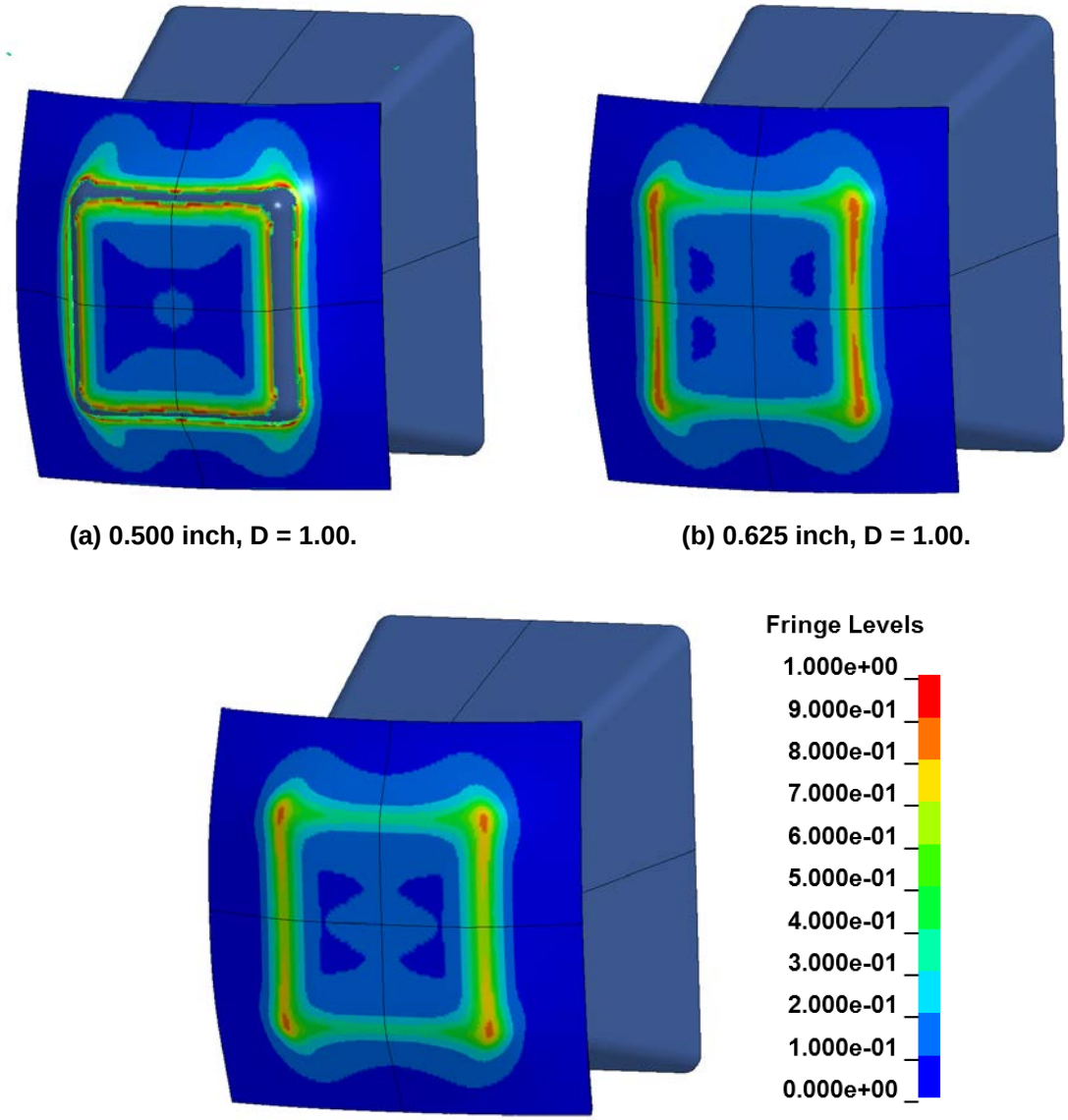

(a) 0.500 inch, D = 1.00. **(b) 0.625 inch, D = 1.00.**

(c) 0.750 inch, D = 0.86.

Figure 84. Calculated jacket damage for 25 mph impacts and various jacket thicknesses.

The comparison of the damage to the jacket, shown in Figure 84, indicates that the increase in the thickness of the jacket has a significant effect on the potential for a jacket rupture. Analyses indicated that the jacket would not be punctured in a configuration of a 0.50-in-thick 304L SS inner tank and a 0.625-in-thick TC128B jacket. The 0.750-in-thick jacket provides increased safety margin.

4.5 Head impact Puncture Analyses

Similar calculations were performed to evaluate the head impact behaviors. The head impact condition included in the specification is:

> The tender shall be stationary and free-standing on tangent rail, with an assumed wheel/rail coefficient of friction of 0.15. Assume tender brakes are set and wheels will slide, not roll. The impactor shall be 12 in. × 12 in. with edges rounded 1 inch. The impactor shall be mounted to a rail car weighing at least 286,000 lb. The fuel tank of the tender shall be impacted on the vertical centerline 21 in. above the bottom of the inner tank. The speed at impact shall be 35 mph.

The required result for the head impact is:

> The tender jacket must not be punctured, and the inner tank must not be breached. The only fuel release allowed is through the automatic opening and reclosing of the pressure-relief valve(s), resulting from pressure changes due to inner tank deformation or liquid surge, and from piping external to the jacket.

In this section, analyses are performed to assess the head impact performance of the legacy tenders under head impacts of various severity and to investigate enhancements that can be made to the tender fuel tanks to improve head impact puncture protection.

4.5.1 Baseline Head Impact Puncture Analyses

In the baseline head impact analyses, the legacy tender jacket and inner tank head configuration was used to assess the head impact performance. In the preliminary analyses, a simplified impact configuration was applied where the head is rigidly constrained longitudinally against the impactor. Subsequently, additional analyses were applied to assess the effect of a lower tank constraint for the impact conditions in the tender specification.

The fully constrained head impact condition was previously used to test and analyze head impact performance of various designs in the NGRTC research program [3]. An example of a test with a chlorine tank car head geometry from the NGRTC program is shown in Figure 85. In this test, the impact was offset from the center of the head and the impactor was a 6x6-inch impactor with a 0.5-inch radius around the edges. The corresponding calculated response for this test is shown in Figure 86 and the force-deflection behaviors from the test and simulation are compared in Figure 87. The good agreement on the damage modes, puncture of the jacket, and the quantitative agreement on the impact forces all were used in the validation of the simulation methodologies that are being applied in this program.

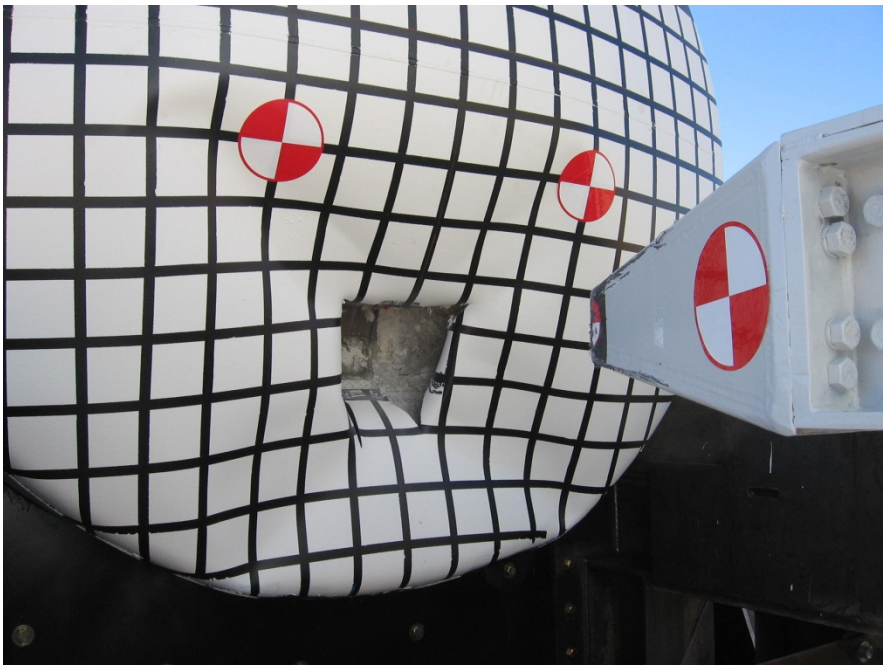

(a) Post impact configuration

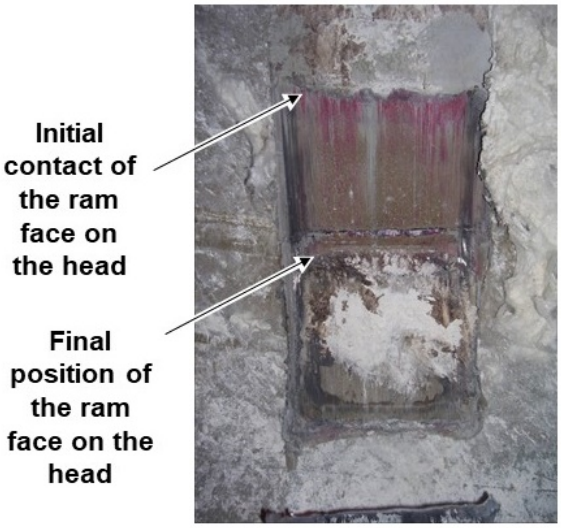

(b) External damage to the tank head

Figure 85. Example head impact test configuration used in the NGRTC Program [3].

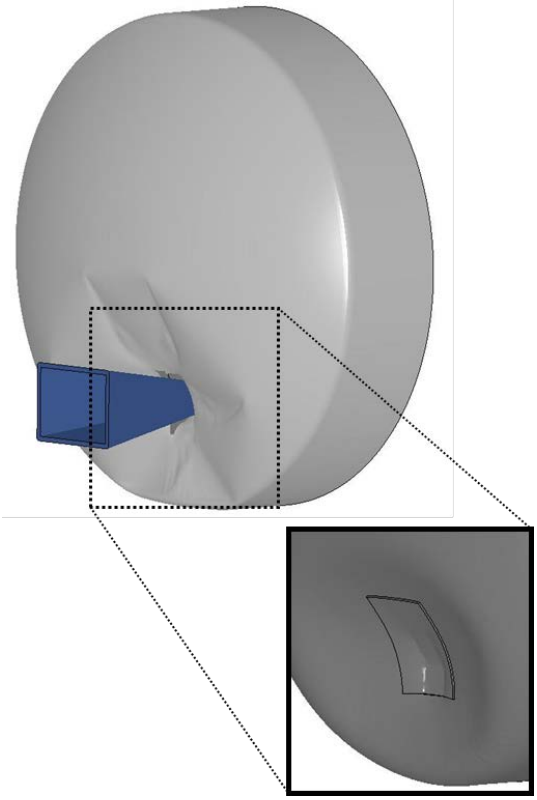

Figure 86. Calculated jacket head puncture and inner tank head damage for the head impact test conditions.

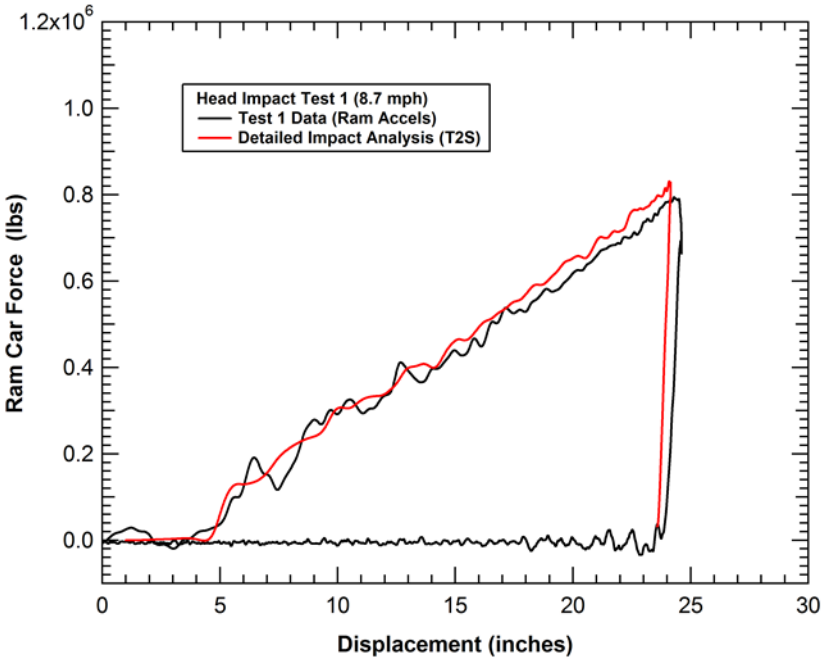

Figure 87. Comparison of the measured and calculated force-displacement behaviors for the head impact test conditions.

An example of a preliminary tender tank head impact analyses at 30 mph is shown in Figure 88. The corresponding calculated damage to the inner tank head is shown in Figure 89. The analysis shows that the legacy tender design tank head can withstand a significant impact and large deformations without puncturing the inner tank head. However, the puncture of the jacket head would result in a loss of vacuum and reduce the insulating capacity of the tender design.

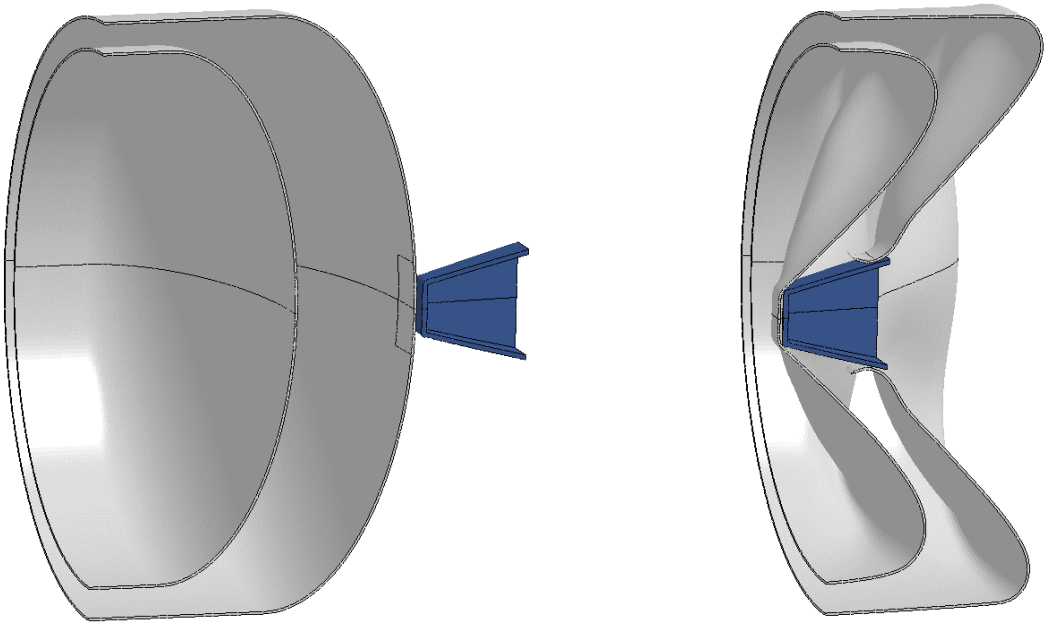

(a) At impact. **(b) Impact deformations.**

Figure 88. Calculated behavior for a 30 mph center impact on constrained tank head.

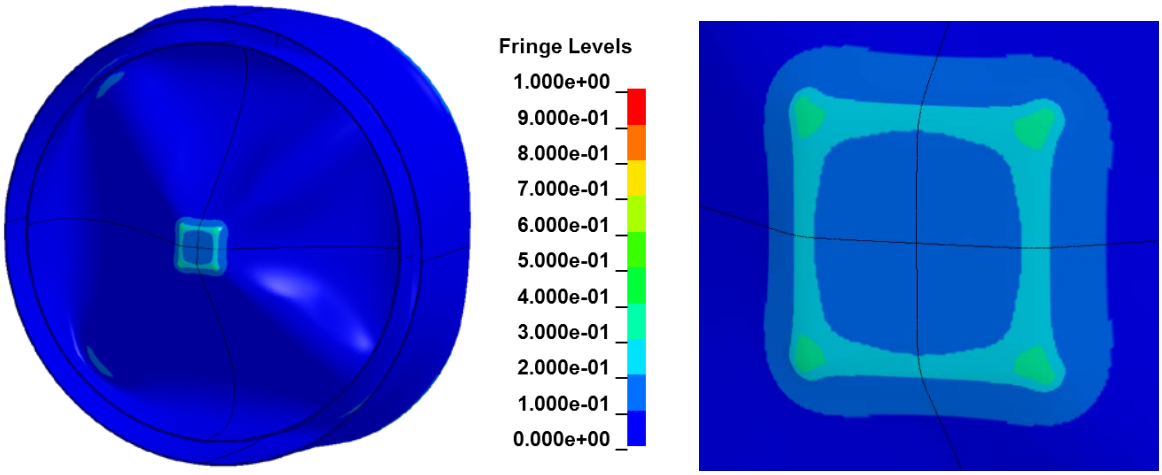

(a) Overall deformation. **(b) Impact region damage.**

Figure 89. Calculated inner tank head damage for a 30 mph center head impact.

The calculated force deflection behaviors for centered head impacts at 25, 30, and 35 mph are compared in Figure 90. The heads in these simulations were fully constrained and pressurized to 150 psi (constant pressure). The jacket head is punctured when the impact force exceeds approximately 2.6 million lbs and the inner tank head is not punctured at these impact velocities (up to 35 mph). The three analyses all follow the same force-deflection curve. The higher speed collisions allow for a further deflection and indentation of the inner tank head with associated higher levels of damage to the head in the impact zone. The results of these analyses were used to provide guidance on tank designs and operational requirements in the specification.

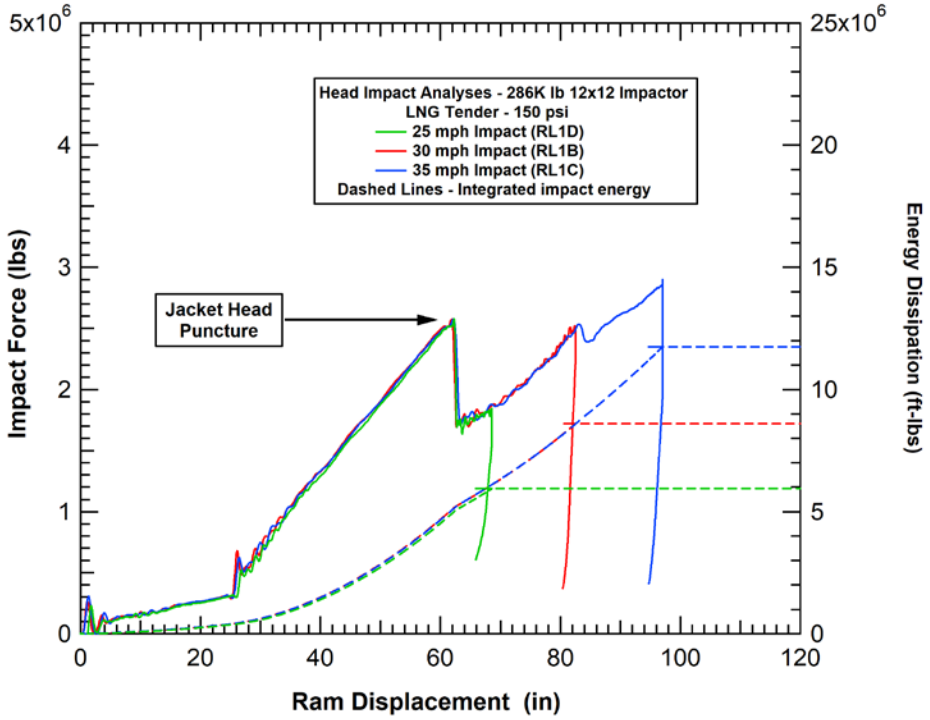

Figure 90. Calculated behaviors for different speed impacts on a constrained tank head.

The simplification of using a constant internal pressure was investigated and found to be reasonable for head impact conditions. An additional analysis was performed to confirm the effect of constant vs variable internal pressure were small. The variable pressure analysis used a full tank with the airbag algorithm to model a 15% outage volume. The calculated force deflection characteristics with the constant and variable internal pressure models are compared in Figure 91. The effect of the methodology for modeling the internal pressure is small and has negligible influence on the jacket head puncture response. With the variable pressure model, the pressure magnitude has increased from 150 psi to approximately 170 psi at the time of the jacket puncture and reaches a 208 psi maximum pressure. However, the stiffness provided by the domed head geometry and baseline pressure level in the impact response are much greater than the effects of the incremental pressure increase.

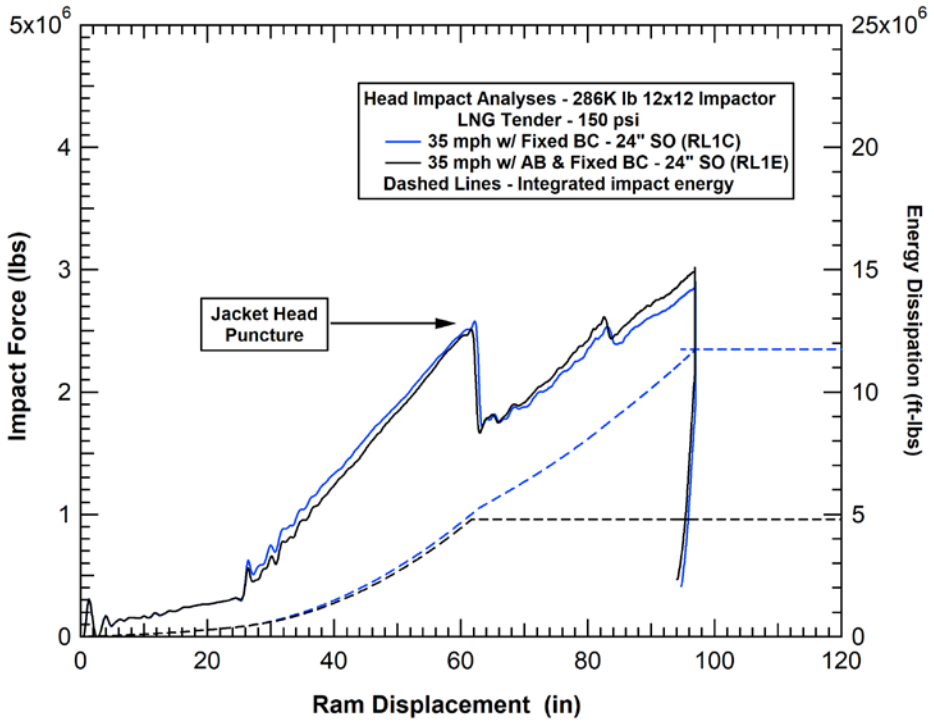

Figure 91. Effects of tank internal pressure modeling for impacts on constrained tank heads.

Another impact parameter that was investigated in the analyses was the effect of an offset versus a center head impact. The comparison of the calculated impact deformations are shown in Figure 92 and the comparison of the calculated force-deflection characteristics are shown in Figure 93. The offset impact produces a small increase in the initial stiffness of the force deflection behavior due to the proximity to the edge of the tank head. The more significant effect is a significant reduction in the tank head puncture force. This reduction in the tank head puncture force results from a nonuniform loading around the perimeter of the impactor face and more concentrated loading at specific corners of the impactor where the puncture initiates.

Another effect that was investigated in the baseline analyses was the effect of the standoff distance between the jacket and inner tank heads. The legacy tender designs had a larger standoff distance between the heads than is typical for tank car designs. To investigate if this additional standoff distance is beneficial, two analyses were performed that compared the baseline 24-inch head standoff distance to a reduced 6-inch standoff distance. The calculated force deflection behaviors of the 24-inch and 6-inch jacket head standoff distances are compared in Figure 94. The larger standoff distance produces primarily an 18-inch shift in deflection before the significant forces develop in the impact. However, the standoff distance is found to have a relatively small effect on jacket head response and puncture force/energy beyond the initial shift in the force-deflection curves.

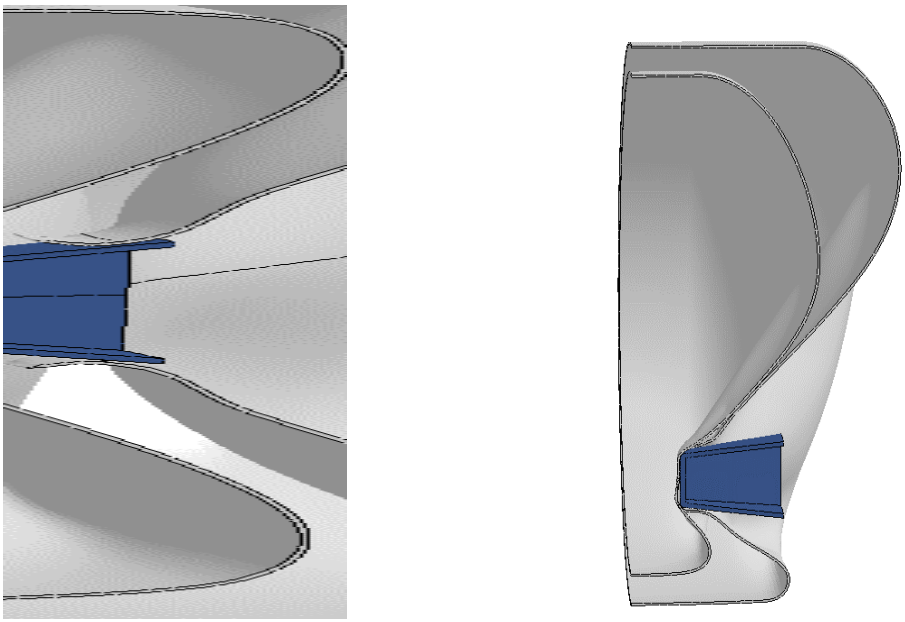

(a) Center impact. (b) Offset impact.

Figure 92. Calculated behavior for a 30 mph center impact on constrained tank head.

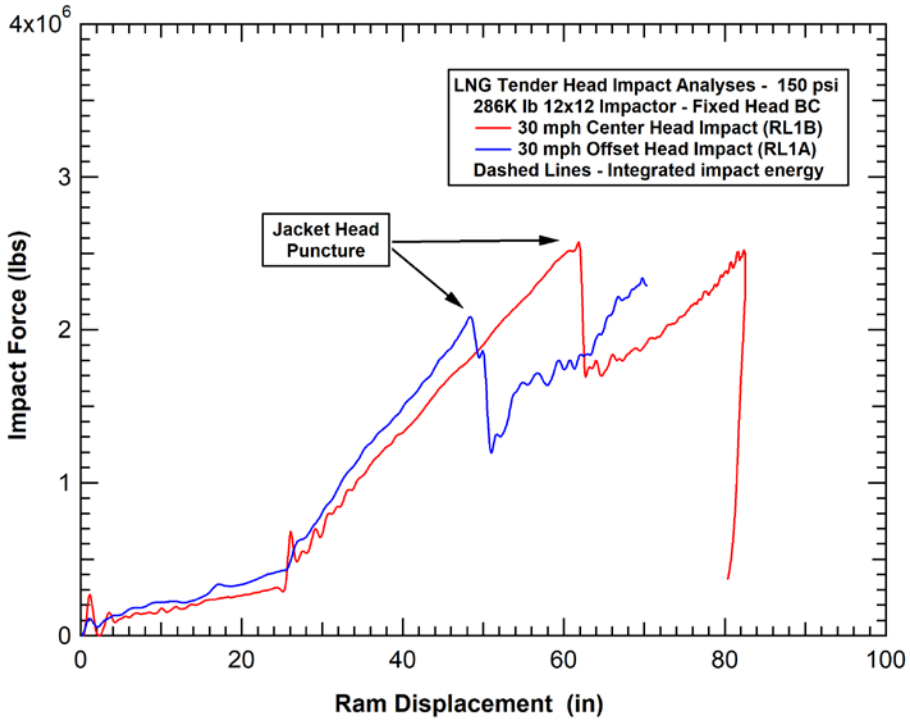

Figure 93. Calculated force-displacement behaviors for impacts on constrained tank heads.

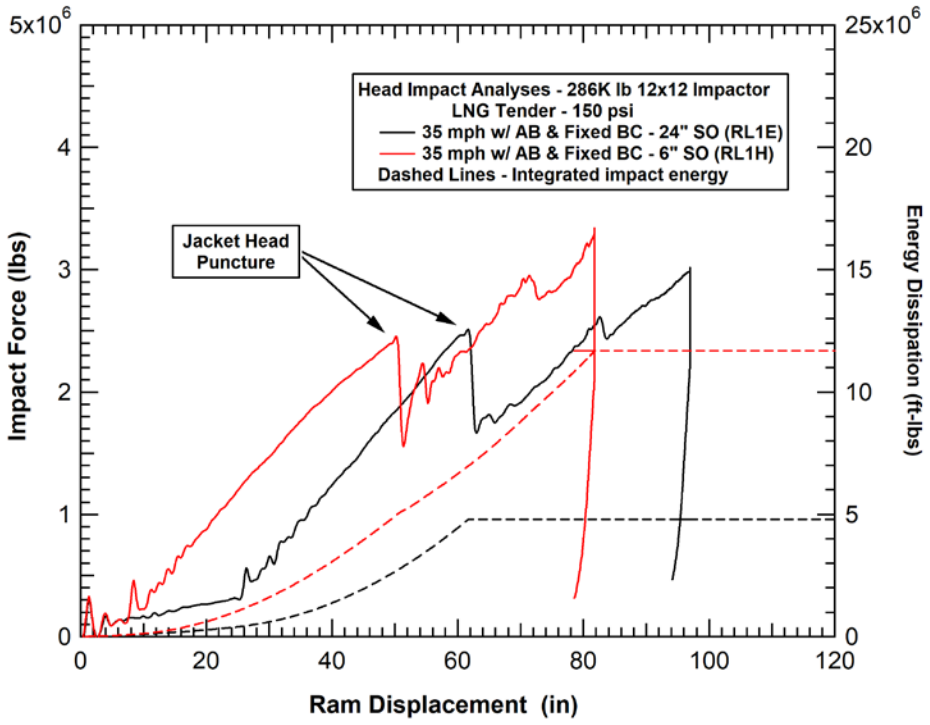

Figure 94. Calculated force-displacement behaviors for impacts on constrained tank heads.

4.5.2 Enhanced Head Impact Puncture Protection

The primary tank failure mode that was identified in the baseline head impact conditions was the puncture of the jacket head that would lead to a loss of vacuum and reduced insulation of the tender. The primary mechanism to provide enhanced protection for this failure mode is either increased thickness of the jacket head or switching to materials with a higher puncture resistance.

An analysis of the fixed head constraint impact configuration was performed with an increased jacket head thickness of 0.75-inch. The thicker jacket head was constructed from TC128B material used in the baseline analyses. The calculated force deflection for the enhanced design with the 0.75-inch-thick jacket head is compared to the performance of the baseline 0.50-inch-thick performance in Figure 95. The comparison shows an increased stiffness of the force deflection response up to the point of the jacket head rupture. The analyses show that the thicker jacket head increases the force required to puncture the jacket head by approximately 30%. The impact energy required to puncture the tank head also increased by a similar magnitude.

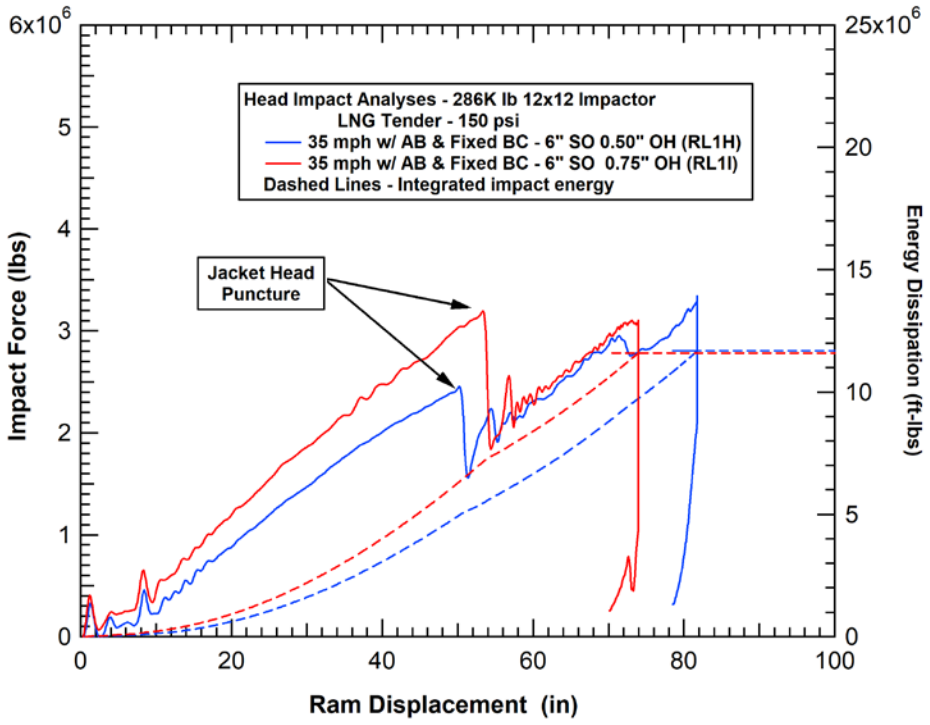

Figure 95. Effect of head thickness on the calculated impact force-displacement behaviors.

The remaining task was to determine if this increase in puncture force and energy is sufficient to withstand the impact conditions established for the tender specification. The primary requirements to assess this are to use a full tank and release the longitudinal constraints on the tank head to allow the impacted tank to move away from the impactor and to consider the offset impact conditions.

The calculated behavior for the constrained and unconstrained tender impact responses are compared in Figure 96. Also shown in the figure is the predicted response using a simple 1-D kinematics model [4] to predict the effects of releasing the constraints (dashed blue line). The comparison shows that releasing the constraint allows the impacted tender to move away from the impactor during impact. In these analyses, the unconstrained tender has moved between 1-2 feet at the time the peak load is achieved. As a result, the equilibrium velocity and rebound unloading between the impactor and tender occurs before the jacket head is punctured in the 35 mph impact.

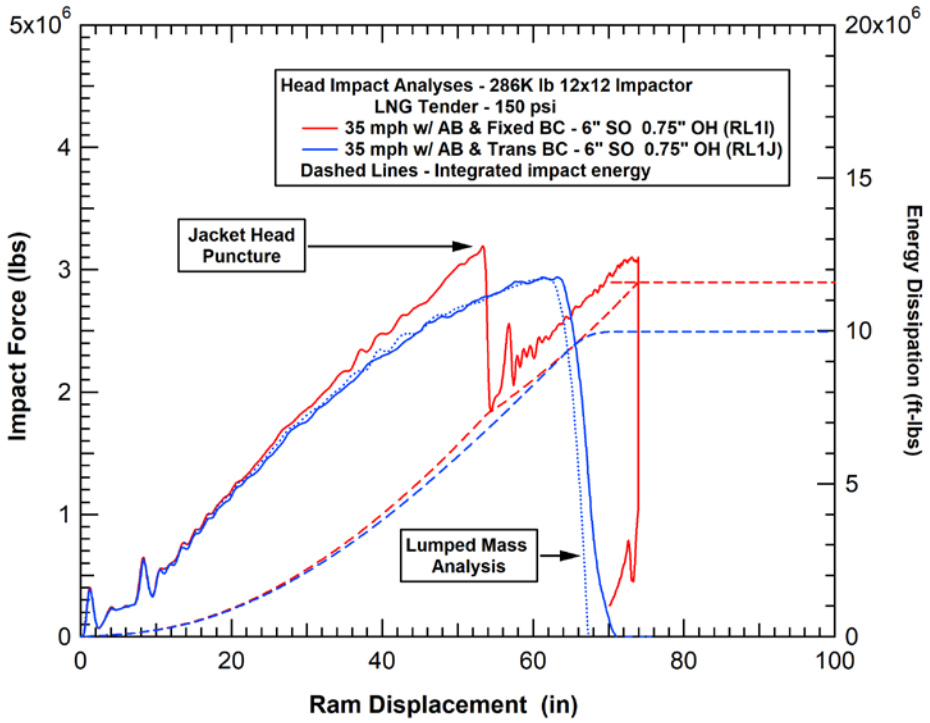

Figure 96. Effects of tank boundary constraints on the calculated head impact force-displacement behaviors.

The final analyses were performed to assess the 25 mph offset head impact condition as required by the tender specification. In this case, a constrained head impact analysis was performed and the 1-D lumped mass analysis was applied to assess the unconstrained response. This was demonstrated previously to accurately reproduce the unconstrained behavior. With the release of the longitudinal constraint, the tender is able to reach the equilibrium velocity and unload during the rebound between the impactor and tender before the jacket head is punctured. Thus, the analyses indicate protection levels can be met or exceeded using 0.50-in-thick 304L SS inner tank head and a 0.750-in-thick TC128B jacket head.

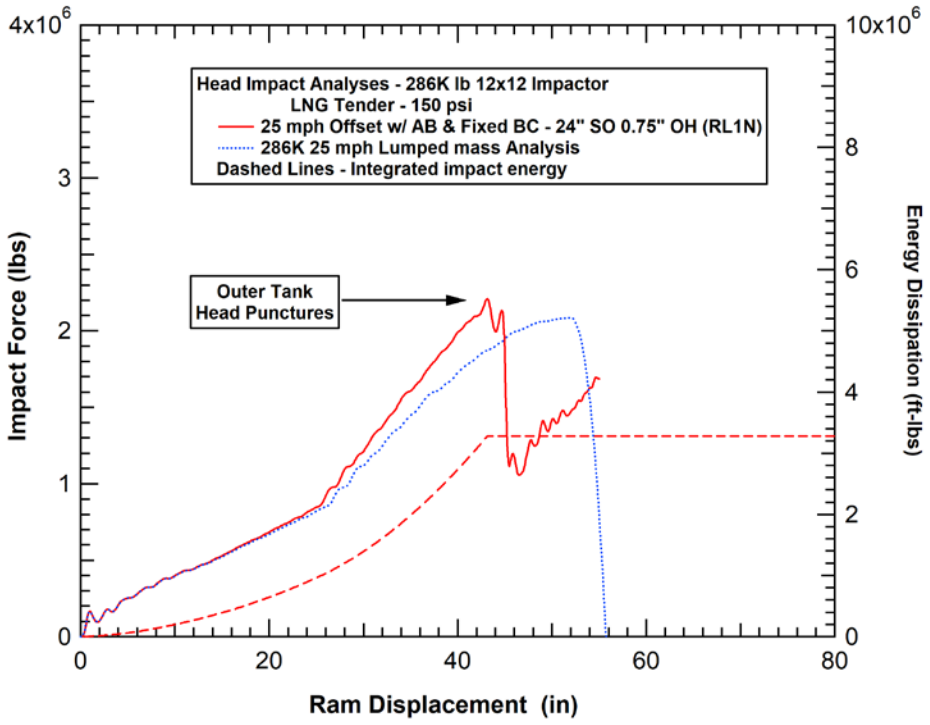

Figure 97. Calculated force-displacement behaviors for the offset 25 mph impact.

5 Summary and conclusions

Detailed finite element (FE) crash and impact analyses were performed for tender designs for a range of collision scenarios. The results of these analyses supported the efforts of the AAR and FRA to develop a safety specification for natural gas tenders. The analyses had an additional purpose to demonstrate that any requirement incorporated in the specification is realistic and can be addressed with available protection technologies. It was important to determine that it is possible to design a functional tender that meets the crash safety requirements in the specification.

The primary collision scenarios investigated for the tenders included:

- Head-on train-to-train collisions
- Grade crossing collisions
- Tender rollover conditions
- Tender tank side impact and head impact conditions

The tender tank side and head impact conditions were included to assess a variety of potential scenarios where the tank could be impacted in either a derailment or a collision.

The analyses improved our understanding of the collision behaviors and associated safety concerns for NGFTs. The results of the simulations were used by the NGFT TAG to understand the potential consequences of the proposed collision load cases and inform the development of performance criteria for tenders.

Analyses were performed for both legacy tender designs and a enhanced tender design. In general, the legacy LNG tender designs perform reasonably well and provides good protection for the cryogenic LNG tank. Thus, the legacy tenders provided a good baseline design on which various features of the design could be investigated and potentially improved.

During the performance of this project, in coordination with the tender specification development efforts, many structural enhancements were incorporated into the enhanced tender design. The design enhancements further improved the crashworthiness of the tender. Many of the enhancements originated with either the development or evaluation of alternative prescriptive design requirements. Thus, these prescriptive requirements are shown to be achievable but also require a significant level of structural integrity to meet the requirements.

6 References

1. Smith, K., “LNG: fuel of the future?” International Railway Journal, December 9, 2013.
2. Vantuono, W.C., “A closer look at LNG” Railway Age, November 8, 2013.
3. Kirkpatrick, S.W., “Detailed Puncture Analyses of Various Tank Car Designs,” ARA Final Technical Report, Prepared for the Next Generation Railroad Tank Car (NGRTC) Project, January, 2009.
4. S.W. Kirkpatrick, “Detailed Puncture Analyses of Various Tank Car Designs - Analysis of Different Impactor Threats and Impact Conditions,” ARA Draft Final Report, Prepared for the Federal Railroad Administration (FRA), July 31, 2012.
5. “LS-DYNA Keyword User’s Manual,” Volumes I through III, Livermore Software Technology Corporation, Version 971, March 2015.
6. "TrueGrid Manual, Version 3.0.0," Volumes 1 and 2, XYZ Scientific Applications, Inc., September 2014.
7. Florence, A.L., Gefken, P.R., and Kirkpatrick, S.W., "Dynamic Plastic Buckling of Copper Cylindrical Shells," Int. J. Solids and Structures, Vol. 27, No. 1, pp.89-103, 1991.
8. Holmes, B.S., Kirkpatrick, S.W., and LeMonds, J., "Ductile Failure of Shells Following Multiaxial Dynamic Strain Histories," ASME Publications, ASME Winter Annual Meeting, 1990.
9. Schwer, L.E., Holmes, B.S., and Kirkpatrick, S.W., "Response and Failure of Metal Tanks to Impulsive Spot Loading: Experiments and Calculations," Int. J. Solids and Structures, Vol. 24, No. 8, pp. 817-833, 1988.
10. Holmes, B.S., Kirkpatrick, S.W., and Schwer, L.E., "Response of Metal Tanks to Impulsive Spot Loading: Experiments and Calculations," Impact: Effects of Fast Transient Loadings, pp. 317-332, Ammann et al. (eds), A.A. Balkema Pubs., Rotterdam, 1988.
11. Kirkpatrick, S.W. and Holmes, B.S., "Structural Response of Thin Cylindrical Shells Subjected to Impulsive External Loads," AIAA J., Vol. 26, No. 1, pp. 96-103, January 1988.
12. Prantil, V.C., Kirkpatrick, S., Holmes, B.S., and Hallquist, J.O., "Response of a Very Thin Shell under an Impulsive Radial Load," Finite Element Methods for Plate and Shell Structures 2: Formulations and Algorithms, T.J.R. Hughes and E. Hinton (Eds), Pineridge Press LTD. Swansea, U.K., 1986.
13. Kirkpatrick, S.W. and Holmes, B.S., "The Effect of Initial Imperfections on Dynamic Buckling of Shells,” ASCE J. Engng. Mech., Vol. 115, No. 5, pp. 1075-1093, May 1989.
14. Kirkpatrick, S.W. and Holmes, B.S., "Static and Dynamic Buckling of Thin Cylindrical Shells," Computational Aspects of Impact and Penetration, R.F. Kulak and L.E. Schwer Eds., Elmepress International, Annandale VA, 1991.
15. Kirkpatrick, S.W. and Holmes, B.S., "Collapse of Thin Cylindrical Shells Under Combined Static Axial and Dynamic Radial Loads," Recent Advances in Impact Dynamics of Engineering Structures - 1989, ASME Pubs., AMD-Vol. 105, AD-Vol. 17, 1989.
16. Kirkpatrick, S.W. and Holmes, B.S., "Axial Buckling of a Thin Cylindrical Shell: Experiments and Calculations,” Computational Experiments, ASME Publications, PVP Vol. 176, pp. 67-74, 1989.
17. Kirkpatrick, S.W. and MacNeill, R.A., "Development of a Computer Model for Prediction of Collision Response of a Railroad Passenger Car,” Proceedings of: JRC2002, The 2002 ASME/IEEE Joint Rail Conference, April 23-25, 2002, Washington D.C.

18. Kirkpatrick, S.W., "Development and Validation of High Fidelity Vehicle Crash Simulation Models," Computer Applications for Crash, Optimization, and Simulation Research, SAE Publications SP-1496, Proceedings of the 2000 International Congress and Exposition, March 6-9, 2000, SAE Paper No. 2000-01-0627.

19. Kirkpatrick, S.W., Simons, J.W., and Antoun, T.H., "Development and Validation of High Fidelity Vehicle Crash Simulation Models," International Journal of Crashworthiness, IJCrash Vol. 4, No. 4, pp. 395-405, 1999.

20. Kirkpatrick, S.W., MacNeill, R.A., and Bocchieri, R.T., "Development of an LS-DYNA Occupant Model for use in Crash Analyses of Roadside Safety Features," Transportation Review Board, Paper No. TRB2003-0002450, Proc. of the 2003 TRB 82nd annual meeting, Washington D.C., Jan. 12-16, 2003.

21. Kirkpatrick, S.W. and MacNeill, R.A., "Development of a Computer Model for Prediction of Collision Response of a Railroad Passenger Car," Proceedings of: JRC2002, The 2002 ASME/IEEE Joint Rail Conference, April 23-25, 2002, Washington D.C.

22. Kirkpatrick, S.W. and Klopp, R.W., "Hazard Assessment for Pressure Tank Cars Involved in Accidents," ICrash 2000. Proceedings of the International Crashworthiness Conference, September 6-8, 2000, London, UK, E. C. Chirwa and D. Otte Eds., pp. 223-235.

23. Ray, M.H., Hiranmayee, K., and Kirkpatrick, S.W., "Performance Validation of Two Finite Element Models of a Side Impact Dummy," International Journal of Crashworthiness, IJCrash Vol. 4, No. 3, pp. 287-303, 1999.

24. Simons, J.W. and Kirkpatrick, S.W., "High-Speed Passenger Train Crashworthiness and Occupant Survivability," International Journal of Crashworthiness, IJCrash Vol. 4, No. 2, pp. 121-132, 1999.

25. Kirkpatrick, S.W., Holmes, B.S., Hollowell, T.C., Gabler, C., and Trella, T., "Finite Element Modeling of the Side Impact Dummy (SID)," Human Surrogates: Design, Development, & Side Impact Protection, SAE Publications, SP-945, pp. 75-86, Presented at the 1993 International Congress and Exposition, March, 1993, SAE Paper No. 930104.

26. Kirkpatrick, S.W., Giovanola, J.H., and Simons, J.W., "DYNA3D Analysis of Dynamic Fracture of Weldments," IA'96, Proceedings of International Seminar on Quasi-Impulsive Analysis, Nov. 20-22, 1996, Osaka, Japan, pp. A6.1-15, K. Wakiyama, E. Tachibana, K. Imai and T. Kitano Eds.

27. Giovanola, J. H., and Kirkpatrick, S. W., 1992, "Applying a Simple Ductile Fracture Model to Fracture of Welded T-Joints," in Advances in Local Fracture/Damage Models for the Analysis of Engineering Problems, AMD Vol. 137, J. H. Giovanola and A. J. Rosakis, Eds., American Society of Mechanical Engineers, New York, pp. 285-303.

28. Giovanola, J.H., and Kirkpatrick, S.W., 1993, "Methodology for Evaluating Strength and Fracture Resistance of Weldments Using a Local Approach to Fracture," in Pressure Vessel Integrity-1993, PVP-Vol. 250, W. E. Pennel, S. Bhandari, G. Yagawa, Editors, American Society of Mechanical Engineers, New York, pp.157-171

29. Giovanola, J.H., and Kirkpatrick, S.W., and Crocker, J.E., 1996, "Investigation of Scaling Effects in Elastic-Plastic Ductile Fracture Using the Local Approach," Proceedings of the First European Mechanics of Materials Conference on Local Approach to Fracture, Euromech-Mechamat '96, Fontainebleau-France, Sept. 9-11.

30. Simons, J.W., Kirkpatrick, S.W., Klopp, R.W., and Seaman, L., "Methods for Modeling Damage in Finite Element Calculations," IA'99, Proceedings of International Seminar on Quasi-Impulsive Analysis, Nov. 15-16, 1999, Osaka, Japan.

31. Giovanola, J.H., Kirkpatrick, S.W., and Crocker, J.E., "Fracture of Geometrically Scaled Notched Three-Point-Bend Bars of High Strength Steel," Journal of Engineering Fracture Mechanics, Vol 62, No. 2-3, pp. 291-310, March, 1999.

32. Giovanola, J.H. and Kirkpatrick, S.W., "Using the Local Approach to Investigate Scaling Effects in Ductile Fracture," International Journal of Fracture, Vol. 92, No. 2, pp. 101-117, 1998.

33. Giovanola, J.H., Klopp, R.W., and Kirkpatrick, S.W., "A Note on One-Point-Bend Impact Fracture Experiments with Curved Specimens," Technical Note, Journal of Testing and Evaluation, JTEVA, ASTM Publications, Jan. 1998, pp. 79-81.

34. Giovanola, J.H., Kirkpatrick, S.W., and Crocker, J.E., "Investigation of Scaling Effects in Elastic-Plastic Ductile Fracture Using the Local Approach," .JOURNAL DE PHYSIQUE IV, Colloque C6, supplement au Journal de Physique III, Volume 6, pp. C6-513-520, October 1996.

35. Giovanola, J.H., Kirkpatrick, S.W., and Crocker, J.E., "Experimental and Computational Investigation of Scaling Effects in Elastic-Plastic Ductile Fracture," Dynamic Plasticity and Structural Behaviors, Supplement Volume, Proc. of Plasticity '95: The Fifth International Symposium on Plasticity and its Current Applications, pp. 30-33, 1995.

36. Kirkpatrick, S.W., “Detailed Puncture Analyses of Various Tank Car Designs - Analysis of Different Impactor Threats and Impact Conditions,” Federal Railroad Administration (FRA) Final Report, Report No. DOT/FRA/ORD-13/17, March 2013.

37. S.W. Kirkpatrick, P. C. McKeighan, “Correlating Material Properties to Puncture Resistance to Enhance the Safety and Security of Tank Cars,” Advanced Tank Car Collaborative research Program (ATCRP) Final Report, January 2016.

38. S.W. Kirkpatrick and R.W. Klopp, "Risk Assessment for Damaged Pressure Tank Cars," 2003 COMPUTER TECHNOLOGY AND APPLICATIONS, ASME Publications, Proceedings of: PVP2003 - The 2003 ASME PVP Conference, July 20-24, 2003, Cleveland, Ohio, W. Reinhardt and D.J. Martin, Eds.

39. Kirkpatrick, S. W., “Analysis of the Tank Car Response in the Minot ND Derailment,” ARA Technical Report, June 17, 2005.

40. S.W. Kirkpatrick and R.W. Klopp, "Hazard Assessment for Pressure Tank Cars Involved in Accidents," ICrash 2000. Proceedings of the International Crashworthiness Conference, September 6-8, 2000, London, UK, E. C. Chirwa and D. Otte Eds., pp. 223-235.

41. R.W. Klopp, S.W. Kirkpatrick, and D.A. Shockey, “Damage Assessment of Tank Cars Involved in Accidents: Phase II - Modeling and Validation,” Final Technical Report to the Federal Railroad Administration, FRA Report, June, 1999.

42. Matthew Witte and Satima Anankitpaiboon, “Fully Instrumented Side Impact Test of Tank Car 3069,” Transportation Technology Center, Inc. Report No. P-07-033, October 8, 2007.

43. Matthew Witte and Satima Anankitpaiboon, “Second Fully Instrumented Tank Car Baseline Side Impact Test of Tank Car 3074,” Transportation Technology Center, Inc. Report No. P-07-034, October 8, 2007.

44. S.W. Kirkpatrick and R.W. Klopp, "Risk Assessment for Damaged Pressure Tank Cars," 2003 COMPUTER TECHNOLOGY AND APPLICATIONS, ASME Publications, Proceedings of: PVP2003 - The 2003 ASME PVP Conference, July 20-24, 2003, Cleveland, Ohio, W. Reinhardt and D.J. Martin, Eds.

45. S.W. Kirkpatrick and R.W. Klopp, "Hazard Assessment for Pressure Tank Cars Involved in Accidents," ICrash 2000. Proceedings of the International Crashworthiness Conference, September 6-8, 2000, London, UK, E. C. Chirwa and D. Otte Eds., pp. 223-235.

46. R.W. Klopp, S.W. Kirkpatrick, and D.A. Shockey, "Damage Assessment of Tank Cars Involved in Accidents: Phase II - Modeling and Validation," Final Technical Report to the Federal Railroad Administration, FRA Report, June, 1999.

47. National Transportation Safety Board, "Collision of Two Canadian National Railway Freight Trains near Two Harbors, Minnesota on September 30, 2010," Accident Summary Report, NTSB/RAR-13/01/SUM, Feb. 12, 2013.

48. Kirkpatrick, S.W., B.D. Peterson, and R.A. MacNeill, "Finite Element Analysis of Train Derailments," ICrash2006. Proc. of the Int'l Crashworthiness Conf., July 4-7, 2006, Athens, Greece.

49. Kirkpatrick, S. W., "Analysis of the Tank Car Response in the Minot ND Derailment," ARA Technical Report, June 17, 2005.

50. Pete McKeighan, "Tensile Properties and Stress-Strain Behavior of Various Steel Products Used in Fabricating Test Specimen for the NGRTC Program," NGRTC Project Memorandum, Southwest Research Institute, 21 November 2007.

51. Association of American Railroads, Technical Services Division, Mechanical Section—Manual of Standards and Recommended Practices.

52. "Draft of NTSB Material Laboratory Factual Report [In reference to Canadian Pacific Railway Derailment and Anhydrous Ammonia Release, Minot, ND, January 18, 2002, DCA-02-MP-002]," Frank Zakar, Metallurgy Group Chairman, Feb. 14, 2003.

53. J-H, Kim, K-Y Kang, M-H Kim, and J-M Lee, "Elasto-Visco-Plastic-Damage Model for Pre-Strained 304L Stainless Steel subjected to Low Temperature," World Academy of Science, Engineering and Technology, Vol:61 2012-01-26, pp. 195-200.

54. R. K. Blandford, D. K. Morton, S. D. Snow, and T. E. Rahl, "Tensile Stress-Strain Results for 304L and 316L Stainless Steel Plate at Temperature," Paper No. PVP2007-26096, Proceedings of the PVP2007, ASME Pressure Vessel and Piping Division Conference, July 20-27, 2007, San Antonio, TX.

55. L.E. Malvern, Introduction to the Mechanics of a Continuous Medium, Prentice-Hall, 1969.

56. Pete McKeighan, "Notched Tensile Properties of Tank Car Material from Full Scale Test No. 1 (Car No. 3069) and Test No. 2 (3074) Oriented in the Transverse Direction," NGRTC Project Memorandum, Southwest Research Institute, 20 November 2007.

57. Pete McKeighan, "Notched Tensile Properties of Thickest TC128B Tank Car Material from Material Inventory for Fabricating Test Specimens," NGRTC Project Memorandum, Southwest Research Institute, 6 December 2007.

58. Pete McKeighan, "Shear Tests on TC128B Normalized Material of Two Different Thicknesses," NGRTC Project Memorandum, Southwest Research Institute, December 2007.

59. Pete McKeighan, "Puncture Tests on Jacket Material (A1011, 90X) and Normalized TC128B Shell Material (two thicknesses)- Revised," NGRTC Project Memorandum, Southwest Research Institute, 17 December 2007.

60. Pete McKeighan, "Puncture Behavior of 0.48-inch Thick A516 Material," NGRTC Project Memorandum, Southwest Research Institute, 12 April 2008.

61. Pete McKeighan, “Puncture Properties of Different 90x Stacked Layers and a Composite Structure,” NGRTC Project Memorandum, Southwest Research Institute, 23 March 2008.

62. Bao, Y., and Wierzbicki, T., “On Fracture Locus in the Equivalent Strain and Stress Triaxiality Space,” International Journal of Mechanical Sciences 46, 81-98.

63. Bao, Y., and Wierzbicki, T., “A Comparative Study on Various Ductile Crack Formation Criteria,” Journal of Engineering Materials and Technology 126, 314-324.

64. Beremin, F. M., 1981, "Study of Fracture Criteria for Ductile Rupture of A508 Steel," in Advances in Fracture Research (ICF5), D. François, Ed., Pergamon Press , pp. 809-816.

65. Chaboche, J. L. et al., Editors, 1986, "Séminaire International sur l'Approche Locale de la Rupture," Conference Proceedings, Centre de Recherches EDF, "Les Renardières," Moret-sur-Loing, France.

66. Curran, D. R., Seaman, L. and Shockey, D. A, 1987, "Dynamic Failure of Solids," Physics Reports, Vol. 147, pp. 253-388.

67. Lemaitre, J., 1986, "Local Approach of Fracture," Engineering Fracture Mechanics, Vol. 25, pp. 523-537.

68. Mudry, F., 1985, "Methodology and Applications of Local Criteria for Prediction of Ductile Tearing," Elastic-Plastic Fracture Mechanics, L. H. Larson, ed., ECSC, EEC, EAEC, Brussels and Luxembourg, Belgium, pp. 263-283.

69. Hancock, J. W. and Mackenzie, A. C., 1976, "On the Mechanisms of Ductile Failure in High-Strength Steels Subjected to Multiaxial Stress States," Journal of the Mechanics and Physics of Solids, 24, pp. 147-169.

70. Rice, J. R., and Tracey, D. M., 1969, "On the Ductile Enlargement of Voids in Triaxial Stress Fields," J. Mech. Phys. Solids, 17, 201-217.

71. Giovanola, J. H., and Rosakis, A. J., Editors, 1992, Advances in Local Fracture/Damage Models for the Analysis of Engineering Problems, AMD-vol. 137, American Society of Mechanical Engineers, New York.

72. Giovanola, J. H., and Kirkpatrick, S. W., 1992, "Applying a Simple Ductile Fracture Model to Fracture of Welded T-Joints," in Advances in Local Fracture/Damage Models for the Analysis of Engineering Problems, AMD Vol. 137, J. H. Giovanola and A. J. Rosakis, Eds., American Society of Mechanical Engineers, New York, pp. 285-303.

73. Giovanola, J.H., and Kirkpatrick, S.W., 1993, "Methodology for Evaluating Strength and Fracture Resistance of Weldments Using a Local Approach to Fracture," in Pressure Vessel Integrity-1993, PVP-Vol. 250, W. E. Pennel, S. Bhandari, G. Yagawa, Editors, American Society of Mechanical Engineers, New York, pp.157-171.

74. Giovanola, J.H., and Kirkpatrick, S.W., and Crocker, J.E., 1996, "Investigation of Scaling Effects in Elastic-Plastic Ductile Fracture Using the Local Approach," Proceedings of the First European Mechanics of Materials Conference on Local Approach to Fracture, Euromech-Mechamat '96, Fontainebleau-France, Sept. 9-11.

75. Gurson, A.L., “Continuum Theory of Ductile Rupture by Void Nucleation and Growth: Part 1—Yield Criteria and Flow Rules for Porous Ductile Media.” Journal of Engineering Materials and Technology, Vol. 99, 1977, pp. 2-15.

76. Tvergaard, V., “On Localization in Ductile Materials Containing Spherical Voids.” International Journal of Fracture, Vol. 18, 1982, pp. 237-252.

77. Tvergaard, V., “Material Failure by Void Growth to Coalescence.” Advances in Applied Mechanics, Vol. 27, 1990, pp. 83-151.

78. T.L. Anderson and S.W. Kirkpatrick, “Quantifying and Enhancing Puncture Resistance in Railroad Tank Cars Carrying Hazardous Materials,” Technical Report, Prepared for The Chlorine Institute, August 7, 2006.

79. Mackenzie, A. C., Hancock, J. W., and Brown, D. K., 1977, "On the Influence of State of Stress on Ductile Failure Initiation in High-Strength Steels," Eng. Fracture Mechanics, 9, 167-188.

80. S.W. Kirkpatrick and R.A. MacNeill, "Development of a Computer Model for Prediction of Collision Response of a Railroad Passenger Car,” Proceedings of: JRC2002, The 2002 ASME/IEEE Joint Rail Conference, April 23-25, 2002, Washington D.C.

81. Russell Walker, Greg Garcia, Satima Anankitpaiboon, and Kari Gonzales, “Tank Car Head Baseline Component Test,” Transportation Technology Center, Inc. Report No. P-08-009, April 2008.

82. S.W. Kirkpatrick, “Analyses of Top Fittings Protection on a Sulfuric Acid Tank Car,” ARA Final Technical Report, Prepared for the Union Tank Car Company, December 17, 2009.

83. S.W. Kirkpatrick, "Top Fittings Analyses for a Flued Nozzle on a UTLX BD 10-110-30 Tank Car using 286K GRL," ARA Technical Report, Prepared for UTLX Manufacturing Inc., July 25, 2013.

84. S.W. Kirkpatrick, “Analyses of Top Fittings Protection on Non-Pressure Tank Cars,” ARA Final Technical Report – Revision 1, Prepared for the Union Tank Car Company, December 10, 2009.

85. S.W. Kirkpatrick, “Analyses of Top Fittings Protection on Non-Pressure Tank Cars,” ARA Final Technical Report, Prepared for the Union Tank Car Company, October, 2009.

86. S.W. Kirkpatrick, “Detailed Analyses of the UTLX DOT-111A100W Tank Car Design,” ARA Final Technical Report, Prepared for the Union Tank Car Company, October 15, 2010.

87. S.W. Kirkpatrick, “Analyses of Top Fittings Protection on a 105J500I Tank Car,” ARA Final Technical Report - Revision 1, Prepared for the Union Tank Car Company, August 15, 2011.

88. S.W. Kirkpatrick, “Analyses of Top Fittings Protection on a 29,000 Gallon 111A100W Tank Car,” ARA Final Technical Report, Prepared for the Union Tank Car Company, December 10, 2010.

89. S.W. Kirkpatrick, “Detailed Analyses of the Advanced UTLX Chlorine Tank Car Design,” ARA Final Technical Report, Prepared for the Union Tank Car Company, May, 2010.

90. Pete McKeighan, “Tensile Properties and Stress-Strain Behavior of Various Steel Products Used in Fabricating Test Specimen for the NGRTC Program,” NGRTC Project Memorandum, Southwest Research Institute, 21 November 2007.

91. P. Wakulchik, Touchstone Testing Labs Test Report No. AR20472, September 29, 2017.

Appendix A – Characterization of 304L Stainless Steel at LNG Cryogenic Temperature

Introduction

During the performance of the NGFT project, described in the main body of this report, the steel characteristics for the cryogenic inner tank used data from 304L stainless steel at LNG Cryogenic temperatures (-260F, 110K) were obtained from an open literature source that reported test data [53]. The inner tank is required to be manufactured of ATSM A240, Type 304 or 304L by the specification. A240 304 Stainless Steel has a well-established performance history in several hundred DOT-113 tank cars as well as in many thousands of other cryogenic tanks and trailers and is the likely material for use in NGFTs. The behavior was expected to be very similar to that of the 304L data used in the study.

Since there is not a large amount of information readily available on the behavior of A240 304 Stainless Steel at low temperature and the response of the inner tank to impact damage is a critical safety issue for NGFTs, the TAG thought it was important to perform a supplemental characterization test program. The testing performed included tensile, notched tensile, and high-rate tensile test series. A summary of that data is provided here.

Characterization Testing

The material characterization test program included longitudinal and transverse tensile tests, notched round bar tensile tests, and longitudinal tensile tests at elevated strain rates. The objective was to perform three repeat tests at each condition to assess repeatability of results. The tensile data for the A240 304 at -260F is compared to the previous cryogenic data for the 304L stainless material in Figure B1. The testing was performed to E8/E8M − 16a standard test methods for tension testing of metallic materials using the specimen geometry shown in Figure A2 [91]. As expected, the stress-strain behaviors for the two materials is similar. Both materials have similar yield strengths and elongations. The largest difference is the ultimate strength, which is approximately 195 ksi for the A240 304 material compared to 205 ksi for the 304L stainless.

The comparison of the smooth tensile and notched tensile data for the 304 stainless material at LNG cryogenic temperature is shown in Figure A3. The drawings of the specimen geometries used in the Notched tensile testing are shown in Figure A4. Since the notch increases the stress triaxiality in the gauge section it results in an increase in the yield and ultimate strength, as expected. The testing used a 1.0-inch gauge length extensometer bridging the notch but the deformation will not be uniform within this gauge section due to the presence of the notch. As a result, the overall engineering elongation for these tests are reduced compared to the smooth

round bar tension tests. However, the measured elongations of approximately 25% are quite large for this type of testing on metals.

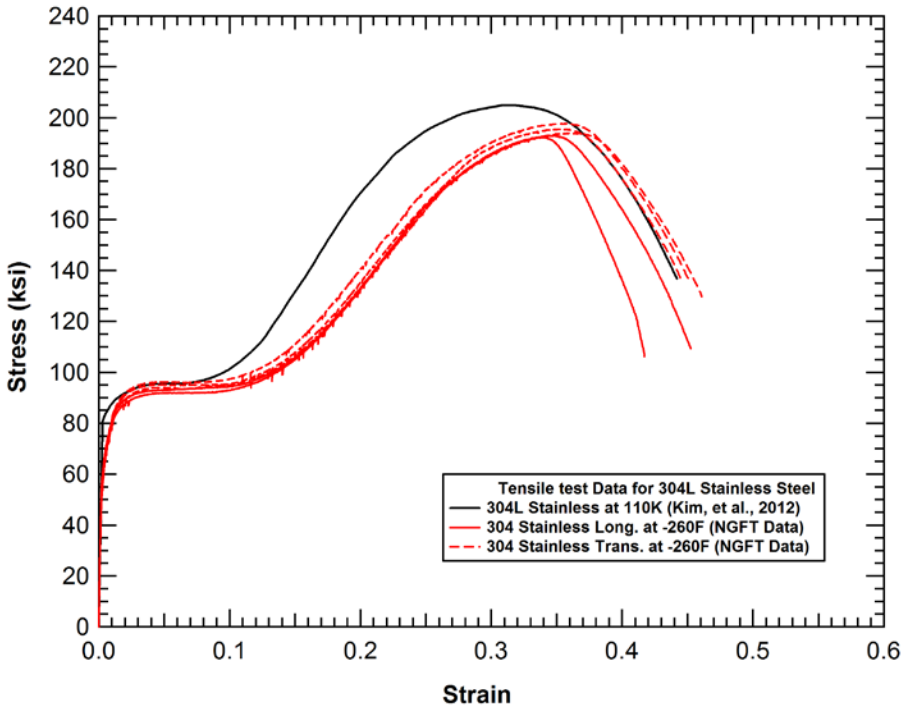

Figure A1. Comparison of the quasi-static tensile data to previously reported data.

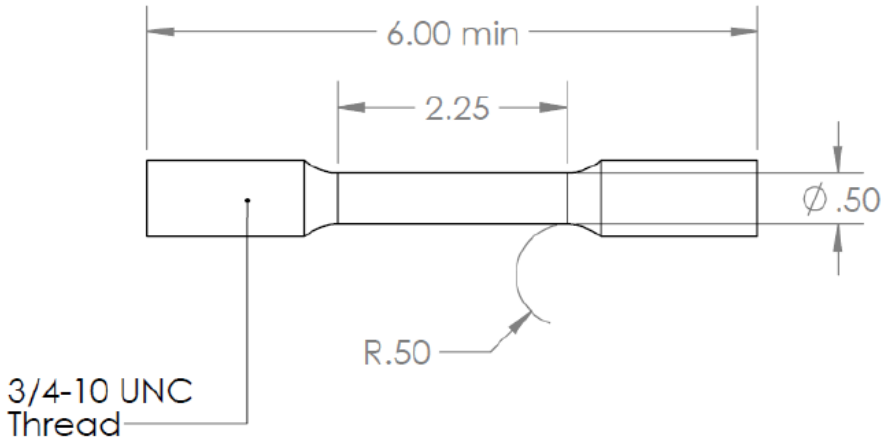

Figure A2. ASTM E8 specimen geometry used for the quasi-static tensile tests.

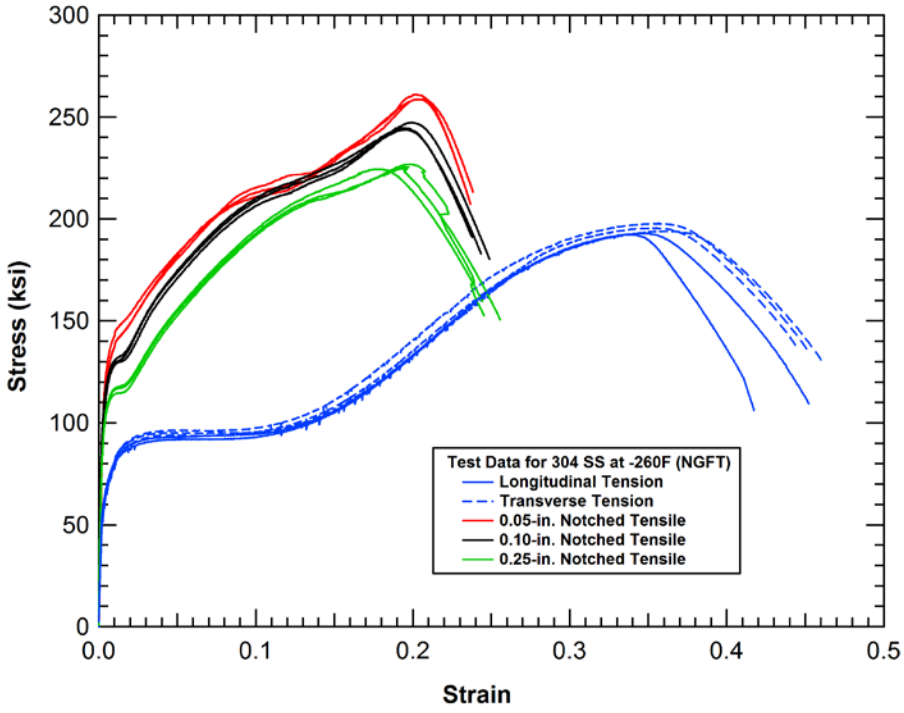

Figure A3. Summary of the 304 stainless quasistatic tensile test data.

The quasistatic tensile testing is compared to the elevated rate tensile testing in Figure A5. The quasistatic testing has a strain rate of approximately 0.0005 (in/in)/s. The elevated rate testing was performed using strain rates of 0.01, 0.1, 1.0, and 10.0 (in/in)/s. These high rate tests use a round bar specimen geometry with a shortened specimen gauge length, shown in Figure A6. For comparison, the quasistatic longitudinal tensile behavior measured with the standard round bar tensile test with the 2-inch gauge section length, shown previously in Figure A2.

A summary of the measured yield strengths and ultimate strengths for the specimens at the various strain rates is provided in Table 1. The comparison of the data shows that thin increasing strain rate elevates the yield stress from approximately 89 ksi at quasistatic rates to 105 ksi at 10.0 (in/in)/s. Alternatively, the ultimate stress is reduced by the elevated strain rates from approximately 195 ksi at quasistatic rates to 166 ksi at 1.0 (in/in)/s. Note that at the highest strain rate of 10.0 (in/in)/s the ultimate stress begins to increase. The source of this effect (inertial effects, specimen variability, etc.) is not known.

The elongation at the ultimate strength is similar for all of the strain rates. The additional elongation after the ultimate stress for the high rate tests is most likely a result of the smaller 0.5-inch gauge length in the high rate tests compared to the 2.0-inch gauge length in the quasistatic tests. As a result, the necking behavior would produce a greater engineering elongation for the shorter gauge length measurements.

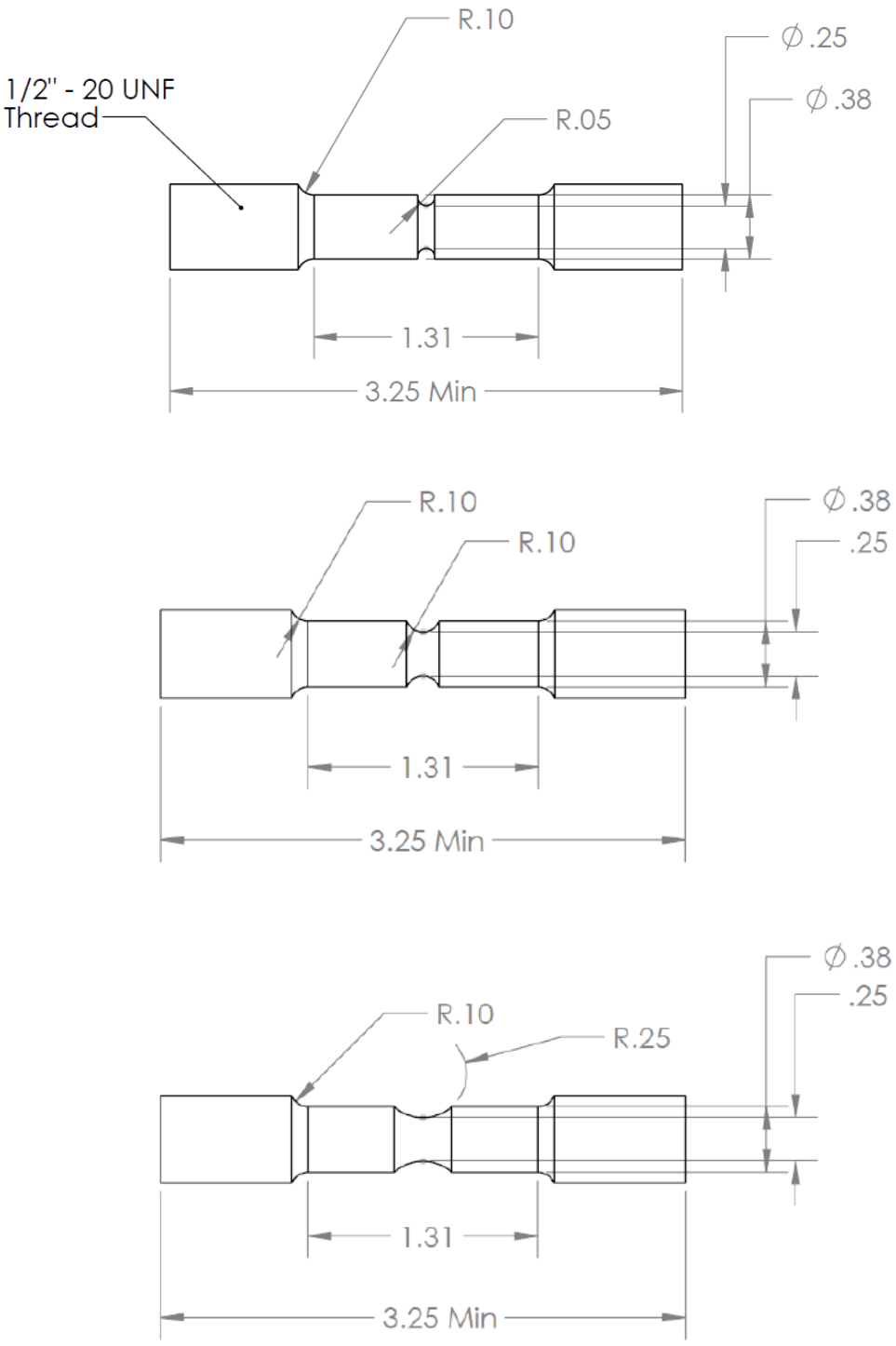

Figure A4. Notched specimen geometries used in stainless steel testing detailed in this Appendix.

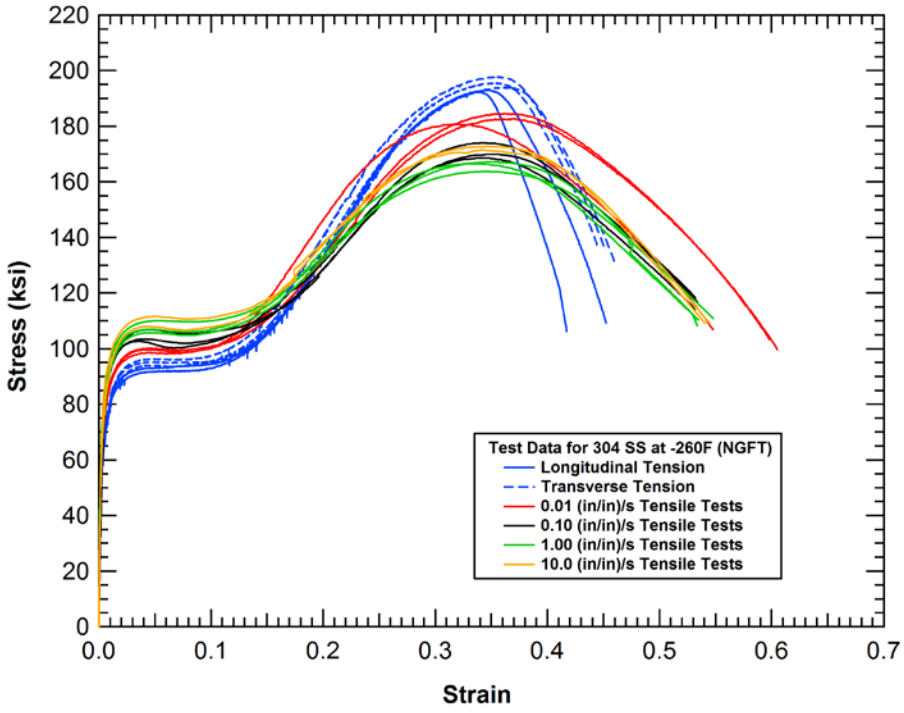

Figure A5. Summary of the 304 stainless tensile test data at elevated strain rates.

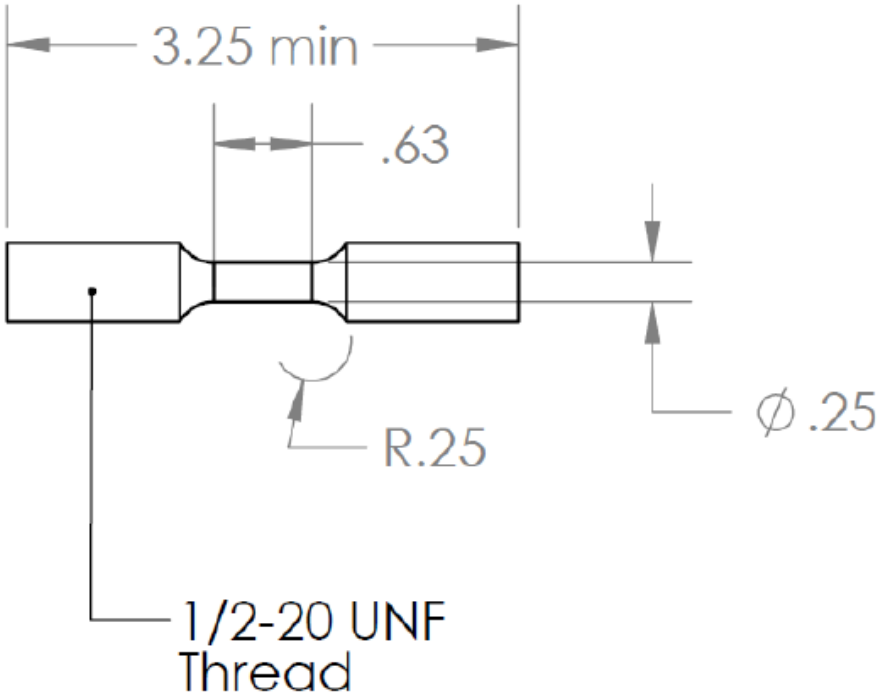

Figure A6. Specimen geometry used in the elevated strain-rate testing detailed in this Appendix.

Table A1. Summary of rate effects on strength of the A240 304 at cryogenic temperature.

Strain Rate (in/in)/s	Yield Stress (ksi)	Ultimate Stress (ksi)
0.0005	89	195
0.01	96	183
0.10	100	170
1.00	103	166
10.0	105	171

Summary and Conclusions

A characterization test program was performed on A240 304 stainless steel at LNG cryogenic temperature. The testing found that the behavior was similar to those used from literature sources for cryogenic 304L stainless steel that was used in the analyses in this report. The largest difference was an approximately 10 ksi reduction in ultimate strength for the A240 304 material from 205 ksi to 195 ksi. In addition, testing at elevated rates found an increase in yield strength and reduction in the ultimate strength.

Overall, the testing of the material confirm properties that would result in a puncture resistance for this material at cryogenic temperatures that is quite high. However, the material property differences would be expected to result in a moderate reduction in the puncture resistance compared to the cryogenic 304L stainless steel data used in the modeling in the main body of the report. However, as the impact requirements were being developed, the emphasis shifted to preventing punctures to the jacket (or jacket head). Under these conditions, there would be little risk of a puncture to the inner cryogenic tank. The damage to the inner tank would not reach the level where the material property differences would become significant. As a result, the new mechanical test data was never used to perform revised analyses.